UAV Detection Based on Adaptive Radar Signal Processing

by

Ahmed Nasser Abdelmohsen Sayed

A thesis
presented to the University of Waterloo
in fulfillment of the
thesis requirement for the degree of
Doctor of Philosophy
in
Electrical and Computer Engineering

Waterloo, Ontario, Canada, 2024

© Ahmed Nasser Abdelmohsen Sayed 2024

Examining Committee Membership

The following served on the Examining Committee for this thesis. The decision of the Examining Committee is by majority vote.

External Examiner:	Christos Christodoulou Professor Department of Electrical and Computer Engineering University of New Mexico
Supervisors:	Omar Ramahi Professor Department of Electrical and Computer Engineering University of Waterloo
	George Shaker Adjunct Associate Professor Department of Electrical and Computer Engineering University of Waterloo
Internal Members:	Patrick Mitran Professor Department of Electrical and Computer Engineering University of Waterloo
	Mark Crowley Associate Professor Department of Electrical and Computer Engineering University of Waterloo
Internal-External Member:	Amir Khajepour Professor Department of Mechanical and Mechatronics Engineering University of Waterloo

Author's Declaration

I hereby declare that I am the sole author of this thesis. This is a true copy of the thesis, including any required final revisions, as accepted by my examiners.

I understand that my thesis may be made electronically available to the public.

Abstract

Unmanned Air Vehicles (UAVs), commonly known as drones, have become widely available across the globe; they can be used for many useful applications, but they can also be used for illegal activities and terrorist attacks. Therefore, it is crucial to identify and classify UAVs for safety and security purposes. For this objective, the detection and classification of UAVs is important. Radar systems are considered a promising solution for the detection and classification of UAVs compared to the other UAV detection systems. Generating radar datasets that contain UAV information to train Machine Learning (ML) algorithms through real measurements is costly and time-consuming. In addition, these datasets are limited to the radar parameters, the types and number of UAVs, and the background environment where these measurements are taken. By simulating all these parameters, synthetic radar datasets that contain UAV information can be generated without many constraints. Furthermore, in the state-of-the-art literature, ML algorithms were trained and tested on radar UAV datasets that were generated by taking radar measurements of hovering and/or pitching UAVs only. Training ML algorithms on datasets containing hovering and/or pitching motions only leads to a degradation in ML accuracy to classify these UAVs when the trained ML algorithms are tested on different datasets that contain different motions of the UAVs.

In this thesis, a new method to generate synthetic radar datasets that contain UAV information is introduced. This method is based on using 3D full-wave Electromagnetic (EM) Computer-Aided Design (CAD) tools to model the UAVs, the radars, and the background environments. The novelty of this method is that full-wave EM CAD tools are used to simulate the motion of UAVs and perform time-based full-wave analysis. Using this new method, a large number of complex scenarios can be modeled and investigated within a short time, and at a low cost. The proposed method is validated, and a ML algorithm is applied to it, yielding an accuracy exceeding 97%. Additionally, the proposed methodology makes it easier to analyze attempts to deceive radar systems, which has the potential to improve the accuracy and effectiveness of UAV detection and classification using radar systems. Furthermore, an investigation on the effect of the control systems of four different UAVs on their range-Doppler signatures is conducted. Different UAVs datasets containing range-Doppler information of different motions of these UAVs are generated using a full-wave EM CAD tool. The range-Doppler signatures are demonstrated to be highly dependent on the mechanical control information of these UAVs. The mechanical control information for the four UAVs is employed using eight different ML algorithms to investigate their impact on classifying the four UAVs. A Mechanical Control-Based Machine Learning (MCML) algorithm is introduced to classify these UAVs. The proposed MCML

method overcomes the degraded classification accuracy when the mechanical control information of UAVs is not taken into consideration, yielding an accuracy exceeding 90%. Overall, the proposed MCML method demonstrated superior accuracy when compared to state-of-the-art works employing radars for UAV classification.

In addition, the importance of using Multiple-Input Multiple-Output (MIMO) radars in the field of detection and classification of UAVs is explored. A Single-Input Single-Output (SISO) radar system is used to investigate the impact of its antenna's Field of View (FOV) on the classification of UAVs. It is shown that the classification accuracy decreases with the increase of the relative angle between the UAVs and the radar's antenna. However, it is shown that MIMO radars increase the classification accuracy significantly. For example, it is demonstrated that with an antenna beamwidth of 30°, the classification accuracy of a Convolutional Neural Network (CNN) algorithm increases from 13.4%, using the SISO radar system to 60.83% using the MIMO radar system, at a relative angle of 80° between the antennas and the UAVs. Also, MIMO radar systems provide a high level of accuracy in the area of multi-UAV classification. MIMO radars are used to count the number of UAVs in a scene and enable their simultaneous classification. Although using MIMO radar systems enhances the detection of UAVs, MIMO radars struggle to detect and classify multiple UAVs at wide relative angles. To address this issue, this thesis proposes a Range-Doppler Integration while Steering (RDIwS) beamforming-based method, which further enhances UAV detection and classification, particularly in scenarios involving multiple UAVs and wider relative angles. The method involves steering the antenna beam to various angles, thereby concentrating the radar's energy on targets within these angles. Subsequently, the range-Doppler maps obtained within each sector of steered angles are integrated to generate a range-Doppler map for the entire FOV. The RDIwS beamforming-based method improves the Signal to Noise Ratio (SNR) of radar targets, subsequently boosting the radar's detection probability for multiple targets at varying angles. For a scenario with four UAVs positioned at different angles and distances, with a SNR of $-30\ dB$ and a false alarm probability of 10^{-5}, the RDIwS method achieves a detection probability of 75%, as opposed to 5% for steering-only beamforming and no detection in the MIMO radar case.

This thesis addresses certain limitations in radar-based UAV detection and classification, which significantly enhances the detection and classification of UAVs using radar systems. However, key areas for future research include the expansion of real-measurements to include more UAVs and controlled experiments for birds, exploration of radars without distance limitations, implementation of real-time signal processing, incorporation of noise sources for more realistic simulations, consideration of tracking models to provide information of the behavior of UAVs, evaluation of ML methods beyond accuracy, and exploration of radar sensor fusion with cameras.

Acknowledgements

I express my profound gratitude to my esteemed supervisors, Professor Omar Ramahi and Professor George Shaker, for their invaluable guidance, unwavering support, and profound expertise throughout my doctoral studies. Their insightful feedback and encouragement played a pivotal role in shaping the trajectory of this comprehensive work.

I extend my gratitude to the members of my PhD committee, Professor Patrick Mitran, Professor Mark Crowley, Professor Amir Khajepour, and Professor Christos Christodoulou, for their invaluable comments and suggestions.

A special appreciation is extended to the Ministry of Defense of the Arab Republic of Egypt for their crucial funding and support, facilitating the execution of this extensive research. Sincere acknowledgments are also conveyed to the Natural Sciences and Engineering Research Council of Canada (NSERC), the Canadian Microelectronics Centre, the Ansys Electronics Desktop team, the Home of Robotics at Waterloo (RoboHub), and The Schlegel-UW Research Institute for Aging (RIA) for their invaluable support, significantly enriching the depth and breadth of this study.

Inexpressible gratitude is dedicated to my wife, Nehal, and my children, Ali and Nelly, whose unwavering love, encouragement, and steadfast belief in my abilities provided the solid foundation upon which I could passionately pursue this scholarly endeavor. Additionally, my deepest appreciation and love are extended to my family in Egypt for their unwavering support and unconditional love.

A collective acknowledgment is extended to all individuals who have contributed to my research, whether directly or indirectly. Special mention goes to my friends and colleagues at the Wireless Sensors and Devices Lab and the Advanced Concepts Research Laboratory. Dr. Hajar Abedi and Mr. Ahmad Ansariyan, your assistance, collaboration, and encouragement have been instrumental in the successful completion of this thesis. The collaborative spirit within this community has been a driving force behind the culmination of this significant academic pursuit.

Dedication

In heartfelt dedication, I offer this work to my cherished wife, children, parents, and sisters. Your steadfast support and unwavering belief in me have been the driving force behind my persistent pursuit of knowledge. Your guidance and encouragement have not only sustained me but also molded me into the person standing here today.

This accomplishment is a shared triumph, as much yours as it is mine. I am eternally grateful for the profound impact of your presence in my life, shaping the course of my academic journey and contributing immeasurably to the person I have become.

Table of Contents

Examining Committee ii

Author's Declaration iii

Abstract iv

Acknowledgements vi

Dedication vii

List of Figures xi

List of Tables xvi

List of Abbreviations xvii

List of Symbols xxi

1 Introduction 1

1.1 Motivation 1

1.2 Objective 2

1.3 Thesis Outline 3

2 Radar-Based UAV Detection: A Literature Review **5**
2.1 Introduction . . . 5
2.2 State-of-the-Art Literature . . . 6
2.3 Unaddressed Aspects in Literature Review . . . 13

3 UAV Classification using Machine Learning and Full-Wave EM CAD Tools **15**
3.1 Introduction . . . 15
3.2 Radar Datasets Generation . . . 18
3.2.1 Methodology Validation . . . 18
3.2.2 Datasets Generation . . . 23
3.3 Classification Results . . . 27
3.4 Countering Radar Deception . . . 32

4 Mechanical Control-Based Machine Learning for UAV Classification **41**
4.1 Introduction . . . 41
4.2 Mathematical Background . . . 42
4.2.1 Quadcopter Equations of Motions . . . 42
4.2.2 Hexacopter Equations of Motions . . . 45
4.3 Simulation Setups . . . 46
4.4 Classification Results . . . 52

5 Improvement of UAV Detection and Classification **59**
5.1 Introduction . . . 59
5.2 Mathematical Background . . . 60
5.3 MIMO and SISO Radars Classification Results . . . 64
5.3.1 Synthetic Datasets . . . 66
5.3.2 Real-Measurements Datasets . . . 68
5.4 RDIwS Beamforming-Based Method for UAV Detection and Classification 73
5.4.1 Performance Analysis of the RDIwS method . . . 74
5.4.2 Evaluation of the RDIwS Method . . . 80

6 Conclusions and Future Works **85**

6.1 Conclusions 85

6.1.1 Supplementary Resources 87

6.2 Limitations and Future Works 88

6.3 Publications 90

6.3.1 Book Chapters 90

6.3.2 Journal Articles 90

6.3.3 Conference Papers 91

References **93**

List of Figures

1.1 Flowchart of the thesis outline. 3

3.1 Range-Doppler maps generation for FMCW radars. 17

3.2 One rotating blade. 19

3.3 Range-Doppler images of the rotating blade with different radars. (a) L-Band. (b) X-Band. (c) W-Band. (d) Range-Doppler Accuracy Results. . . 20

3.4 (a) A "like" pendulum simulation setup. (b) Range values. (c) Doppler velocity values. 21

3.5 Spectrogram results for (a) One blade rotor. (b) Two blades rotor. (c) Three blades rotor. (d) Four blades rotor. 22

3.6 Simulated test setup for the six different types of UAVs using Ansys HFSS. 23

3.7 (a) The DJI S900 hexacopter UAV [1]. (b) HFSS model for the DJI S900 hexacopter UAV. (c) Three-time stamps for the modeled DJI S900 hexacopter UAV showing the rotation of its blades. 24

3.8 Range-Doppler images for the: (a) Fixed-wing UAV. (b) Helicopter UAV. (c) Hexacopter UAV. (d) DJI FPV quadcopter UAV. (e) MD4-1000 quadcopter UAV. (f) DJI Phantom 3 standard quadcopter UAV. 25

3.9 (a) A flowchart of the used CNN algorithm. (b) The confusion matrix result for the CNN algorithm. (c) The classification report for the used CNN algorithm. 28

3.10 (a) Simulated test setup for a new scenario. (b) Classification accuracy of applying the trained CNN algorithm to a new scenario for different UAV types. 29

3.11 A hexacopter and a quadcopter model A in the same scene. 30

3.12 The AWR1443BOOST TI radar (left in red) [2] and the DCA1000EVM board (right in green) [3]. 31
3.13 (a) Lab-measurements setup for the DJI Phantom 3 standard. (b) Range-Doppler image for the DJI Phantom 3 standard using the AWR1443BOOST TI radar. 32
3.14 The effect of changing a UAV's material/coating (a) PEC material. (b) Plastic material. 34
3.15 HFSS models depicting the DJI Phantom 3 standard UAV with explosives attached. (a) Rocket. (b) Dynamite. 35
3.16 Accuracy of the CNN algorithm to detect if a standard UAV is carrying explosives using range-Doppler information. 35
3.17 Range-Doppler maps for the DJI Phantom 3 standard UAV when: (a) Nothing attached. (b) Rocket attached. (c) Dynamite attached. 36
3.18 ISAR images for the DJI Phantom 3 standard UAV when: (a) Nothing attached. (b) Rocket attached. (c) Dynamite attached. 36
3.19 Accuracy of the CNN algorithm to detect if a standard UAV is carrying explosives using ISAR images. 37
3.20 Range-Doppler maps for: (a) The quadcopter UAV. (b) The bird. 37
3.21 Confusion matrices of the trained ML models. (a) CNN. (b) SVM. 38
3.22 Simulation setup for the quadcopter with: (a) One/two birds. (b) Swarm of 10 birds. 39

4.1 (a) Traditional Method. (b) Proposed MCML Method. 42
4.2 The quadcopter frame body [4]. 43
4.3 The hexacopter frame body [5]. 45
4.4 Simulation setups for the UAVs' different movements. (a) Throttle. (b) Pitch. (c) Roll. (d) Yaw. 47
4.5 Quadcopter control [6]. 48
4.6 Range-Doppler maps for a quadcopter when: (a) Throttle up. (b) Throttle down. (c) Pitch forward. (d) Pitch backward. (e) Roll left. (f) Roll right. . 49
4.7 Range-Doppler maps for a hexacopter when: (a) Throttle up. (b) Throttle down. (c) Pitch forward. (d) Pitch backward. (e) Roll left. (f) Roll right. . 50

4.8 Range-Doppler maps for: (a) Yaw left quadcopter. (b) Yaw right quadcopter. (c) Yaw left hexacopter. (d) Yaw right hexacopter. 51

4.9 Different classifiers accuracy when considering/Not considering the mechanical control information of UAVs. 52

4.10 Comparison of the classification reports for the three different CNN algorithms used in this work when: (a) Not considering the mechanical control information of UAVs. (b) Considering the mechanical control information of UAVs. 54

4.11 (a) A flowchart of the DopplerNet CNN algorithm. (b) Its confusion matrix when it is applied to the same dataset. 55

4.12 Confusion matrix for the DopplerNet CNN algorithm when (a) Not considering the mechanical control information of UAVs. (b) Considering the mechanical control information of UAVs. 55

4.13 A Confusion matrix for applying the proposed MCML algorithm to dataset 4. 56

4.14 Simulation setup for all motions scenario. 57

4.15 A confusion matrix of applying the DopplerNet classifier on the full motions scenario according to (a) The state-of-the-art literature. (b) The proposed MCML method. 57

4.16 Measurements setup of the DJI Phantom 3 standard quadcopter. 58

4.17 Range-Doppler images for DJI Phantom 3 standard when it: (a) Throttles up. (b) Pitches forward. 58

5.1 ROC curve depicting the detection probability of the TI radar. 63

5.2 (a) Top-view of the simulation setups for the UAVs at different angles. (b) The used SISO antenna (left) and MIMO antenna (right). 64

5.3 Range-Doppler images for the seven UAVs at a relative angle of 0°. (a) Fixed-wing. (b) Helicopter. (c) Quadcopter A. (d) Quadcopter B. (e) Quadcopter C. (f) Quadcopter D. (g) Hexacopter. 66

5.4 (a) The confusion matrix of the CNN algorithm at a relative angle of 0°. (b) A Comparison between the CNN classification accuracy using the SISO and the MIMO antennas at various relative angles. 67

5.5 The confusion matrices for testing the trained CNN model on synthetic datasets at different angles for both the SISO and MIMO antenna cases. (a) 20° SISO antenna. (b) 40° SISO antenna. (c) 60° SISO antenna. (d) 20° MIMO antenna. (e) 40° MIMO antenna. (f) 60° MIMO antenna. . 68

5.6 Experimental setups for quadcopter model D at different angles. (a) 0° setup. (b) 0° range-angle. (c) 0° range-Doppler. (d) 20° setup. (e) 20° range-angle. (f) 20° range-Doppler. (g) 40° setup. (h) 40° range-angle. (i) 40° range-Doppler. (j) 60° setup. (k) 60° range-angle. (l) 60° range-Doppler. 69

5.7 Experimental setups for quadcopter model D at different angles. (a) 80° setup. (b) 80° range-angle. (c) 80° range-Doppler. (d) 90° setup. (e) 90° range-angle. (f) 90° range-Doppler. 70

5.8 (a) Experimental setup for quadcopter model C. (b) range-Doppler map of quadcopter model C at a relative angle of 0° with respect to the radar. . . 71

5.9 (a) Classification results of the CNN algorithm for the real-measurements dataset at a relative angle of 0° with respect to the radar. (b) Classification results of the CNN algorithm for quadcopter D at different angles. 72

5.10 Range-Doppler maps for quadcopter D at relative angle of 40° using: (a) SISO antenna. (b) MIMO antenna. 72

5.11 Beamforming using an array of transmitters. 74

5.12 Signal processing algorithm for a MIMO radar system. 75

5.13 Signal processing algorithm for a beamforming (steering-only) radar system. 76

5.14 Signal processing algorithm for a beamforming-based RDIwS radar system. 76

5.15 Signal processing algorithm for a beamforming (steering and tracking) radar system. 77

5.16 ROC curves for the performance of the beamforming methods compared to a traditional MIMO radar system at false alarm probability of 10^{-5} when: (a) A UAV at a relative angle of 0°. (b) A UAV at a relative angle of 45°. (c) Two UAVs within the maximum power. (d) Two UAVs at a relative angle of ±45°. (e) Four UAVs within the maximum power. (f) Four UAVs at a relative angle of ±45°. (g) Four UAVs at different locations and different relative angles of ±45° and ±60°. 79

5.17 Comparison of the classification accuracy of different radar systems at different angles in case of only one UAV in the scene. 81

5.18 Simulation setup of multiple UAVs at different angles. 82

5.19 Range-angle maps for four different UAVs when using: (a) MIMO radar. (b) RDIwS beamforming-based method. 82

5.20 (a) A quadcopter UAV positioned 1 m in front of the radar at a relative angle of 60°. (b) Range-Doppler map of the quadcopter UAV using the traditional MIMO algorithm. (c) Range-Doppler map of the quadcopter UAV using the proposed RDIwS beamforming-based algorithm. 83

List of Tables

2.1 Comparison of UAV detection methods. 6

3.1 An example of radar parameters used in the literature 19
3.2 Radar parameters used in this work. 21
3.3 UAVs dimensions. 23
3.4 MIMO antenna specification. 30
3.5 The AWR1443 radar parameters. 31
3.6 Classification accuracy results of a UAV among avian subjects 39

4.1 Specified radar parameters. 48
4.2 Generated datasets. 52
4.3 The AWR1443BOOST TI radar configuration. 58

5.1 Dimensions of the used UAVs. 65
5.2 Radar configuration & antenna parameters. 65

List of Abbreviations

2DPCA Two-Dimension Principal Component Analysis 10

A-SPC Advanced Stationary Point Concentration 12

ADC Analog-to-Digital Converter 30

AESA Active Electronically Scanned Array 12

AI Artificial Intelligence 12

AIC Akaike Information Criterion 10

ALRO Adaptive Learning Rate Optimizing 8

AoA Angle of Arrival 12, 59, 60, 85

CAD Computer-Aided Design iv, 1, 4, 15, 16, 18, 21, 22, 24, 26, 28, 30–32, 84, 88, 89

CCW Counterclockwise 41, 44–46

CFAR Constant False Alarm Rate 8, 9, 77

CNN Convolutional Neural Network v, 7–11, 27, 28, 31, 32, 34, 35, 38, 51, 52, 55, 63, 65, 66, 69, 70, 84–87

CPU Central Processing Unit 26

CVD Cadence Velocity Diagram 9, 11

CW Clockwise 41, 44–46

CW Continuous-Wave 7, 11

CWT Continuous Wavelet Transform 10

DBN Deep Belief Network 11

DCNN Deep Convolutional Neural Network 11

DNN Deep Neural Network 10

DSP Digital Signal Processing 12

DT Decision Tree 51

DWT Discrete Wavelet Transform 10

EM Electromagnetic iv, 1, 4, 6, 8, 15, 16, 18, 21, 22, 24, 26, 28, 32, 84, 88

EMD Empirical Mode Decomposition 7, 8

FCC Federal Communications Commission 88

FFT Fast Fourier Transform 10, 16, 19, 20, 31, 61, 74

FMCW Frequency-Modulated Continuous-Wave 7–12, 16, 18, 19, 22, 63, 84

FOV Field of View v, 4, 13, 14, 58, 59, 66, 70, 73, 80, 82, 85, 86

GPU Graphics Processing Unit 26

HERM Helicopter Rotation Modulation 10

IF Intermediate Frequency 16, 17

IMFs Intrinsic Mode Functions 8

ISAR Inverse Synthetic Aperture Radar 11, 16, 34, 35

KNN K-nearest Neighbors 51

LFMCW Linear Frequency-Modulated Continuous-Wave 10

LOS Line of Sight 5, 6

LSTM Long Short-Term Memory 8

MCML Mechanical Control-Based Machine Learning iv, v, 4, 40, 50, 52, 55, 85, 86

MDL Minimum Description Length 10

MIMO Multiple-Input Multiple-Output v, 2, 4, 9, 11, 12, 16, 29, 58, 59, 61–63, 66, 67, 70, 72–74, 77, 80, 81, 83, 85, 86

ML Machine Learning iv, v, 1–6, 9, 13, 15, 16, 25, 27, 30, 32, 34, 35, 37, 40, 51, 52, 58, 63, 74, 79, 80, 82, 84–87, 89

mm-Wave millimeter-Wave 8, 9, 11, 18, 22, 27, 63

NB Naive Bayes 51

OMP Orthogonal Matching Pursuit 10

PCA Principal Component Analysis 11

PEC Perfect Electric Conductor 20, 32

RAM Random-Access Memory 26

RCS Radar Cross-Section 8, 9, 12–15, 18, 32, 52, 61, 77, 80

RDIwS Range-Doppler Integration while Steering v, 4, 59, 72–74, 76, 77, 79–81, 83, 86

ReLU Rectified Linear Unit 27, 52

RF Random Forest 51

RF Radio Frequency 5

ROC Receiver Operating Characteristics 62, 74, 77

RSP Radar Signal Processing 27

RX Receiver 59–64, 80

SDR Software Defined Radio 12

SIMO Single-Input Multiple-Output 2, 62, 85

SISO Single-Input Single-Output v, 2, 4, 58, 61–63, 66, 67, 70, 72, 85

SNR Signal to Noise Ratio v, 2, 4, 7–10, 12, 14, 27, 58, 59, 61, 62, 66, 70, 72, 74, 77, 79, 83, 85, 86

SPC Stationary Point Concentration 12

STFT Short-Time Fourier transform 10, 17

SVM Support Vector Machine 7, 8, 10, 11, 35, 38, 51

TI Texas Instruments 30, 55, 62–64, 67, 69, 82, 88

TVD Time Velocity Diagram 10

TX Transmitter 59, 61–64, 72, 80

UAV Unmanned Air Vehicle iv, v, 1–18, 21–24, 26–41, 44–47, 50–52, 55, 56, 58, 59, 62–67, 69–74, 76, 77, 79–89

YOLO You Only Look Once 13

List of Symbols

$X(\tau, \omega)$ Fourier Transform of the received signal 17

K Number of Columns for the Steering Matrix 60

e_l Additive Noise 59

K_f Aerodynamic Force Constant 42

K_m Aerodynamic Moment Constant 42

w Angular Velocity 18, 42

G Antenna Gain 61

d Antenna Spacing 63, 72, 73

A Area of a target 18

BW Bandwidth: The frequency range for the radar chirp 19, 30, 47, 57

f_{beat} Beat-frequency: Radial frequency of the down-converted beat signal in Hz 19, 59, 60

f_0 Center frequency: center frequency on chirp bandwidth or linear frequency sweep 19, 30, 47, 57

$\boldsymbol{R}$ The Covariance Matrix 60

σ Radar Cross Section: is the effective area that intercepts the transmitted radar power and then scatters that power back to the radar receiver. 18, 61

f_D Doppler Frequency 17, 20

A_e Effective aperture of the received antenna 61

t_f Fast time: The sampling time within a chirp in a given frame 16, 59

$\mathbf{\Gamma}$ A factor depends on a channel's magnitude and phase mismatch 60

$HPBW$ Half power beam width 19, 47

$\boldsymbol{I}$ Inertia Matrix 43

$\boldsymbol{x}$ The beat signal at the l^{th} antenna element 60

λ Wavelength: Wavelength associated with the center frequency 18, 61

L Length between two propellers 42

F Lifting Force 42–45

c Speed of light: A constant describing the speed of light 299,792,458 m/s 19

b_l Channel's Magnitude Mismatch 59

m Mass 43

R_{max} Maximum Range 19, 30, 47, 57

λ_{max} Maximum wavelength: Wavelength associated with minimum chirp frequency 59

M Moment 42

$\boldsymbol{R_n}$ The Noise Covariance 60

N_0 Receiver Noise 61

α_l Channel's Phase Mismatch 59

τ_l Phase Shift 59

ϕ Azimuth Angle of Arrival 20

Θ Pitch Angle 43

r Position 43

v_r Radial Velocity 18, 20, 59, 60

r Blade Radius 18

$RP(R, t_s)$ Range profile across the frame: Obtained after applying the FFT to the received signal in the IF domain. 17

ΔR Range Resolution 19, 30, 47, 57

$RDM(R, f_D)$ Range-Doppler map 17

P_r Received Power 61

$X_r(t_f, t_s)$ Received Signal Waveform 17

$\Delta\psi_l$ Residual Phase Noise 59

Φ Roll Angle 43

T_m Signal Period 19

P_s The Signal Power 60

t_s Slow time: The sampling time across different chirps in a given frame (i.e., the chirp index) 16, 59

$\Omega(\tau)$ STFT Window Function 17

$S(\tau, \omega)$ Spectrogram of the received signal 17

$\boldsymbol{A}$ Steering Matrix 60

$\boldsymbol{a}$ Steering Vector 60

R Target distance: Position of the target. 17, 19, 61

θ Elevation Angle of Arrival 20

P_t Transmitted Power 61

ΔV Velocity Resolution 19, 30, 47, 57

V Vertical Polarization 19, 47

mg Weight 43–45

Ψ Yaw Angle 43

Chapter 1

Introduction

1.1 Motivation

Due to the wide availability of Unmanned Air Vehicles (UAVs) all over the world, they have become widely used in illicit activities, such as drug and weapons smuggling to prisons or across borders, interference with airplanes, privacy invasion, and in terrorist attacks [7, 8, 9, 10, 11, 12, 13, 14, 15, 16]. Therefore, it is important to identify and classify UAVs from other targets for safety and security purposes. For this, the detection and classification of UAVs at a distance is required. Radar-based systems are preferred in comparison with radio sensors, optical, and acoustic systems due to their advantages in this application. Radar systems work anytime during the day, and in bad weather conditions, they can detect multiple UAVs at a time, track autonomous UAVs, classify them when combined with Machine Learning (ML) models [17, 18, 19, 20, 21].

Generating radar datasets that contain UAVs information to train ML algorithms is one of the most important limitations in this application [17]. This process is costly and time-consuming. Also, these measurements are limited by radar parameters, available UAVs, and the background environment. Most importantly, the number of available radar UAVs datasets are very limited, and they can be used only considering the types of UAVs and the radar parameters used in their work [22, 23, 24, 25, 26]. Having the ability to use full-wave Electromagnetic (EM) Computer-Aided Design (CAD) tools, it is possible to overcome this limitation and generate multiple datasets that represent a large number of complex scenarios in an effective, easy, and low-cost way.

Additionally, UAVs are widely classified using their range-Doppler information and micro-Doppler signatures [27, 28, 29]. In the state-of-the-art literature, radar UAVs'

datasets were generated by taking radar measurements of hovering and/or pitching UAVs only. Consequently, ML algorithms were trained and tested on the same datasets that contain the same motions. The range-Doppler information of UAVs is found to be highly dependent on the mechanical control information of UAVs. ML classification accuracy significantly decreases when they are applied to new datasets that contain different motions of the UAVs. By considering the mechanical control information of UAVs in the generated datasets, it is possible to overcome this limitation and enhance the capability of ML algorithms to correctly classify UAVs if they are applied to new datasets with different motions of these UAVs.

Furthermore, the relative angles between UAVs and a radar's antenna and the number of UAVs in a scene significantly affect the radar's capabilities to detect and classify these UAVs. Although using Multiple-Input Multiple-Output (MIMO) radar systems enhance the detection of UAVs compared to Single-Input Single-Output (SISO) or Single-Input Multiple-Output (SIMO) radar systems [30, 31, 32, 33, 34, 35, 36, 37, 38, 39, 40, 41, 42, 43, 44, 45], MIMO radars struggle to detect and classify UAVs at wide relative angles. Beamforming is considered one of the significant advancements in the field of antenna technology and signal processing for the detection and classification of UAVs. By using radar beamforming, the detection probability of UAVs is increased by electronically focusing the antenna beam at a specific angle. Additionally, radar beamforming improves spatial resolution of UAVs and raises the Signal to Noise Ratio (SNR) for them, ensuring the detection and classification of small UAVs [46, 47, 48, 49, 50, 51, 52, 53, 54, 55].

1.2 Objective

The primary goal of this thesis is to increase radar systems' capabilities of detecting and classifying UAVs. This can be attained by achieving four main objectives:

1. A new reliable and valid method for generating radar datasets that contain UAVs information in an effective, easy, and low-cost way is needed. This method should overcome the limitations of generating radar datasets using real-measurements. The generated datasets should be used to enhance the detection probability of UAVs and increase the classification accuracy of ML algorithms by training them on a large number of complex scenarios.

2. A new method to overcome the degraded ML classification accuracy when the mechanical control information of UAVs is not taken into consideration is needed as the

existing literature doesn't consider the mechanical control information of UAVs in their datasets.

3. An investigation on the impact of the relative angles between the UAVs and a radar's antenna on the classification accuracy of ML algorithms is needed. This investigation is crucial because existing literature predominantly trained and tested ML algorithms with a fixed angle of 0° between the antenna and the UAVs. Furthermore, it is essential to examine the effects of multi-UAV classification at various angles. This inquiry is needed since the existing literature often neglects the classification of multiple UAVs within a scene simultaneously.

4. An enhancement of the radar signal processing to effectively increase the radar system's capabilities to detect and classify multiple UAVs at different angles is required.

1.3 Thesis Outline

As shown in Figure 1.1, the structure of this thesis is as follows:

- Chapter 2: A literature survey on the different systems used in detecting and classifying UAVs is presented. In addition, a detailed literature survey on the state-of-the-art

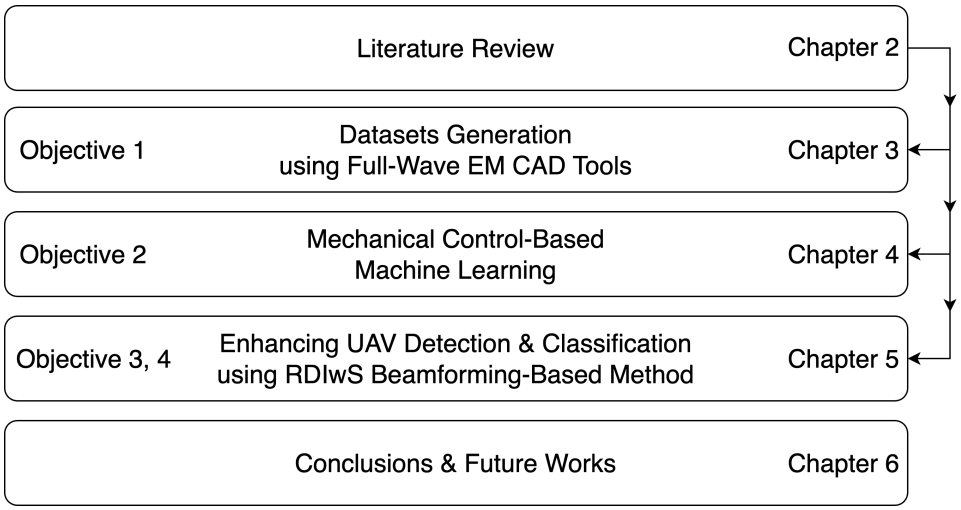


Figure 1.1: Flowchart of the thesis outline.

literature in the field of UAV detection and classification using radar-based systems is presented.

- Chapter 3: Dataset generation using full-wave EM CAD tools is introduced and validated. The method overcomes the limitations of generating real-measurement datasets using radar systems. In addition, the importance of using full-wave EM CAD tools in countering radar deception techniques is presented.

- Chapter 4: A Mechanical Control-Based Machine Learning (MCML) method is introduced to overcome the degradation in ML classification accuracy when the mechanical control information of UAVs is not taken into consideration. The method uses all the basic mechanical control information of UAVs to train ML algorithms to avoid the degradation in ML accuracy to classify UAVs when they applied to new datasets representing different motions.

- Chapter 5: An investigation on the impact of the Field of View (FOV) of a SISO and a MIMO radar systems is presented. Additionally, a Range-Doppler Integration while Steering (RDIwS) beamforming-based method is introduced to increase the SNR of UAVs located at wide relative angles and in particular in the case of multi-UAV classification at different angles, which significantly enhance the detection and classification of UAVs.

- Chapter 6: Closing remarks and system limitations, recommendations for system performance improvements, and finally, a summary of publications.

Chapter 2

Radar-Based UAV Detection: A Literature Review

2.1 Introduction

The illicit applications of Unmanned Air Vehicles (UAVs) underscore the need for an early detection system that can swiftly and precisely provide information about UAVs. Three primary methods are commonly used for the detection of UAVs: acoustic, optical, and and Radio Frequency (RF) [17, 18, 19, 20, 21]. Acoustic methods, known for their ease of installation and relatively low cost, do not necessarily demand a Line of Sight (LOS) to detect the presence of UAVs. These methods can also be effectively combined with Machine Learning (ML) algorithms for classification. Conversely, acoustic methods are limited in their ability to facilitate long-range detection and are notably susceptible to interference from ambient noise in the surrounding environment. Optical methods, when integrated with ML algorithms, offer a robust solution with the capability to capture actual images of the target, track autonomous UAVs, and are generally considered a cost-effective option, falling within the low to medium cost range. However, optical systems are susceptible to weather conditions, require a LOS to effectively detect UAVs, and in the case of utilizing thermal cameras, small UAVs may not emit sufficient heat for reliable detection. In RF detection methods, radio sensors and radar-based systems are commonly employed. In radio sensor detection, a receiver is used to intercept RF communications between the UAVs and its controller. This approach is considered a cost-effective solution, falling within the low to medium-cost range. It not only detects the positions of both the UAVs and its controller but also has a low false alarm rate. Moreover, it is capable of detecting

Table 2.1: Comparison of UAV detection methods.

Method	Acoustic	Optical	Radio Sensors	Radars
LOS Independence	✓	×	×	×
Long Range Detection	×	×	✓	✓
Weather Conditions	×	×	✓	✓
Detect Autonomous UAVs	✓	✓	×	✓
Classify UAVs and Birds	×	✓	×	✓
Compatibility with ML	✓	✓	✓	✓
Detect Controller Location	×	×	✓	×

UAVs from long distances. On the other hand, radio sensors cannot detect autonomous UAVs as there is no communication between a UAV and its controller. Additionally, they struggle to detect a large number of UAV simultaneously and require a LOS for effective operation. Radar-based detection systems, unlike optical methods, remain unaffected by adverse weather conditions and operate effectively both during the day and at night. These systems can track autonomous flights and can successfully detect and track multiple UAV simultaneously. When integrated with ML algorithms, they can classify various targets and differentiate between different types of UAVs. However, radar-based detection systems are considered a high-cost solution compared to other detection systems, and they require a LOS to detect UAVs [17, 18, 19, 20, 21].

Table 2.1 summarizes the key differences between the four UAV detection methods. As demonstrated, comparing various detection methods, radar systems offer numerous advantages over other techniques. This thesis primarily focuses on enhancing the detection and classification of UAVs using radar systems, leveraging their superior capabilities [17, 18, 19, 20, 21]. In section 2.2, state-of-the-art literature on the radar-based UAV detection systems is presented.

2.2 State-of-the-Art Literature

Radar systems transmit Electromagnetic (EM) waves, when an object is illuminated by transmitted waves, some of the EM waves are scattered back toward the radar. This phenomenon indicates the presence of a target(s) [56, 57]. Radar technology has historically played a crucial role in aerial surveillance, enabling the accurate detection and tracking of airborne objects. This has been particularly significant in the context of UAV detection and classification, as radar systems have become a focal point. The increasing prevalence of

UAV utilization in various applications, along with their varying sizes and functionalities, has emphasized the pressing need for robust detection and classification methods. Radar systems have extensively been explored as a powerful tool UAV detection and classification.

In [58], a low-cost radar-based system for UAV detection and classification is presented, distinguishing UAVs from common urban objects. It utilizes a two-step process, initially extracting micro-Doppler features and providing preliminary classifications. Subsequently, it combines data from successive time segments to make the final determination. In [59], the challenge of classifying multiple UAVs and birds based on micro-Doppler signatures is addressed. It introduces three protocols and demonstrates the most effective one for distinguishing UAVs from birds in real observation scenarios using radar and a Convolutional Neural Network (CNN). In [29], an X-band radar system is used for UAV detection. Experimental results with measured radar signals show a good performance in detection accuracy and computational efficiency. In [27], micro-Doppler signatures of a small UAV are used. Experimental results show the potential of micro-Doppler features for UAV detection and classification. In [28], an iterative adaptive technique for enhancing Doppler processing in ground-based surveillance radar systems used for UAV detection is proposed. The method overcomes limitations in dwell time and improves Doppler resolution, resulting in better discrimination of micro-Doppler signatures and accurate UAV classification.

In [60], micro-Doppler signatures for distinguishing UAVs and birds using radar data are explored. An accuracy of 96% in UAV and bird classification and 85% accuracy in classifying individual UAVs and birds into five categories are achieved using Support Vector Machine (SVM). In [61], micro-Doppler signatures are extracted from spectrograms and cepstrograms to distinguish between birds and small UAVs. In [62], a method uses the micro-Doppler effect and pattern recognition is presented to identify UAVs in real-time with accuracy. In [63, 64], an analysis of micro-Doppler features from small UAVs using a 94 GHz radar in Continuous-Wave (CW) and Frequency-Modulated Continuous-Wave (FMCW) modes is discussed in the first work. Wavelet decomposition extracts high-frequency components corresponding to small UAV movements, and time-frequency analysis is employed for feature visualization and interpretation. In the second work, radar micro-Doppler properties of UAVs and birds are explored. Experimental measurements were conducted using K-band and W-band radars with various UAV models and bird species. The results demonstrate that both radar frequencies can retrieve reliable and distinct micro-Doppler signatures, with the W-band radar having a higher Signal to Noise Ratio (SNR).

In [65, 66, 67], various methods for mini-UAV classification based on radar data are explored. The first approach employs Empirical Mode Decomposition (EMD) to extract oscillating waveforms from radar echo signals, which are then used to derive features cap-

turing blade flashes for classification using a nonlinear SVM. In the second work, FMCW radar returns from various UAVs and non-UAV objects in terms of micro-Doppler signatures are analyzed. Based on this analysis, it uses a UAV classification system consisting of five key components: burst selection, rule-based scan pruning, EMD-based micro-Doppler analysis and feature extraction, error counting minimization for class label estimation, and scan-to-scan filtering. The third investigation delves into the challenges posed by the weak micro-Doppler signals from small UAV rotor blades, using EMD to extract the rotation components effectively, which has been validated as a viable method for UAV identification. In [68], six entropies extracted from Intrinsic Mode Functions (IMFs) for radar-based mini-UAV classification are investigated. Three entropies are selected due to their efficiency and accuracy and are used in combination with different sets of IMFs to improve classification accuracy.

In [69], EM waves scattering from micro-UAV rotor blades are studied, considering factors like polarization, frequency, and azimuth angle. Both simulations and experiments reveal variations in scattering with azimuth and frequency. In [70], Radar Cross-Section (RCS)-based statistical system for classifying UAVs is presented at microwave frequencies. It begins with RCS measurements of six commercial UAVs at various frequencies and different polarization. It shows that the UAVs' RCS depends on factors like shape, size, material, azimuth angle, frequency, and polarization. Statistical models are used to characterize the UAVs, leading to a recognition system with an average accuracy exceeding 97.60% at an SNR of 10 dB. In [22], RCS measurements on different UAVs at $26-40$ GHz are conducted for two categories: carbon fiber and plastic UAVs. It is shown that larger carbon fiber UAVs are easier to detect, while plastic UAVs are less visible. In [71], improved UAV classification using millimeter-Wave (mm-Wave) radar, used in [22], and deep learning is presented. It introduces an efficient Long Short-Term Memory (LSTM) model with a weight optimization technique and Adaptive Learning Rate Optimizing (ALRO). The LSTM-ALRO approach achieves a high UAV detection accuracy of 99.88%. In [23], a system for UAV detection and classification using persistent range-Doppler radar is presented. It combines a Constant False Alarm Rate (CFAR) detection stage with a CNN for classification. It classifies UAVs, cars, and people with an accuracy of 99.48%. In [24], using a 77 GHz radar, a CNN classifier's ability to discriminate UAVs from non-UAV targets, such as birds, is evaluated when they are not represented in the training data. It is shown that the mean accuracy for out-of-distribution UAVs is 78%. By introducing a synthetic UAV class created through a mathematical model, the accuracy improves to 86%. When trained on all UAV types, the mean accuracy across all classes reaches 90%.

In [72], a model for micro-Doppler effects to analyze UAV signatures is introduced. It focuses on the number of UAV motors and their rotation speed. The model is validated

by comparing simulated radar images with data from a 77 GHz FMCW Multiple-Input Multiple-Output (MIMO) radar. Results demonstrate the model's accuracy in classifying UAVs based on the number of motors, with motor rotation speed not significantly affecting the classification. In [73], a system to automatically classify UAVs from other objects, especially birds is introduced. It proposes a complex-log-Fourier transform to better handle micro-Doppler signatures, addressing the phase spectrum. Additionally, it presents a dimension-reduction technique called subspace reliability analysis, reducing the error rate from 6.68% to 3.27% compared to the Cadence Velocity Diagram (CVD). In [74], classification features from micro-Doppler signatures are extracted and employs eigenpairs from correlation matrices for classification, showing an accuracy of 95% of to classify different UAVs and birds.

In [75, 76], a multi-static radar system is used to study UAVs carrying payloads. The first study distinguishes between hovering and flying UAVs with different payloads, achieving over 96% accuracy in payload weight classification. The second study employs domain transformations and CNN to classify UAVs with or without payloads, achieving approximately 95.1% accuracy for hovering UAVs and 96.6% for flying UAVs. In [77], a multi-static radar is used with three steps signal processing algorithm. A CFAR is used to detect the targets, micro-Doppler signatures are used to discriminate the detected targets, and finally, a Kalman filter is used to track the targets over time. In [78], radar measurements of small UAVs using a multi-static radar system at L- and X-bands are presented. It includes range-time plots, micro-Doppler signatures, and a quantitative analysis of signal quality. The study achieved over 90% classification accuracy for distinguishing UAVs from other objects using simple features and classifiers.

In [79, 80], an investigation on the effect of SNR on UAV-bird classification using radar data is conducted. It is shown that classification accuracy drops with lower SNR. Data augmentation improves accuracy at low SNR levels, achieving an overall accuracy of 92%. In [81], a K-band radar system with high sensitivity for detecting low RCS targets and measuring their range and velocity is introduced. It employs fiber-optic links to reduce leakage and platform designs to minimize ground reflections. In [82], micro UAV detection in rocky terrain using a 24 GHz dual-polarized FMCW radar is explored. It deals with land clutter, using a CFAR detector, and enhances UAV discrimination by extracting and plotting the micro-Doppler signature of rotating propellers and the UAV's trajectory in the time-frequency domain. In [83], a precise UAV detection and localization system using mm-Wave radar, combining spatial heatmaps, micro-Doppler analysis, and Gaussian process regression to improve accuracy over direct spectral analysis is proposed. In [84] micro-Doppler results using FMCW radar and ML are used to locate and classify UAVs, achieving an accuracy of 85.1% in classifying four UAV models. In [85], a CNN algorithm

is applied to the Continuous Wavelet Transform (CWT) and Discrete Wavelet Transform (DWT) scalogram of reflected radar signals from UAVs. In [86], a clutter suppression method using an Orthogonal Matching Pursuit (OMP) algorithm for Linear Frequency-Modulated Continuous-Wave (LFMCW) radar is presented. The method reduces clutter power and extracts micro-Doppler signals for distinguishing different UAVs in low SNR conditions.

In [87], radar micro-Doppler is used to detect and classify small UAVs based on their movements. Radar measurements of UAVs and birds are analyzed using Time Velocity Diagram (TVD), and a boosting classifier is employed for target detection and classification offering advantages over the SVM classifier. In [88], UAVs are recognized using micro-Doppler features generated by rotor rotation. A Fast Fourier Transform (FFT) and Two-Dimension Principal Component Analysis (2DPCA) are applied to extract features efficiently without high-dimensional data conversion. The method achieves a 98.44% recognition rate for small UAVs, reducing computational complexity and feature extraction time. In [89], a method for detecting and recognizing rotor UAVs based on their micro-motion characteristics is presented. It compensates for translational motion, estimates micro-Doppler parameters, and enhances target detection and identification. In [90], FMCW radar signal models are examined in the presence of UAVs, and an approach for high-frequency micro-Doppler signature analysis is introduced. In [91], the limitations of micro-Doppler methods for detecting small UAVs with weak radar returns from plastic propellers are addressed. A rotary UAV detector based on the number of Helicopter Rotation Modulation (HERM) lines is introduced and two parametric methods are evaluated, Minimum Description Length (MDL) and Akaike Information Criterion (AIC), for HERM line estimation.

In [92], the challenging task of distinguishing between rotary-wing UAVs and flying birds using K-band FMCW radar is addressed. A data augmentation method is used to enhance the collected dataset. A CNN model is used to improve feature extraction and reduce computational complexity, achieving high classification accuracy. In [93], CNN models are utilized to classify UAVs based on radar signals, using Short-Time Fourier transform (STFT) spectrograms. In [94], a method for tracking and recognizing low-altitude UAVs and birds using traditional surveillance radar data is introduced. It establishes motion models, filters and smoothes target trajectories, calculates model occurrence probabilities, and identifies target types. In [95], a data augmentation method for generating simulated radar micro-Doppler signatures to classify UAVs is presented. It demonstrates that using this method to train a Deep Neural Network (DNN) improves accuracy. The study focuses on classifying the number of UAV motors using a 77 GHz radar system, achieving a classification accuracy of 78.68%.

In [25, 26], a dataset of micro-Doppler signatures from various small aerial targets is developed in the first work and transfer learning-based Deep Convolutional Neural Network (DCNN) is used, achieving high classification accuracy. The second work introduces a lightweight DCNN model, for accurate detection and classification of small UAVs based on their micro-Doppler signatures, achieving a classification accuracy of 97.1% to 97.3%. In [96], the radar signatures of various consumer UAVs through laboratory measurements are examined. The UAVs are rotated on a turntable, and their back-scattered radar data are collected at two different frequency bands. The data are then processed to create Inverse Synthetic Aperture Radar (ISAR) images.

In [97, 98, 99], UAVs are classified based on micro-Doppler signatures created by rotor blade rotation in the first work. It suggests using both K-band and X-band radar data to enhance accuracy. Spectrograms are formed, Principal Component Analysis (PCA) extracts features, and SVM is used for classification. Dual-band radar fusion outperforms single-band radar in classification accuracy. In the second work, direct-path and multi-path micro-Doppler radar signatures are combined to improve micro-UAV classification accuracy in urban environments, achieving a 5% increase in accuracy. The third work introduces a recognition method for multiple micro-UAVs based on their micro-Doppler signatures using dictionary learning, with a 93% recognition performance in indoor environments when trained on half of the measured data. In [100], a method for localizing and classifying UAVs using mm-Wave FMCW radar is presented. The UAV's height and distance are estimated, and the UAV's activity is classified with lightweight models like logistic regression, SVM, and a CNN. In [101], a UAV classification method that utilizes a CNN and micro-Doppler signatures is presented. Micro-Doppler signatures and CVD are combined to create a merged Doppler image, which is processed by a CNN model. In [102], the effectiveness of W-band radar for detecting small UAVs and emphasizes radar's reliability in challenging scenarios are discussed. The advantages of FMCW radar in the mm-Wave range are highlighted, including compactness and suitability for various surveillance applications, especially when other sensors may be less effective. In [103], a radar system for detecting and classifying micro UAVs based on Doppler signatures and spectral correlation functions is introduced. It employs a Deep Belief Network (DBN) for classification and achieves over 90% accuracy in UAV detection and classification using a 2.4 GHz CW Doppler radar in lab experiments.

In [35, 36, 37, 38, 39, 41], MIMO radars are used to improve the detection and classification of UAVs. The first work emphasizes enhancing UAV detection by utilizing range-velocity processing and micro-Doppler analysis for improved classification. The second work discusses the development of a mm-Wave FMCW radar system for detecting small UAVs, addressing technology challenges and performance expectations. The third work

presents a low-cost 2×2 MIMO radar prototype developed with Software Defined Radio (SDR) technology and evaluates its performance in detecting slow-moving, low RCS micro-UAVs. The fourth work introduces a low-cost S-band MIMO radar system designed for detecting small UAVs and employing calibration methods to improve target SNR. The fifth work proposes two methods for fast subspace computation and accurate Angle of Arrival (AoA) acquisition, leveraging randomized low-rank approximation for high-resolution environmental sensing. The sixth work introduces an end-to-end detection and tracking framework for multiple micro-UAVs using FMCW-MIMO radar, addressing low SNR challenges.

In [104, 105, 106], a Stationary Point Concentration (SPC) technique is introduced in the first work to address challenges related to phase noise in radar systems. The SPC technique reduces noise by concentrating it on a stationary point, and it can be implemented using Digital Signal Processing (DSP) without additional hardware. In the second work, issues in heterodyne FMCW radar systems are addressed, including increased noise and unwanted Doppler shifts in the range-Doppler map. The authors introduce an enhanced SPC technique that mitigates noise and corrects Doppler shifts, improving SNR and velocity information for small moving UAVs. While in the third work, limitations in the SPC technique are identified and an Advanced Stationary Point Concentration (A-SPC) technique is introduced. The A-SPC method is designed to address the drawbacks of the SPC technique while retaining its advantages.

In [107, 108, 109, 110], in the first work, a method is proposed to extract a symmetry feature from micro-Doppler signatures of UAV targets, maintaining explainable Artificial Intelligence (AI) for safety applications. In the second work, the use of micro-Doppler signatures for differentiating UAVs from other objects, like birds is highlighted. It also explores how the signatures vary with different UAV component shapes. It involves the design and performance of a 94 GHz radar for lab-based micro-Doppler measurements. In the third work, the classification of UAV types using micro-Doppler signatures is addressed. It presents a simulation approach that models UAV components as point clouds derived and compares simulated results with experimental data. In the fourth work, models to simulate radar returns from multi-rotor UAVs using real motor speed data are created, generating synthetic spectrograms that capture the micro-Doppler features.

In [46, 49, 52, 55], Active Electronically Scanned Array (AESA) technology and its advantages are introduced in the first work for airborne radar systems, emphasizing its flexible antenna design and adaptable configuration. In the second work, a radar system for commercial UAV detection in the X-band is presented, achieving detection up to 2 km and discussing detection figures and RCS studies. The third work introduces an X-band radar system demonstrator and its signal processing, demonstrating UAV detection and

tracking up to 3 km, highlighting its advantages for surveillance tasks. In the fourth paper a new method that combines moving surveillance radar with computer vision, You Only Look Once (YOLO) network, is presented to jointly detect and classify UAVs. The approach uses full spatial coverage radar data and achieves over 99% in accuracy. All four works focus on radar digital beamforming technology, including radar detection and capabilities.

2.3 Unaddressed Aspects in Literature Review

Following a comprehensive review, at the beginning of this research, of the state-of-the-art literature in the field of radar-based UAV detection and classification, several key limitations have been identified. These limitations have a significant effect on the detection and classification of UAVs using radar-based systems. The following is a list of the main limitations that this thesis highlights:

1. The lack of comprehensive and different datasets that are required for training and testing ML algorithms.
2. The constraints, complexity, and considerable cost involved in generating a large number of real-measurement datasets to train and evaluate ML algorithms and develop signal processing techniques.
3. ML algorithms were trained and tested on the same datasets which did not consider the mechanical control information of UAVs.
4. The impact of a radar's antenna FOV on the classification accuracy of UAVs was not investigated.
5. Multi-UAV detection and classification at wide angles with respect to the radar was not investigated.
6. The physically small dimensions of UAVs, resulting in a small RCS, subsequently lead to a significant reduction in their detection probability.

The efficiency of radar-based UAV detection and classification systems is significantly impacted by these limitations. The ability to develop ML algorithms that can reliably classify various UAVs in a variety of scenarios is limited by the lack of adequate datasets. Additionally, generating real-world measurements is resource-intensive, which imposes practical limitations and high expenses that could prevent research and development activities.

Given that such information is essential for comprehending the flight characteristics of UAVs, the absence of mechanical control information in the training and testing datasets further limits the ability to improve classification accuracy. The oversight regarding the radar's antenna FOV and its impacts on classification accuracy highlights a critical gap in current research. Additionally, the exclusion of multi-UAV detection and classification at wide angles relative to the radar represents a limitation in addressing scenarios where multiple UAVs may be involved. The low RCS of UAVs resulting from their small sizes leads to a reduction in their SNR, this is one of the main concerns in the field of radar detection and classification of UAVs. These limitations have to be addressed in order to increase the radar systems' capabilities in the field of detection and classification of UAVs. In the following chapters, the details on addressing the limitations mentioned above are presented; chapter 3 addresses the first and second limitations, while chapter 4 addresses the third limitation, and finally, chapter 5 addresses the fourth, fifth, and sixth limitations.

Chapter 3

UAV Classification using Machine Learning and Full-Wave EM CAD Tools

3.1 Introduction

Training Machine Learning (ML) algorithms on radar datasets that contain Unmanned Air Vehicles (UAVs) information is mandatory to increase ML algorithms capability to correctly classify UAVs. To generate these datasets, it is essential to conduct radar measurement campaigns. However, these measurements are limited by many factors such as the availability of different UAV types, the radar parameters, and the background environments. Additionally, these measurements are costly and time-consuming [111]. Furthermore, there are very few publicly available datasets on the detection and classification of UAVs, and they can only be used when taking into account the different kinds of UAVs that were used, the radar's specifications, the UAVs' operating ranges, and the environments in which the measurements were made [111, 22, 23, 24, 25]. To overcome these constraints, numerical simulations provide a reliable alternative method. In the state-of-the-art literature [93, 108, 109, 110, 112, 113, 114, 115], several studies attempted to mathematically simulate the Radar Cross-Section (RCS) of UAVs and the spectrograms of rotor blades on UAVs, or they used Computer-Aided Design (CAD) models of propellers, generating micro-Doppler signatures by converting 3D CAD models to point clouds. In some of these efforts, as in [113], the simulations take up to 160 hours to finish. However, a key difference that sets our proposed method apart from prior efforts is that we mimic

UAV motion using full-wave EM CAD tools that cover more than just rotor blade rotation. Our use of time-based full-wave analysis, a novel feature built into our method, further emphasizes this uniqueness. Furthermore, our approach not only facilitates the generation of micro-Doppler signatures of UAVs but also produces a wide range of results including but not limited to range profiles, waterfalls, range-Doppler maps, Inverse Synthetic Aperture Radar (ISAR) images, and range-angle maps when Multiple-Input Multiple-Output (MIMO) radars are used.

In this chapter, full-wave Electromagnetic (EM) CAD tools are introduced to perform time-based full-wave analysis of UAVs in different scenarios to generate radar datasets that contain UAVs information in a fast, easy, and reliable way. The simulations are performed using Ansys HFSS [116] as a proof of concept. Using this method, radar datasets can be generated without many constraints. The generated datasets using the proposed method can be effectively used to train ML algorithms. In addition, radars can be designed and evaluated in the UAV and radar fields before expensive production campaigns. Also, the attempts taken to deceive radar systems can be investigated using the proposed method. Researchers and engineers can create more effective defenses and detection systems by simulating the behavior of radar systems and examining how they react to various UAV configurations and flight paths. Due to its many important advantages, the suggested methodology represents a significant advancement in the field of UAV detection and classification.

Most UAVs generate micro-Doppler signatures as a common feature, and these signatures have been widely used to classify radar objects. Subsequently, range-Doppler maps and micro-Doppler signatures are used in the classification process of UAVs, for example [27, 28, 29, 60, 61, 62, 63, 64]. Frequency-Modulated Continuous-Wave (FMCW) radars are frequently used in the field of UAV detection and classification due to their advantages [56, 57]. Figure 3.1 illustrates the procedural steps involved in the generation of range-Doppler maps in FMCW radars. In the FMCW operation, a frame is transmitted, consisting of multiple chirps, as depicted in Figure 3.1. The transmitted signals are received back after scattering from various objects. The received signals are then mixed with the transmitted ones through a local oscillator to obtain the Intermediate Frequency (IF) signals. Then, to obtain the range-Doppler maps, the following process is applied: it starts by applying a FFT to the fast-time axis, t_f, executed for each chirp, resulting in the acquisition of range information for each chirp. Subsequently, another FFT is applied to the slow-time axis, t_s, encompassing the entire frame. This operation captures changes in range across the chirps, yielding both Doppler information and the final range-Doppler

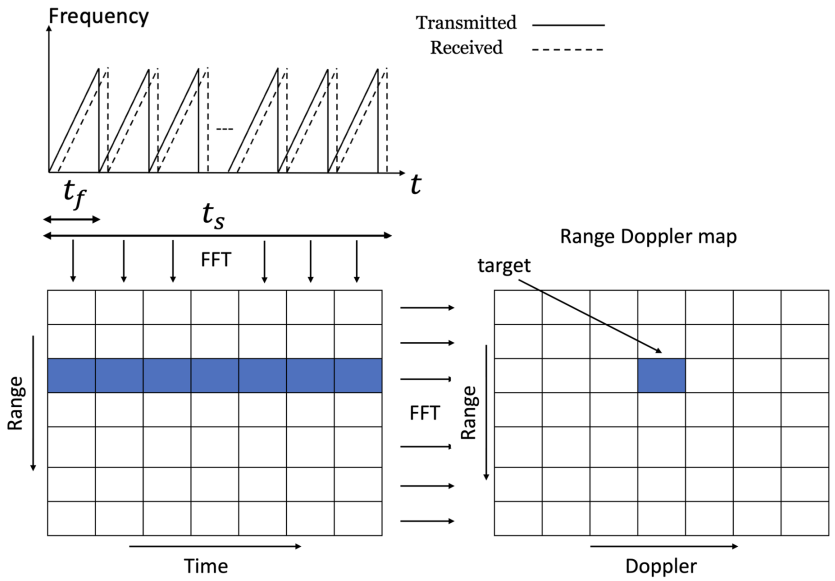


Figure 3.1: Range-Doppler maps generation for FMCW radars.

maps [23]. This process can be represented as follows:

$$\begin{aligned} RP(R, t_s) &\Leftrightarrow FFT\{X_r(t_f, t_s)\} \\ RDM(R, f_D) &\Leftrightarrow FFT\{RP(R, t_s)\} \end{aligned} \tag{3.1}$$

where $X_r(t_f, t_s)$ is the received radar signal in the IF domain, $RP(R, t_s)$ represents the range profile across the whole frame, and $RDM(R, f_D)$ represents the range-Doppler map, which is a two-dimensional representation of the radar echoes in the range (R) and Doppler frequency (f_D) domains.

While the micro-Doppler signatures, spectrograms, of UAVs are generated by applying a Short-Time Fourier transform (STFT) to the radar received signal to analyze its frequency over time. The received signal is divided into segments or windows in which STFT is applied to represent the signal's frequency content. The length of each window is chosen to balance the trade-off between time and frequency resolutions as shown in (3.2) [74, 61, 64, 60, 88, 67, 86, 92]:

$$X(\tau, \omega) = \int_{-\infty}^{\infty} X_r(t)\Omega(t - \tau)e^{-j\omega t}dt \tag{3.2}$$

where $\Omega(\tau)$ denotes the window function and $X(\tau, \omega)$ denotes the Fourier transform of the received signal's segment according to the window length. Then, the spectrogram representation is obtained by taking the magnitude squared of the STFT in logarithmic

scale as shown in (3.3) [74, 61, 64, 60, 88, 67, 86, 92]:

$$S(\tau, \omega) = 10 \log_{10} |X(\tau, \omega)|^2 \tag{3.3}$$

where $S(\tau, \omega)$ is the spectrogram of the received signal in a logarithmic scale. This representation is useful for visualizing signals with a wide range of power spectral density in the logarithmic scale, as it compresses the dynamic range of the spectrogram.

3.2 Radar Datasets Generation

To generate the required datasets for this work, six different types of UAVs are considered. The UAVs are modeled based on commercially available UAV models. Ansys HFSS [116] is used to model the UAVs and generate the range-Doppler maps for the required datasets. The range-Doppler and micro-Doppler responses of the radar system, obtained from full-wave EM CAD tools, are first validated.

3.2.1 Methodology Validation

Due to the smaller physical size of UAVs, their RCS is relatively small. For instance, at 9 GHz frequency, the mean RCS of the DJI Phantom 4 [117] is 0.04 m^2 [118]. The RCS of a radar target depends on different factors with the used frequency being the most important one [119].

$$RCS(\sigma) = \frac{4\pi A^2}{\lambda^2} \tag{3.4}$$

where σ is the RCS of a target, A is the target's area, and λ is the signal wavelength. The RCS increases with the increase in frequency, as shown in (3.4). For example, the mean RCS for the Walkera UAV is -12.5 $dBsm$ at 26 GHz and is -8.5 $dBsm$ at 40 GHz [22].

Due to their wide bandwidth, millimeter-Wave (mm-Wave) radars are widely used in the literature in the field of UAV detection and classification [22, 24, 71, 100, 102]. An investigation is conducted to evaluate the impact of using different radars with different frequency bands on the range-Doppler accuracy of a rotating blade. A 1 m blade is modeled to rotate in its position with an angular velocity of 100 rad/s at a distance of 50 m away from the radar, as shown in Figure 3.2. Three radars, previously used in this field, are chosen for this investigation, L-band, X-band, and W-band radars [79, 65, 90]. The

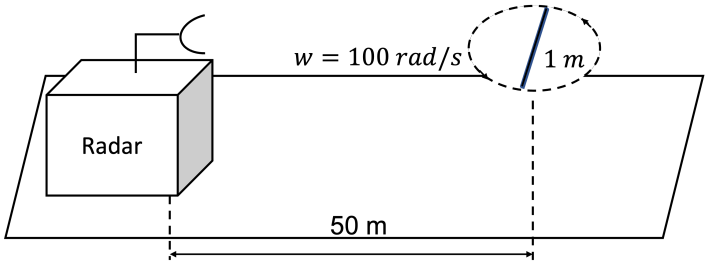


Figure 3.2: One rotating blade.

Table 3.1: An example of radar parameters used in the literature

Radar	**Center Frequency** f_0	BW	**Range Resolution** ΔR
L-Band	1.5 GHz	2 MHz	75 m
X-Band	9.7 GHz	80 MHz	1.875 m
W-Band	77 GHz	4 GHz	3.75 cm

parameters for the three radars are shown in Table 3.1. Based on the range and velocity resolutions, and according to equation (3.5):

$$v_r(m/s) = w(rad/s) \times r(m) \tag{3.5}$$

where v_r is the radial velocity, w is the angular velocity, and r is the blade radius, a maximum radial velocity of ± 50 m/s should be achieved. As shown in Figure 3.3a–d, the W-band radar, due to its wide bandwidth, has the highest accuracy compared with the other radars.

Based on the results shown in Figure 3.3a–d, a mm-Wave FMCW radar is chosen to validate the range-Doppler and micro-Doppler signatures results obtained through full-wave EM CAD tools, and to model the six UAVs to generate the required datasets for this work. For simplicity, a BW of 300 MHz is selected, while the used radar parameters are summarized in Table 3.2.

In FMCW radars, the range is determined from the beat frequency, f_{beat}, which is obtained by subtracting the transmitted waveform from the received waveform as shown in equation (3.6) [23]:

$$R = \frac{f_{beat} c T_m}{2BW} \tag{3.6}$$

where R represents the range to the target, f_{beat} is the beat frequency, T_m is the signal period, c is the speed of light, and BW is the signal bandwidth. The beat frequency f_{beat}

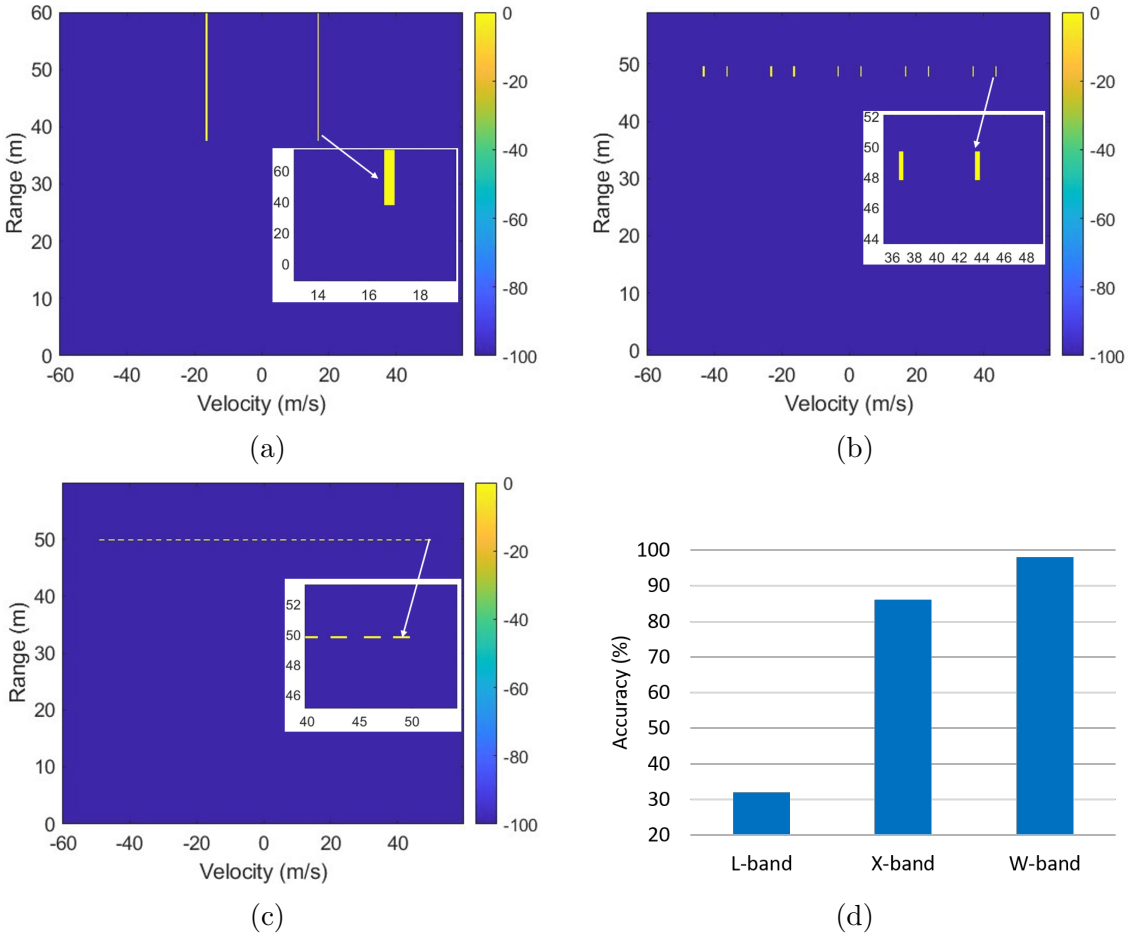


Figure 3.3: Range-Doppler images of the rotating blade with different radars. (a) L-Band. (b) X-Band. (c) W-Band. (d) Range-Doppler Accuracy Results.

is computed by performing a Fast Fourier Transform (FFT) on the fast-time axis of the received signal. To determine the Doppler velocity of the target, a second FFT is applied to the slow-time axis of the signal, which results in the range-Doppler information as shown in equation (3.1) [23]. The radial velocity of an object, v_r, is determined by [119]:

$$f_D = \frac{2v_r}{\lambda} cos\theta cos\phi \tag{3.7}$$

where f_D is the doppler frequency, θ and ϕ are the angle of arrival in the elevation and azimuth planes, respectively.

In order to validate the range-Doppler results, a "like" pendulum simulation is conducted, as shown in Figure 3.4a. A Perfect Electric Conductor (PEC) sphere of 0.5 m

Table 3.2: Radar parameters used in this work.

Quantity	Symbol	Value
Center Frequency	f_0	77 GHz
Bandwidth	BW	300 MHz
Range Resolution	ΔR	0.5 m
Velocity Resolution	ΔV	0.4 m/s
Maximum Range	R_{max}	60 m
Antenna Beam Width	$HPBW$	60°
Antenna Polarization	V	Vertical

radius is modeled to move in a straight line in front of the radar from a distance of 5 m to a distance of 55 m. The sphere's initial velocity at a distance of 5 m is 0 m/s, with an acceleration of 0.5 m/s^2, its velocity reaches its maximum value of 5 m/s at a distance of 30 m. Then, the sphere decelerates with a deceleration of -0.5 m/s^2 to reach 0 m/s at a distance of 55 m. Figure 3.4b,c show the range and Doppler velocity results of the sphere. It is shown that the range and Doppler information obtained through the proposed method are accurate.

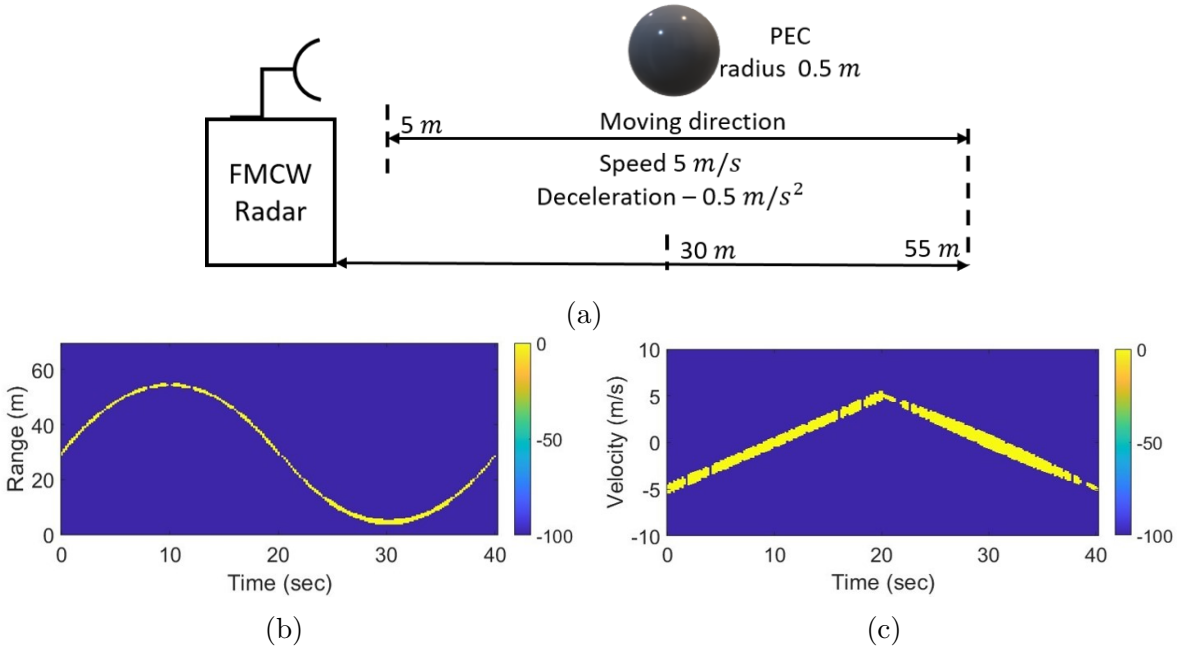


Figure 3.4: (a) A "like" pendulum simulation setup. (b) Range values. (c) Doppler velocity values.

The micro-Doppler signature of UAVs is affected by the number of blades in a rotor. A rotor for a UAV commonly contains either one, two, three, or four blades. In [112], mathematical analysis is done on the frequency variations brought on by the interference brought on by the rotation of one, two, and three blades. Convolution theory is applied in the time and frequency domain to accomplish this. Analyses are conducted at a frequency of 24 GHz and a wavelength of 1.25 cm. Rotor models with one, two, and three blades, each with a length of 1 m and rotating at a rate of 10 π rad/s, are investigated.

In order to validate the micro-Doppler results, simulations are conducted using a full-wave EM CAD tool similar to the simulations described in [112], using the same radar parameters. The simulation results for the cases of one, two, three, and four blades are shown in Figure 3.5a–d. The spectrogram results in Figure 3.5 align with the spectrogram results as presented in the work of [112].

Figure 3.4b,c, Figure 3.3c, and Figure 3.5a–d validates the range-Doppler and micro-Doppler results obtained by full-wave EM CAD tools concerning the utilization of radars for the detection and classification of UAVs.

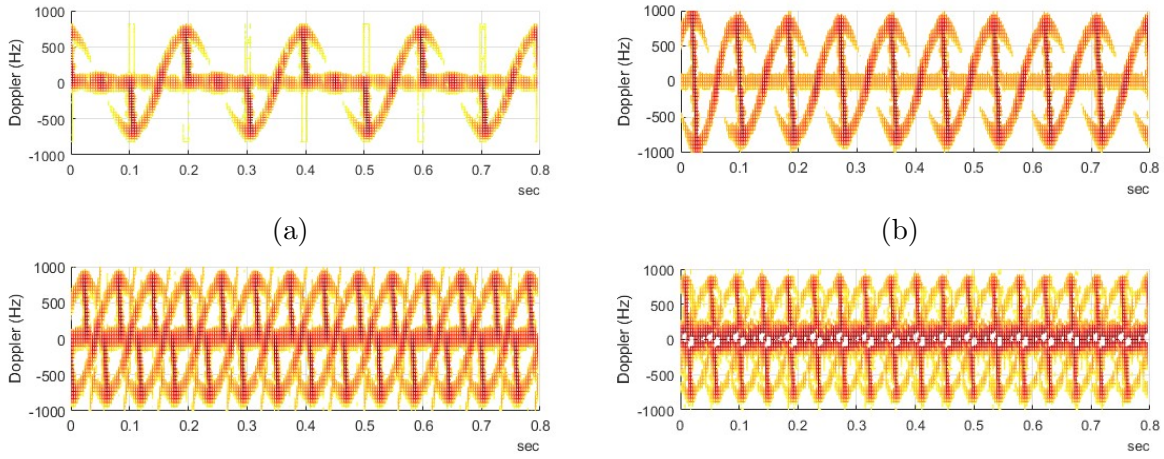


Figure 3.5: Spectrogram results for (a) One blade rotor. (b) Two blades rotor. (c) Three blades rotor. (d) Four blades rotor.

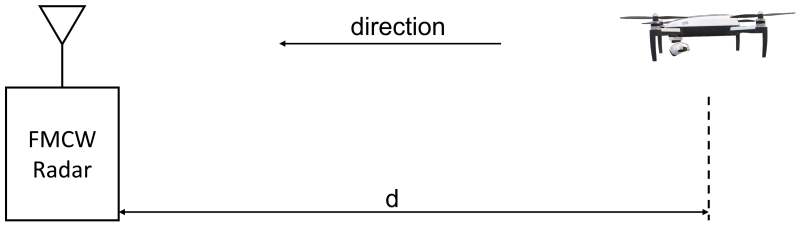


Figure 3.6: Simulated test setup for the six different types of UAVs using Ansys HFSS.

3.2.2 Datasets Generation

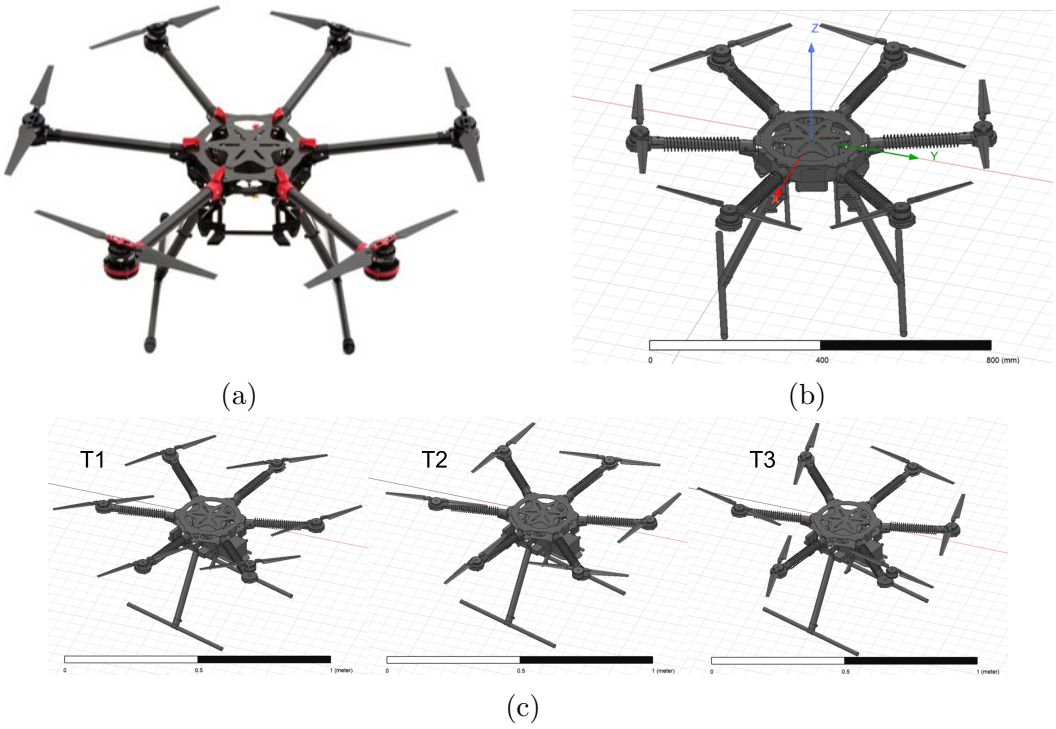
Six different types of UAVs are modeled using a full-wave EM CAD tool. The six UAVs are a fixed-wing, a helicopter, 3 quadcopters, and a hexacopter. They are modeled according to the Albatross UAV [120, 121], the Black Eagle 50 UAV [122], the DJI FPV UAV [123], the MD4-1000 UAV [124, 125], the Phantom 3 standard UAV [126], and the DJI S900 UAV [1], respectively. The dimensions of these UAVs are shown in Table 3.3. A W-band FMCW radar is used to generate the datasets required for this work, its parameters are shown in Table 3.2.

The six UAVs are modeled to pitch forward to the radar from a distance of 55 m with 5 m/s velocity, this distance is chosen to match the state-of-the-art literature using mm-Wave radars for this application [22, 24, 100, 71, 102]. Figure 3.6 shows the Ansys HFSS simulation setup used to generate the required datasets for this work. For example, Figure 3.7a–c show the DJI S900 hexacopter UAV, its corresponding model in Ansys HFSS, imported from [127], and three-time stamps for the modeled UAV showing the rotation of its blades, respectively, while the other UAVs follow a similar approach.

Figure 3.8a–f shows the range-Doppler maps obtained through Ansys HFSS for the

Table 3.3: UAVs dimensions.

UAV	**Type**	**Dimensions** (m)
Albatross	Fixed-wing	0.74 × 0.2 × 0.15
Black Eagle 50	Helicopter	2.65 × 0.56 , blade 3.75
DJI S900	Hexacopter	Diagonal 0.9, Arm 0.358
DJI FPV	Quadcopter	0.178 × 0.232 × 0.127
MD4-1000	Quadcopter	1.136 × 1.730 × 0.495
Phantom 3	Quadcopter	Diagonal 0.35, blade 0.24



(a) (b)

(c)

Figure 3.7: (a) The DJI S900 hexacopter UAV [1]. (b) HFSS model for the DJI S900 hexacopter UAV. (c) Three-time stamps for the modeled DJI S900 hexacopter UAV showing the rotation of its blades.

Albatross, Black Eagle 50, DJI FPV, MD4 1000, DJI Phantom 3 standard, and DJI S900 UAVs, respectively. To obtain results using the proposed method, the following procedure is used:

1) In the Ansys HFSS design environment, generate a 3D model of the UAV and its surroundings. The dimensions and configuration of the UAV, as well as the terrain, structures, and any other things that can have an impact on radar scattering, must all be specified.

2) To ensure a proper depiction of the structures and the electromagnetic waves interacting with them, apply an appropriate mesh to the geometry.

3) Assign the UAV and the nearby objects the proper material attributes. A material library containing frequently used materials is provided by full-wave EM CAD tools, and custom materials can have particular electromagnetic characteristics.

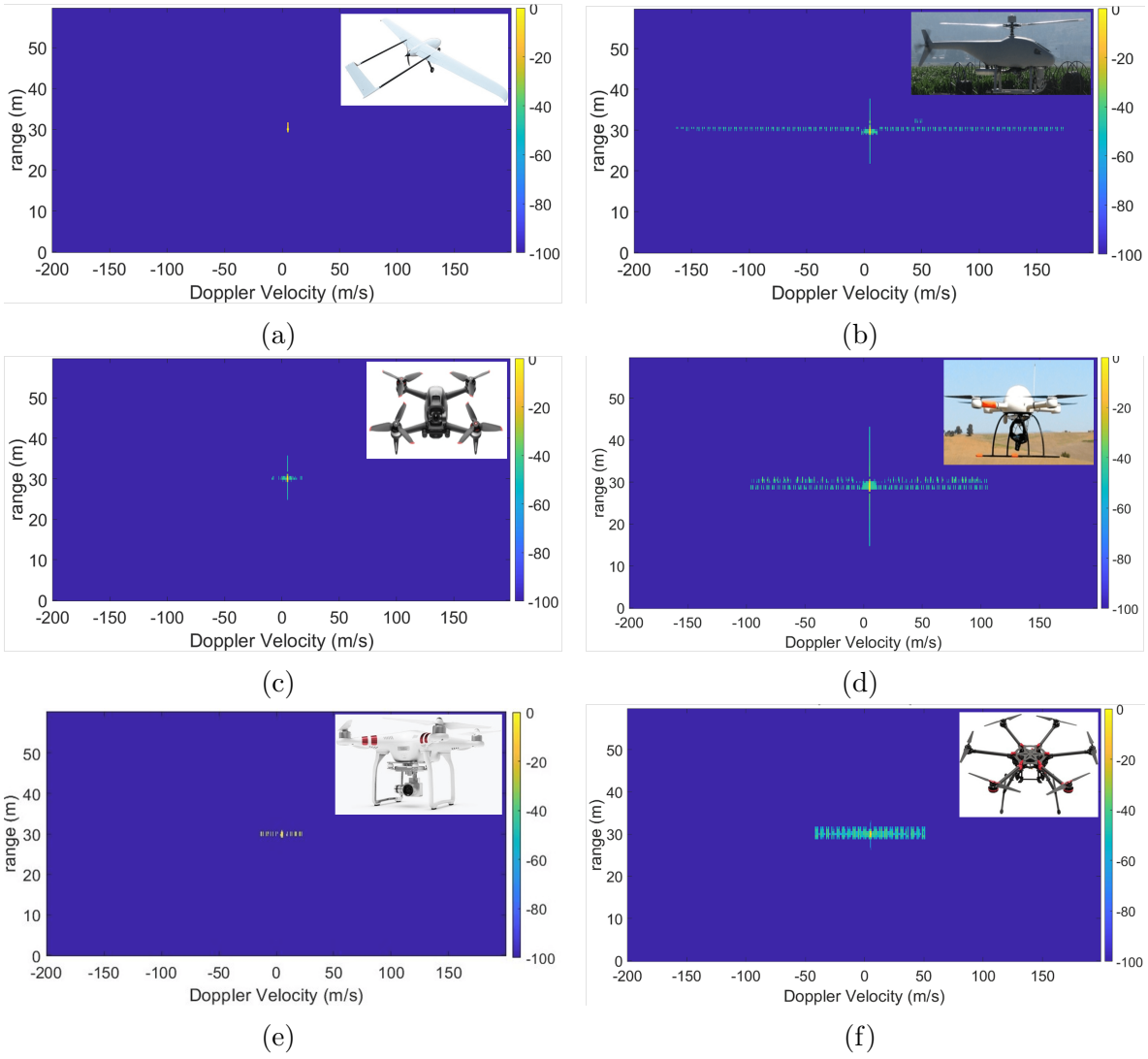


Figure 3.8: Range-Doppler images for the: (a) Fixed-wing UAV. (b) Helicopter UAV. (c) Hexacopter UAV. (d) DJI FPV quadcopter UAV. (e) MD4-1000 quadcopter UAV. (f) DJI Phantom 3 standard quadcopter UAV.

4) Define the electromagnetic wave parameters of the radar system, such as frequency, polarization, and incidence angle. The simulation will be excited using this data, and the UAV scattering behavior will be examined.

5) To guarantee that the simulated waves propagate correctly in the intended directions and prevent undesirable reflections or diffractions, set up the proper boundary

conditions.

6) Set the solver settings, frequency range, and convergence requirements, among other simulation parameters.

7) A path, speed, and acceleration have to be defined for the UAVs to traverse.

8) Analyze and display the results when the simulation ends.

9) ML algorithms are trained by the generated datasets.

The computational requirements, including the time needed for simulations, are influenced by various factors. These factors include but are not limited to:

- **Simulation Size:** Computational requirements are directly influenced by the size and complexity of the simulation model, including the number of components, the complexity of the geometry, and the mesh density.
- **Frequency Range:** The number of frequency points that must be solved depends on the spectrum of frequencies being considered in the simulation, which also affects how long the simulation lasts.
- **Solver Settings:** Different solver variables, such as accuracy thresholds and convergence requirements, affect the amount of computing effort and simulation duration.
- **Hardware Specifications:** The computer equipment used to run the simulations, including the number and kind of Central Processing Unit (CPU) cores, memory size, and availability of Graphics Processing Units (GPUs), becomes essential in deciding how long the simulations take to run.
- **Parallelization:** The capacity to parallelize simulations across many CPU cores is provided by full-wave EM CAD tools, and the number of cores used may have an impact on the speed of the simulation.
- **Waveform and Time Step:** The choice of waveform and time step can influence how long computations take.
- **Materials and Dispersive Models:** Dispersive materials and models may increase simulation complexity and increase calculation time.
- **Solver Technology, Software Version, and License:** Simulation performance can be influenced by the specific solver technology and the type of license used.

To efficiently utilize computing power and reduce simulation time in full-wave EM CAD tools, it is essential to carefully consider these factors and fine-tune simulation settings. For example, considering the setup shown in Figure 3.6, and running the simulation on a system with the specifications of a 3.5 GHz 6-core processor, 64 GB of Random-Access Memory (RAM), and no GPUs, the simulation time for generating 200 range-Doppler frames for a single UAV is about 15 minutes. Conversely, the identical simulation performed on the same system equipped with an NVIDIA GeForce RTX 4060 GPU yields completion in under 10 seconds. It is noted that in contrast to prior works, such as [113], the simulations take a significantly longer duration of around 160 hours for *much simpler* simulations, while our proposed method achieves faster simulations within a matter of seconds (or minutes without using GPUs).

3.3 Classification Results

Traditional Radar Signal Processing (RSP) methods have exhibited certain limitations regarding target classification [128]. This section focuses on applying a ML algorithm to a dataset generated using the proposed method. A dataset containing a total of 1200 range-Doppler frames is generated using the proposed method, 200 frames for each UAV. Before classification, the frames are normalized and a threshold is applied to them. The ML algorithm is implemented in Python using Keras of TensorFlow [129]. Previous studies [23, 24, 59, 80, 85, 92, 93, 101] have shown that CNN is a powerful algorithm for classifying UAVs. In particular, the DopplerNet algorithm is utilized to classify the six types of UAVs [23]. To avoid over-fitting, a Maxpooling layer is added to this algorithm. The flow chart of the CNN algorithm used in this work is illustrated in Figure 3.9a, which consists of seven layers.

In order to match the chosen range and velocity resolutions, the input layer's dimensions are set to $1000 \times 120 \times 1$. A convolutional layer with 32 filters, a 3×3 kernel, and Rectified Linear Unit (ReLU) activation function is applied, yielding an output size of $998 \times 118 \times 32$. A Maxpooling layer, 2×2, follows the convolutional layer to reduce the algorithm's complexity, and its output size is $499 \times 59 \times 32$. A flatten layer is used to reshape the previous feature map into a vector with an output size of $942,112$. Three dense layers are used, of which two have a ReLU activation function and an output size of 64. Finally, the output layer uses a Softmax activation function to calculate the probability of each of the six classes.

The algorithm's hyperparameters include 10 epochs, a batch size of 10, and the Adam optimizer [130]. These specific hyperparameter values were selected following experimenta-

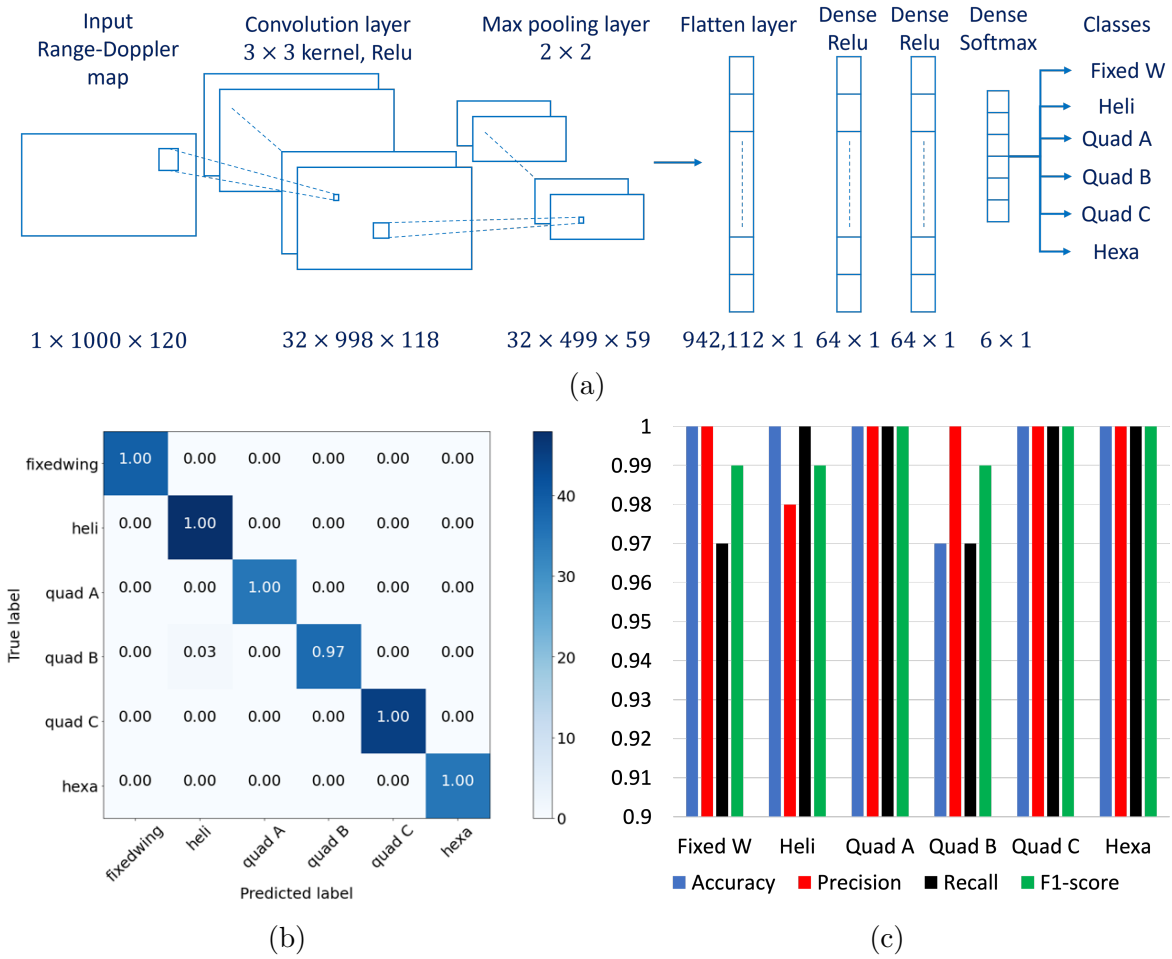
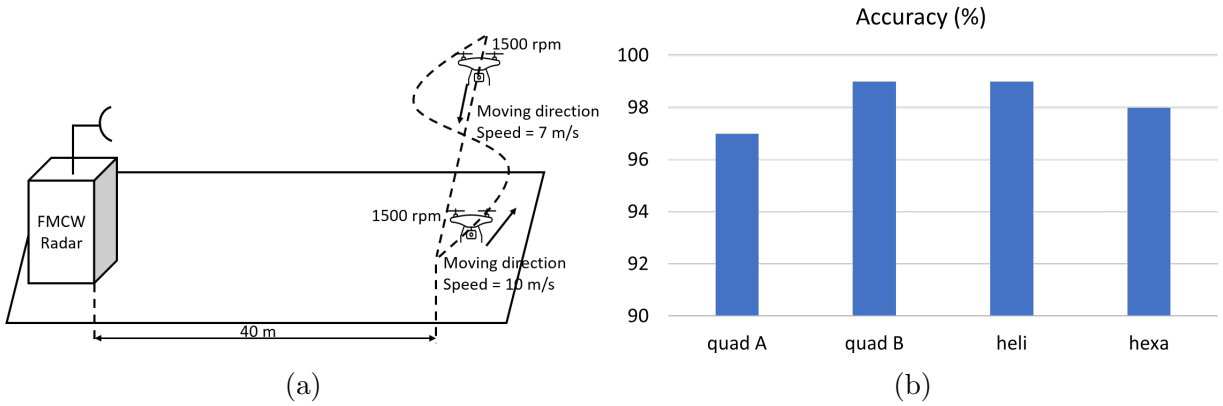


Figure 3.9: (a) A flowchart of the used CNN algorithm. (b) The confusion matrix result for the CNN algorithm. (c) The classification report for the used CNN algorithm.

tion with different settings, revealing that they yield optimal training/test accuracy. The dataset is divided into a training set and a test set with a ratio of 80% and 20%, respectively. The accuracy of the algorithm is found to exceed 97%. The confusion matrix for this algorithm and the classification report are presented in Figure 3.9b,c, respectively. It is worth noting that the DJI FPV quadcopter, the MD4-1000 quadcopter, and the DJI Phantom 3 standard quadcopter are respectively denoted as quadcopter model A, quadcopter model B, and quadcopter model C. As previously indicated, the selection of a 55 m distance aligns with current practices in mm-Wave radar applications for this application. However, extending the range will result in a lower SNR for UAVs, given the inverse



(a) (b)

Figure 3.10: (a) Simulated test setup for a new scenario. (b) Classification accuracy of applying the trained CNN algorithm to a new scenario for different UAV types.

fourth-power relationship with range. This decrease in SNR may impact radar-based detection and classification. A potential mitigation involves employing radars with higher transmitted power and implementing signal processing techniques to enhance the SNR of UAV signals, thereby improving the overall efficacy of UAV detection and classification.

As mentioned above, six different kinds of UAVs that are all flying directly in the direction of the radar are used to train the CNN algorithm. The CNN algorithm is tested on a completely new situation to further evaluate the method of producing UAV datasets using full-wave EM CAD tools. In this situation, there are two identical UAVs; one goes in front of the radar in a straight line from right to left, while the other proceeds in a curved route from left to right, as shown in Figure 3.10a. In contrast to earlier situations, when only one UAV was going directly in the direction of the radar, the current scenario comprises two identical UAVs moving in two distinct directions. The ability of the trained CNN algorithm to classify the UAVs in this new scenario is evaluated, yielding an accuracy of over 97%. The corresponding classification accuracy results for different UAV types are presented in Figure 3.10b.

Furthermore, another scenario is developed that involves the DJI FPV quadcopter and the DJI S900 hexacopter existing together, as shown in Figure 3.11. In this case, the quadcopter took a different route, aligning itself with an azimuth angle of $-30°$ and a different velocity profile, while the hexacopter followed a trajectory that is oriented toward the radar at an azimuth angle of $35°$. To efficiently detect and determine the number and azimuth orientations of the objects, the scenario used a MIMO antenna design, which is described in Table 3.4. The range-angle map is presented in a polar form in Figure 3.11.

A OneVsOneClassifier [131], ideally adapted for the difficulties associated with multi-

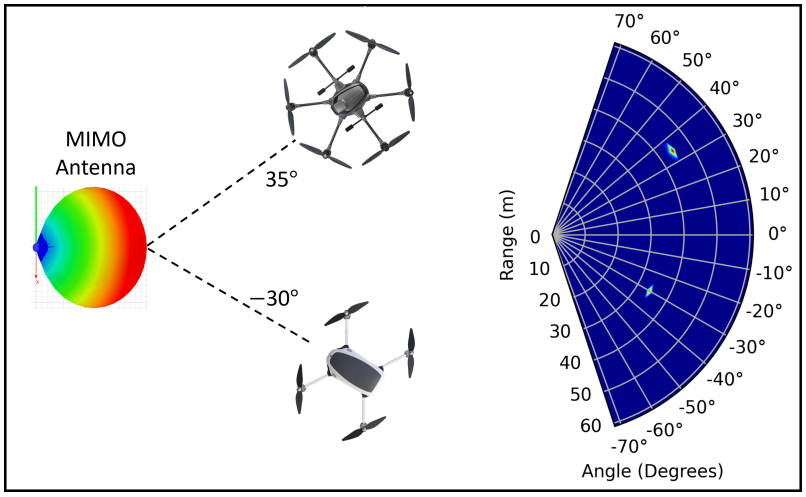


Figure 3.11: A hexacopter and a quadcopter model A in the same scene.

Table 3.4: MIMO antenna specification.

Quantity	**Value**
Antenna Beam Width	60°
Antenna Gain	0 dB
Output Power	1 W
Antenna Polarization	Vertical
Number of Channels	32 (4 TX & 8 RX)
Spacing between Antennas	2.05 mm
FOV	±71.86°
Angular Resolution	4.64°

label classification scenarios, underwent thorough training using the dataset produced by the setup outlined in Figure 3.6. After that, the newly created dataset resulting from the scenario including the simultaneous presence of both UAVs depicted in Figure 3.11 is subjected to the trained OneVsOneClassifier. The classifier shows high accuracy in correctly classifying the two UAVs, obtaining a classification accuracy exceeding 96%.

The AWR1443BOOST radar [2] from Texas Instruments (TI), which is shown in Figure 3.12 is used to test the viability of applying a ML model trained on CAD-generated radar dataset to categorize real-measurements data. A lab-measurements dataset of range-Doppler maps for a DJI Phantom 3 standard quadcopter UAV is generated using this radar. The acquired dataset is used to assess the process for CAD-generated radar datasets.

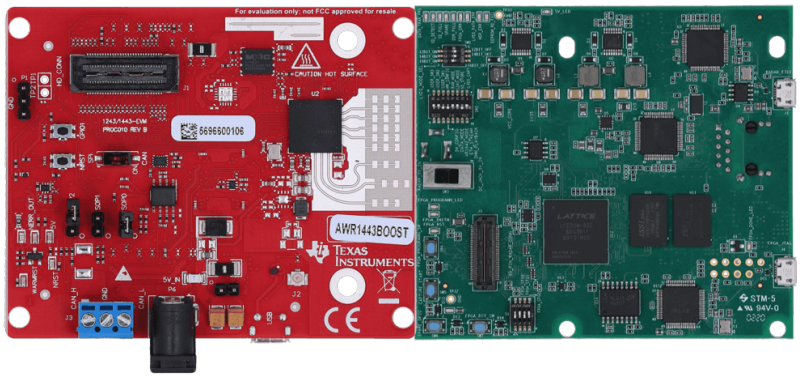


Figure 3.12: The AWR1443BOOST TI radar (left in red) [2] and the DCA1000EVM board (right in green) [3].

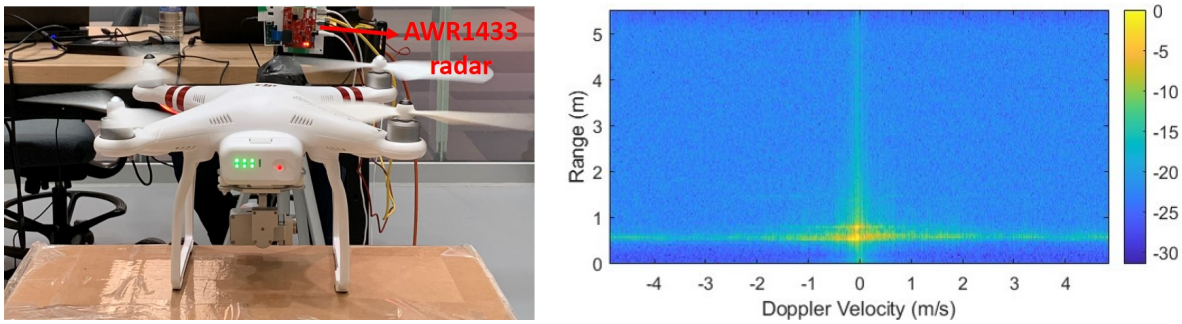
A DCA1000EVM board [3] is utilized to record the Analog-to-Digital Converter (ADC) data for the AWR1443BOOST TI radar, which operates between 76 and 81 GHz. The AWR1443BOOST radar specifications used for this study are shown in Table 3.5.

Table 3.5: The AWR1443 radar parameters.

Quantity	**Symbol**	**Value**
Center Frequency	f_0	77 GHz
Bandwidth	BW	3.460 GHz
Range Resolution	ΔR	0.0433 m
Velocity Resolution	ΔV	0.0174 m/s
Maximum Range	R_{max}	5.5 m

The DJI Phantom 3 standard UAV was placed at a distance of 0.5 m in front of the AWR1443BOOST radar, as shown in Figure 3.13a. A total of 514 range-Doppler frames are generated using the AWR1443BOOST radar. By applying a stationary clutter removal algorithm and performing an FFT on the fast-time axis of the received signal, the range information of the DJI Phantom 3 Standard UAV was obtained. Subsequently, a second FFT was conducted on the slow-time axis to extract the UAV's Doppler velocity, resulting in a range-Doppler image shown in Figure 3.13b.

The CAD-generated radar dataset is resized to match the dimensions of the range-Doppler maps acquired using the AWR1443BOOST radar due to the constraints in maximum range and velocity values of the AWR1443BOOST radar. The range-Doppler pictures



(a) (b)

Figure 3.13: (a) Lab-measurements setup for the DJI Phantom 3 standard. (b) Range-Doppler image for the DJI Phantom 3 standard using the AWR1443BOOST TI radar.

captured by the AWR1443BOOST radar are classified using the CNN classifier trained on the CAD-generated dataset. The CNN classifier demonstrates a high level of accuracy when tested on the new dataset. As mentioned earlier, 514 range-Doppler frames are generated utilizing the AWR1443BOOST radar. Among all the frames, 96% are correctly classified as DJI Phantom 3 Standard, while erroneously 2% are classified as MD4-1000 quadcopter UAV, 1% as DJI FPV quadcopter UAV, and the remaining 1% are classified as fixed-wing UAV. The findings of this study illustrate the high degree of accuracy of the proposed methodology to generate radar datasets that contain UAVs information using full-wave EM CAD tools. The research also emphasizes the potential of using these datasets to train ML systems.

3.4 Countering Radar Deception

This section emphasizes the significance of the proposed method in looking at attempts to deceive radar systems. These efforts involve lowering the RCS of UAVs by altering their design and material selection. This makes it more challenging to detect them. Utilizing materials that can absorb or deflect radar signals, often known as radar-absorbing material or stealth coatings, makes it harder for radar systems to detect UAVs. Additionally, one method for deceiving radar systems involves altering the UAV's blade length to change its Doppler signature. It is significant to note that mounting explosives on common UAVs is another trick that may be used.

Figure 3.9b demonstrates that the classification accuracy of the DJI Phantom 3 standard is 100%. The classification accuracy drops to 75% when the blade length is changed

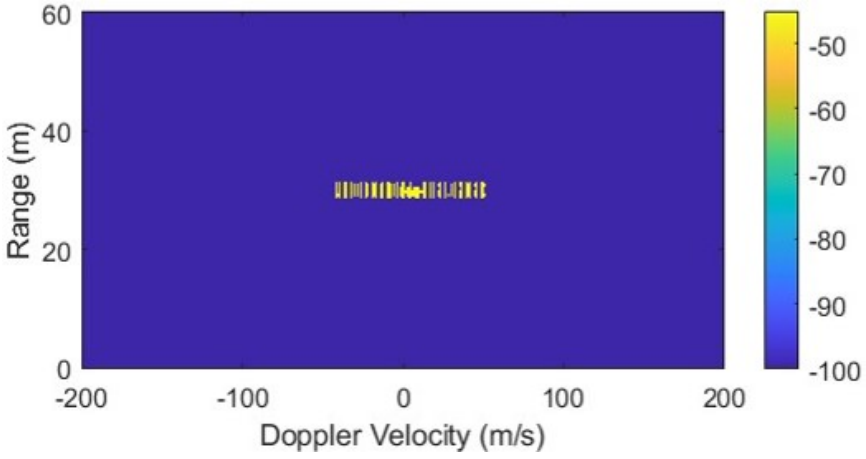
from 12 *cm* to 9 *cm*, with the remaining 25% being assigned to the DJI FPV UAV, which has a 9 *cm* blade length. The Doppler signature of UAVs is influenced by the blade length, indicating that the classifier takes into account both Doppler data and RCS when classifying UAVs. The accuracy of the classification process still declines from 100% to 75% despite the inclusion of RCS, leading to a 25% chance of radar deception.

Additionally, by altering the electrical material characteristics of the simulated UAV, as shown in Figure 3.14a,b, it is possible to study the effects of adding absorbing materials to UAVs. This may be done by selecting a different material for a UAV. In this experiment, the material of the DJI S900 hexacopter UAV is switched from PEC to plastic as a proof of concept.

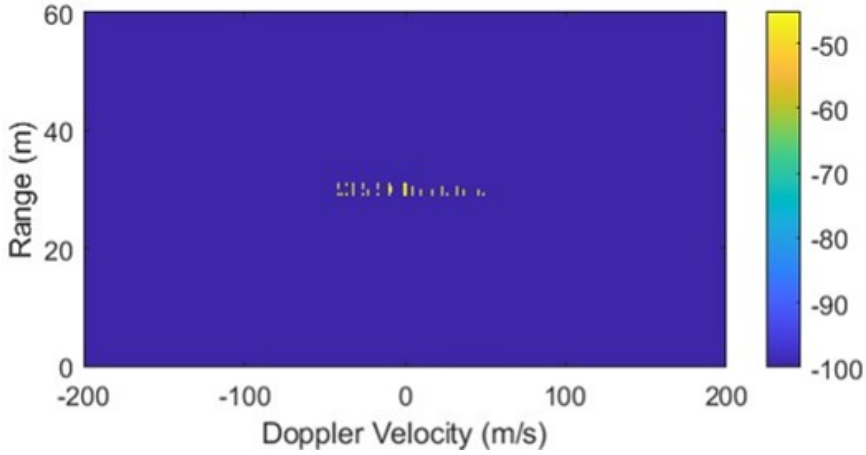
Furthermore, it's important to understand that common commercial UAVs may be used for malicious purposes such as transporting explosives for possible terrorist strikes. Studies like [75, 76] provide examples of previous research with UAVs carrying payloads that were conducted using real-measurement campaigns. The realization of comparable goals with much shorter deadlines and more economic viability is made possible by our proposed method, which offers noticeable advantages in terms of efficiency and cost-effectiveness. Figure 3.15a,b show the DJI Phantom 3 standard UAV with a rocket attached and dynamite attached, respectively, illustrating the potential threats associated with such modifications. The UAV, the rocket, and the dynamite models were imported from GrabCAD library [132, 133, 134]. The proposed method makes it possible to generate datasets concerning common UAVs that are carrying explosives. These datasets may then be used to train ML algorithms on a variety of scenarios, giving them the ability to efficiently detect and counteract such radar system deceptions. The ML algorithms can improve their capacity to effectively identify and classify UAVs even in the presence of deceptive tactics involving explosives.

For example, Figure 3.16 shows the classification accuracy of the CNN algorithm in classifying the DJI Phantom 3 standard, the DJI Phantom 3 standard with a rocket attached, and the DJI Phantom 3 standard with dynamite attached. Figure 3.16 demonstrates how the ML algorithm is unable to determine whether or not a typical UAV is carrying explosives. This mismatch results from the classifier's reliance on range-Doppler signatures, which were unable to distinguish the three UAVs because explosives do not provide extra Doppler information, as shown in Figure 3.17a–c. This suggests that a classifier may mistakenly identify an advancing UAV as a harmless DJI Phantom 3 standard without realizing the potential threat of it carrying explosives if it has just been taught to discriminate between different types of UAVs, as demonstrated in Figure 3.9b.

The proposed method provides the capacity to investigate and evaluate a variety of



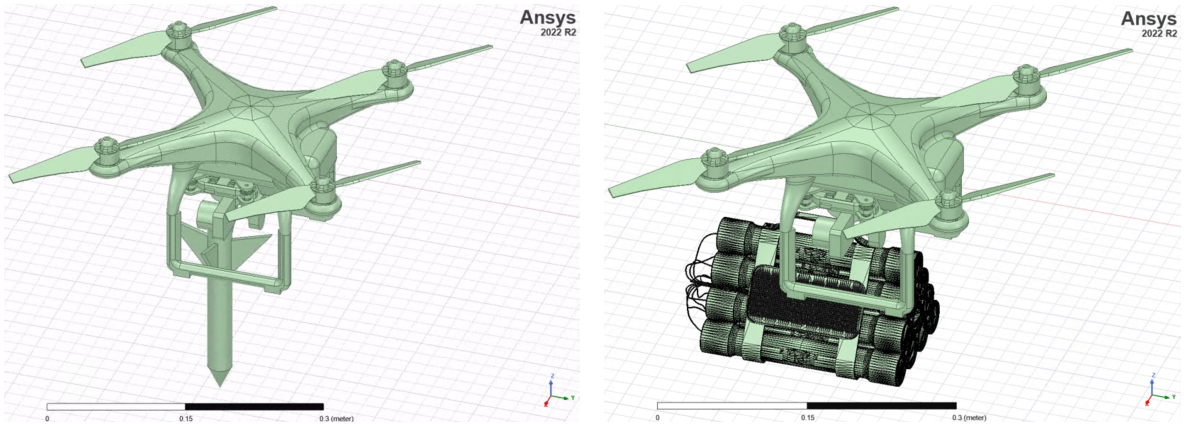
(a)



(b)

Figure 3.14: The effect of changing a UAV's material/coating (a) PEC material. (b) Plastic material.

scenarios, allowing to manage and reduce related risks. In particular, datasets that contain ISAR images capturing these dangerous situations can be used to train ML algorithms. With the use of the ISAR approach, which creates high-resolution images of a target based on its radar echoes, it is possible to examine the precise shape, structure, and motion of moving targets [135, 136, 137, 138, 139]. By making use of the relative motion between the radar platform and the target, ISAR operates. The radar system gathers several radar echoes emitted by the target as it travels. By processing these echoes, ISAR generates a two-dimensional image that reveals the target's spatial reflectivity distribution [135, 136,



(a) (b)

Figure 3.15: HFSS models depicting the DJI Phantom 3 standard UAV with explosives attached. (a) Rocket. (b) Dynamite.

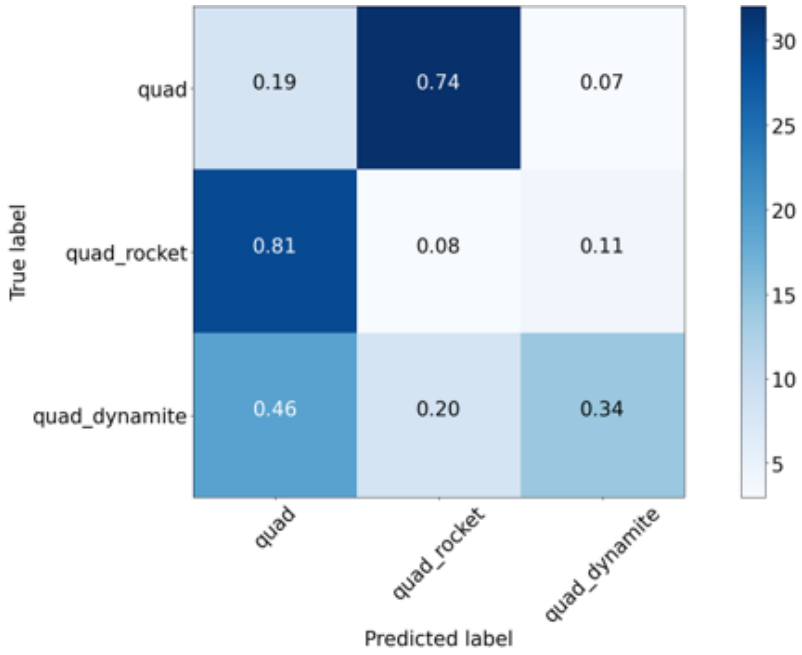


Figure 3.16: Accuracy of the CNN algorithm to detect if a standard UAV is carrying explosives using range-Doppler information.

137, 138, 139]. The proposed method is used to generate the ISAR images shown in Figure 3.18a–b. A bandwidth of 3.46 GHz, centered at 77 GHz, is used to assist the

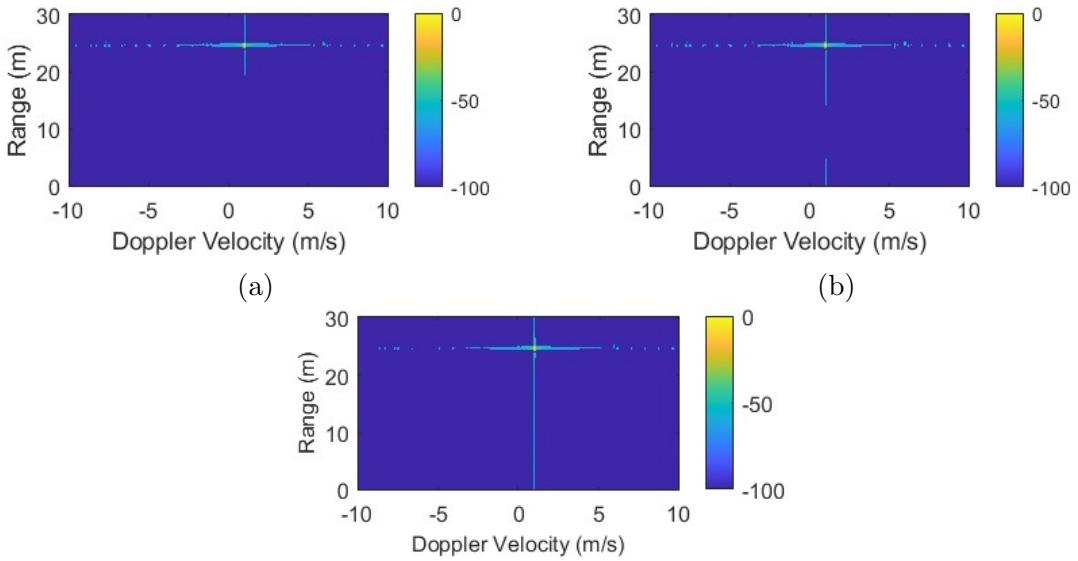


Figure 3.17: Range-Doppler maps for the DJI Phantom 3 standard UAV when: (a) Nothing attached. (b) Rocket attached. (c) Dynamite attached.

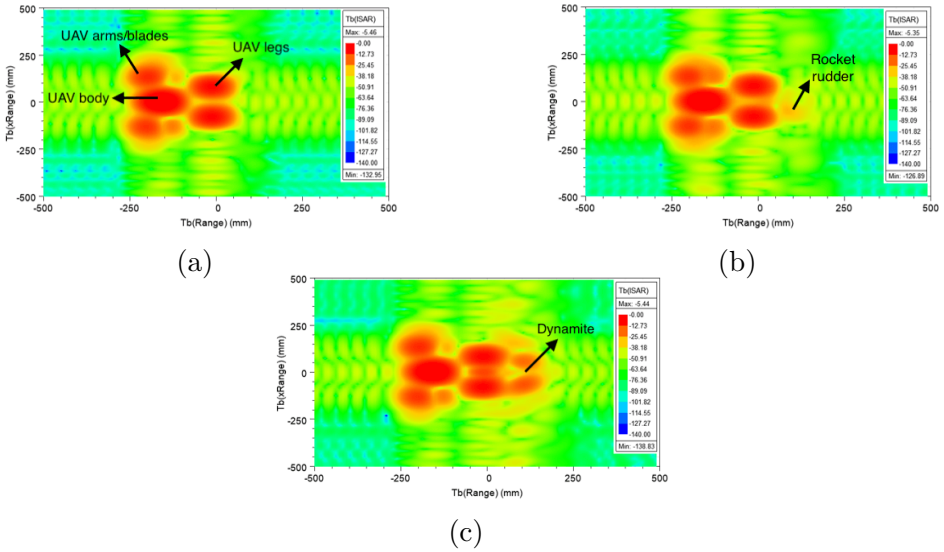


Figure 3.18: ISAR images for the DJI Phantom 3 standard UAV when: (a) Nothing attached. (b) Rocket attached. (c) Dynamite attached.

generation of the ISAR images. The range and The cross range resolutions are both set to 0.0433 GHz. As shown in Figure 3.19, the CNN algorithm displays outstanding accuracy

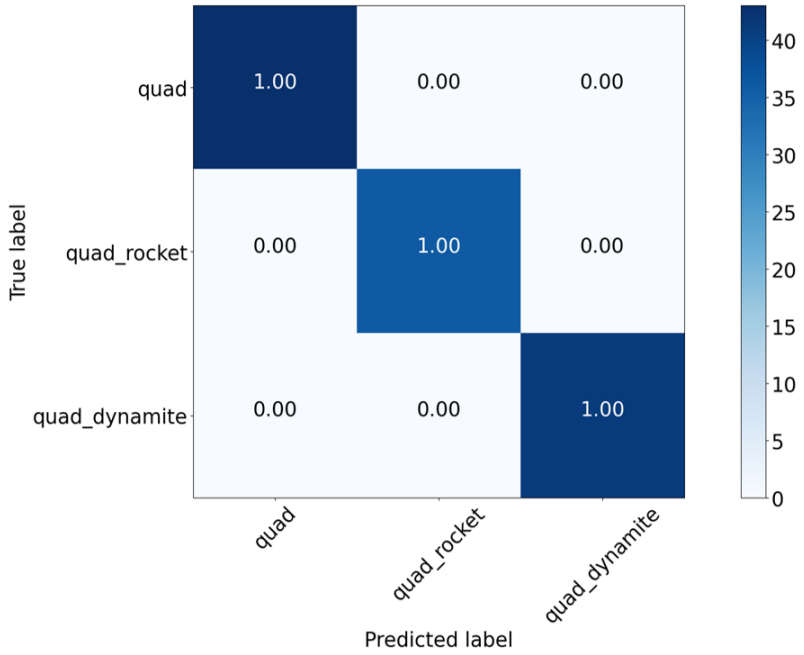
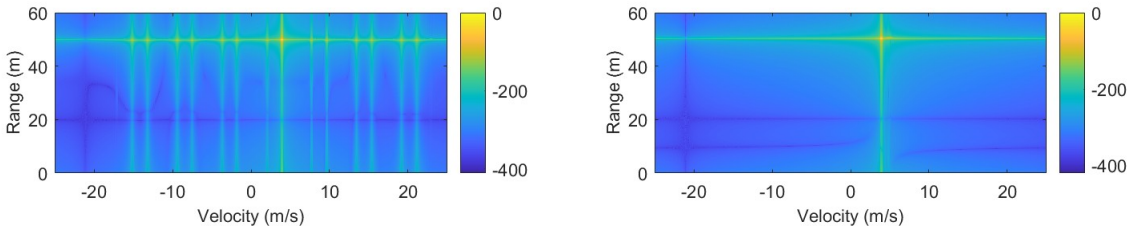


Figure 3.19: Accuracy of the CNN algorithm to detect if a standard UAV is carrying explosives using ISAR images.

in determining whether or not a UAV is carrying explosives. To achieve this, an additional set of classification layers can be employed to determine if a specific UAV is carrying payloads after its initial classification by the first set of classification layers.

Moreover, a comprehensive investigation is conducted to evaluate the ML algorithms' capacities to identify and classify UAVs in the presence of avian entities. The study involves the use of two different ML models, namely a CNN classifier and a SVM classifier [140]. Using a W-band radar with a bandwidth of 4 GHz, the proposed method is utilized to



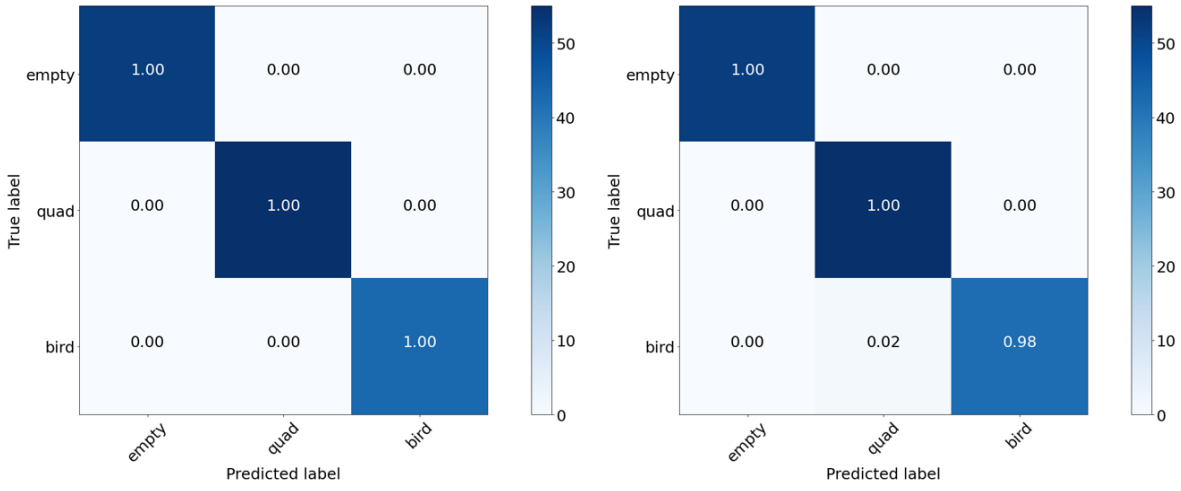
(a) (b)

Figure 3.20: Range-Doppler maps for: (a) The quadcopter UAV. (b) The bird.

facilitate the modeling of the DJI Phantom 4 Pro V2.0 quadcopter [117], and the American Eagle bird. Using the proposed method, datasets containing the range-Doppler maps for both the quadcopter and the avian subject are generated. The ML models are trained on a dataset generated using a basic simulation framework, in which the UAV or the bird moves independently at a speed of 4 m/s and pitches to the radar along a linear track as shown in Figure 3.6. For both the UAV and the bird, a set of 250 range-Doppler maps is generated, alongside an equivalent number for an unoccupied scene. For example, the range-Doppler maps for the quadcopter UAV and the bird are presented in Figure 3.20a,b, respectively. The subsequent classification result demonstrates a noteworthy degree of accuracy, as shown in Figure 3.21a,b.

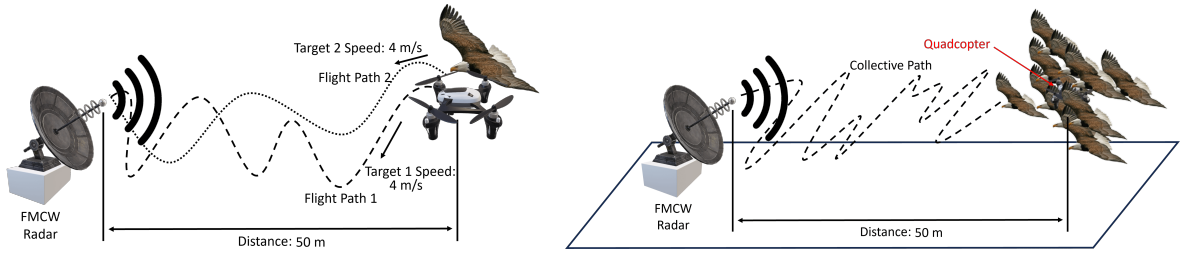
The trained ML models are then applied to three different datasets, each of which represents a different situation where a UAV and avian entities coexist in the same environment. The goal of this investigation is to carefully consider the ramifications of detecting and correctly classifying a UAV in the midst of an environment with avian subjects. The scenarios subjected to testing are outlined as follows:

1. Single quadcopter alongside a solitary bird.
2. Single quadcopter accompanied by two birds.
3. Single quadcopter navigating amidst a swarm of ten birds.



(a) (b)

Figure 3.21: Confusion matrices of the trained ML models. (a) CNN. (b) SVM.



(a) (b)

Figure 3.22: Simulation setup for the quadcopter with: (a) One/two birds. (b) Swarm of 10 birds.

Table 3.6: Classification accuracy results of a UAV among avian subjects

Scenario	**CNN**	**SVM**
One Bird	99%	97%
Two Birds	98%	92.5%
Swarm of 10 Birds	90%	86.5%

In the instances involving one or two birds exclusively, both the quadcopter and the avian entities traverse comparable trajectories at equivalent speeds, following randomized curved paths, as depicted in Figure 3.22a. It is important to highlight that Figure 3.22a exclusively illustrates the simulation arrangement for the initial scenario, while the subsequent scenario introduces an additional bird navigating through an alternative randomized curved trajectory. Conversely, for the latter scenario characterized by a bird swarm, a representative depiction of this simulation setup is presented in Figure 3.22b. In the context of the bird swarm scenario, the birds execute coordinated flight trajectories parallel to that of the UAV, a maneuver strategically employed to confuse radar detection. This tactical evasion serves as an intentional measure to potentially exploit the UAVs for unauthorized purposes or illicit activities, such as terrorist operations.

The observable outcomes are documented in Table 3.6, wherein the classification accuracy of both the CNN and SVM models in the context of UAV detection and classification amidst avian entities is cataloged. As shown in Table 3.6, it is evident that the likelihood of detecting and precisely classifying a UAV diminishes as the number of concurrent avian subjects escalates.

Due to its independence from the complexity and time restrictions imposed by field measurements, the proposed method provides an efficient way to examine attempts taken to deceive radar systems. The proposed method can model radar system behavior and

predict how it will react to various UAV designs and flight paths. The proposed method provides several advantages over field observations, including the speed with which they can evaluate many scenarios with various parameters. As an illustration, the examination duration for the scenario involving the attachment of explosives, utilizing the proposed method, is 45 minutes, in contrast to around two days required for equivalent investigations using real-measurements. This enables researchers and engineers to assess the efficacy of various defenses against efforts to deceive radar systems quickly and adjust their designs accordingly. Additionally, the proposed method can be a useful tool for researchers to better understand the underlying physics of radar systems.

Chapter 4

Mechanical Control-Based Machine Learning for UAV Classification

4.1 Introduction

The Doppler signatures of Unmanned Air Vehicles (UAVs), which are widely used to classify different types of them, depend on their movement mechanism. Because of this, a Machine Learning (ML) algorithm's accuracy drops if the impact of the mechanical control information of UAVs is not taken into consideration, which may lead to a non-unique signature of a UAV while in-flight. In this chapter, the influence of the control systems of two quadcopters, a hexacopter, and a helicopter UAVs on their range-Doppler signatures is explored. UAVs have five "basic" motions which are hovering, pitching, throttling, rolling, and yawing. For a UAV to perform each motion, the speeds of the rotors of this UAV have to be changed which subsequently affects the UAV's Doppler signature. The Doppler signature of each movement of a UAV differs from the Doppler signature for the other movements. In the state-of-the-art literature, ML models are trained and tested on the same datasets that contain only hovering and pitching motions for a UAV, for example [141, 101, 97, 100, 98, 99, 63, 96, 25, 76, 75, 103]. This leads to a degradation on ML accuracy if these trained models are tested using different datasets that contain other motions of UAVs as the Doppler signatures of UAVs are highly dependent on the mechanical control information of them. To overcome this and in contrast to the state-of-the-art literature, a Mechanical Control-Based Machine Learning (MCML) method is proposed. Figure 4.1a,b shows the traditional method used to generate signatures for UAVs in the state-of-the-art literature and the proposed MCML method, respectively.

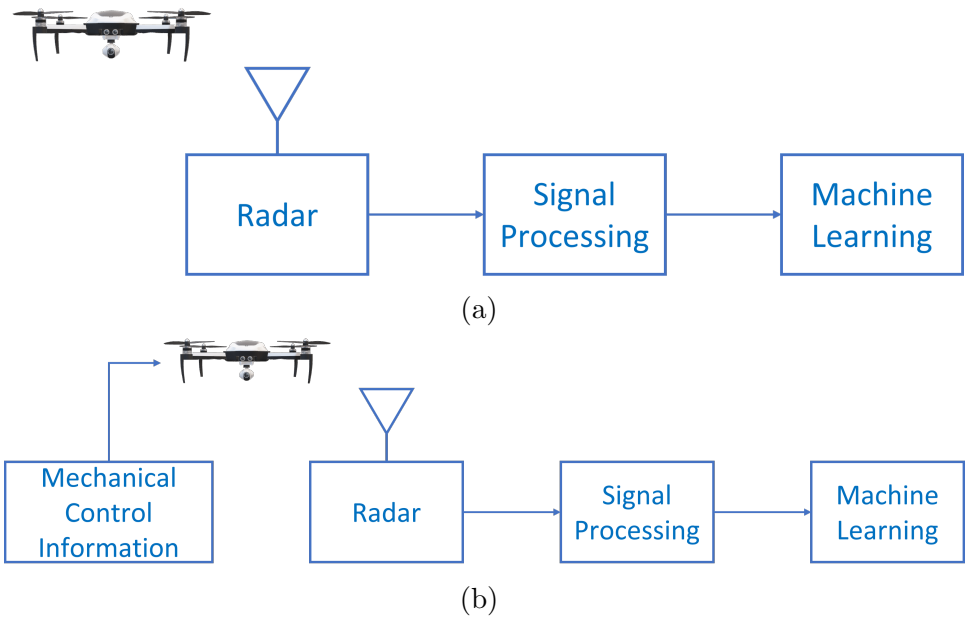


Figure 4.1: (a) Traditional Method. (b) Proposed MCML Method.

4.2 Mathematical Background

In order to better understand the impact of UAVs control systems on their Doppler signatures, the mathematical model of the equations of motions for a quadcopter and a hexacopter UAVs in different movements is described in this section. The equations of motions for the helicopter UAV are presented in [142].

4.2.1 Quadcopter Equations of Motions

By adjusting the rotors' angular velocities, a quadcopter UAV is controlled. A quadcopter UAV is considered a 4-rotor helicopter in essence. Its thrust to hover or throttle is provided by the four rotors equally, while other movements are controlled by changing the motors' speeds. In order to ensure stability and all necessary motions, a quadcopter's four rotors are positioned in both a Clockwise (CW) and a Counterclockwise (CCW) direction. In addition, to hover in the air, quadcopters throttle, pitch, roll, and yaw in both directions. The body frame of a quadcopter is shown in Figure 4.2 [4]. The forces and moments on a quadcopter are given as [4, 143]:

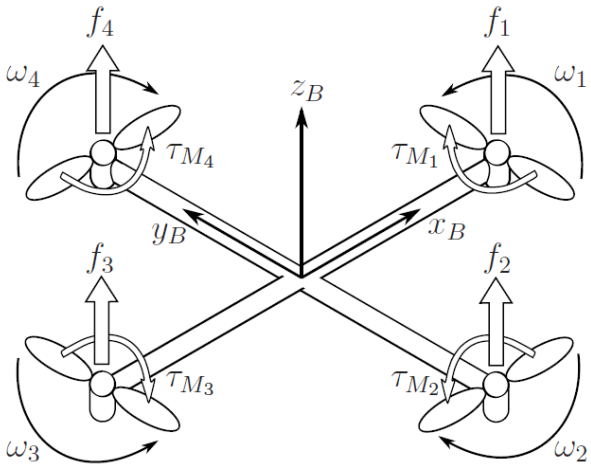


Figure 4.2: The quadcopter frame body [4].

$$F_i = K_f \times \omega_i^2 \tag{4.1}$$

$$M_i = K_m \times \omega_i^2 \tag{4.2}$$

where F_i is the lifting force for each propeller, M_i is the moment at each propeller, $i = 1, 2, 3, 4$, K_f and K_m are the aerodynamics force and moment constants, and w_i is the angular speed for each propeller.

The resultant thrust by opposite propellers generates moments in x and y axes, M_x and M_y:

$$M_y = (F_2 - F_4) \times L \tag{4.3}$$

$$M_x = (F_1 - F_3) \times L \tag{4.4}$$

where L is the length between the two propellers. According to Newton's second law of motion, the linear and rotational motions of a quadcopter can be expressed as [143]:

$$Force = mass \times linear\ acceleration \tag{4.5}$$

$$Torque = inertia \times angular\ acceleration \tag{4.6}$$

Since inertia is the object's resistance to change, while in motion, as the momentum increases, the inertia increases. The linear motion of a quadcopter is represented in (4.5), while (4.6) represents the rotational motion.

When a quadcopter hovers, all the forces applied to it must be in balance, which means the total lifting force equals its weight, mg, which is the gravity force that acts in the opposite direction of the thrust. Additionally, the conservation of momentum gives:

$$mg = F_1 + F_2 + F_3 + F_4 \tag{4.7}$$

The equation of motion for a hovering quadcopter is:

$$m\frac{\partial^2 r}{\partial t^2} = F_1 + F_2 + F_3 + F_4 - mg = 0 \tag{4.8}$$

where m is the mass of the quadcopter, and r is the position. For a quadcopter to throttle up and throttle down, its equations of motion are given as:

$$m\frac{\partial^2 r}{\partial t^2} = \begin{cases} F_1 + F_2 + F_3 + F_4 - mg > 0 & F > mg \\ F_1 + F_2 + F_3 + F_4 - mg < 0 & F < mg \end{cases} \tag{4.9}$$

where the total lifting force F=F_1+F_2+F_3+F_4, in addition, $all\ moments = 0$. On the other hand, in yaw motions, $all\ moments \neq 0$, while $F = mg$, then:

$$m\frac{\partial^2 r}{\partial t^2} = F_1 + F_2 + F_3 + F_4 - mg = 0 \tag{4.10}$$

$$I_{ZZ}\frac{\partial^2 \Psi}{\partial t^2} = M_1 + M_2 + M_3 + M_4 \tag{4.11}$$

where the yaw, Ψ, pitch, Θ, and roll, Φ, are called the Euler angles [143]. These angles describe the angular orientation of a fixed body with respect to a reference frame. Due to the quadcopter symmetrical frame, the inertia matrix $\boldsymbol{I}$ is given as:

$$\boldsymbol{I} = \begin{bmatrix} I_{XX} & 0 & 0 \\ 0 & I_{YY} & 0 \\ 0 & 0 & I_{ZZ} \end{bmatrix} \tag{4.12}$$

Finally, in pitch and roll motions, $all\ moments \neq 0$, and $mg < F$. The pitch and roll angles must be nonzero; this causes nonzero components of thrust in the horizontal direction, which causes a resultant moment in the horizontal plane. The equations of motion become:

$$m\frac{\partial^2 r}{\partial t^2} = F_1 + F_2 + F_3 + F_4 - mg > 0 \tag{4.13}$$

$$I_{XX}\frac{\partial^2 \Phi}{\partial t^2} = (F_1 - F_3) \times L \tag{4.14}$$

$$I_{YY}\frac{\partial^2 \Theta}{\partial t^2} = (F_2 - F_4) \times L \tag{4.15}$$

4.2.2 Hexacopter Equations of Motions

Similar to the quadcopter UAV, the hexacopter UAV is controlled by changing the angular velocities of the rotors; however, it provides more flight time and has the ability to carry more load. A hexacopter UAV is considered a 6-rotor helicopter, its thrust is provided by the six rotors equally in order for a hexacopter UAV to hover, while other movements can be controlled by changing the motors' speeds. The rotors of a hexacopter are arranged CW and CCW that work together to provide stability and all required movements for a hexacopter [144]. The body frame of a hexacopter is shown in Figure 4.3 [5]. According to [144, 5, 143], the forces and moments on a hexacopter follow equations (4.1) and (4.2).

The equation of motion for a hovering hexacopter is given as:

$$m\frac{\partial^2 r}{\partial t^2} = F_1 + F_2 + F_3 + F_4 + F_5 + F_6 - mg = 0 \tag{4.16}$$

For a hexacopter to throttle up and down, its equations of motion are given as:

$$m\frac{\partial^2 r}{\partial t^2} = \begin{cases} F - mg > 0 & F > mg \\ F - mg < 0 & F < mg \end{cases} \tag{4.17}$$

where the total lifting force$F$=F_1+F_2+F_3+F_4+F_5+F_6, $all\ moments = 0$. In yaw motions, $all\ moments \neq 0$, while $F = mg$, and the total torque in the z-axis can be obtained

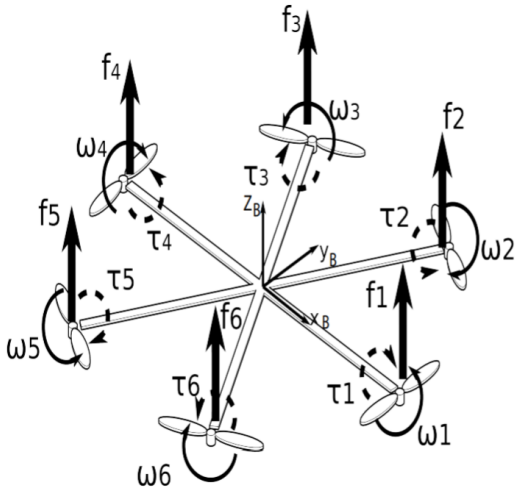


Figure 4.3: The hexacopter frame body [5].

by increasing/decreasing the CW rotors speeds while decreasing/increasing the CCW rotors speed. The equation of motion for the yaw motion is given as:

$$m\frac{\partial^2 r}{\partial t^2} = F_1 + F_2 + F_3 + F_4 + F_5 + F_6 - mg = 0 \tag{4.18}$$

Finally, in pitch and roll motions, *all moments* $\neq 0$, and $mg < F$. The pitch and roll angles must be nonzero; this causes nonzero components of thrust in the horizontal direction, which causes the resultant moment to be in the horizontal plane. The pitch motion is achieved by increasing/decreasing the rear rotors' speeds while decreasing/increasing the front rotors' speeds. Roll motion is achieved by increasing/decreasing the side rotors' speeds while decreasing/increasing the other side rotors' speeds. The equation of motion becomes:

$$m\frac{\partial^2 r}{\partial t^2} = F_1 + F_2 + F_3 + F_4 + F_5 + F_6 - mg > 0 \tag{4.19}$$

The torques applied on the hexacopter body around the roll, pitch, and yaw angles given by

$$\tau_\Phi = \frac{3}{4} K_f r \ ({\omega_2}^2 + {\omega_3}^2 - {\omega_5}^2 - {\omega_6}^2) \tag{4.20}$$

$$\tau_\Theta = K_f r \ (-{\omega_1}^2 - \frac{{\omega_2}^2}{4} + \frac{{\omega_3}^2}{4} + {\omega_4}^2 + \frac{{\omega_5}^2}{4} - \frac{{\omega_6}^2}{4}) \tag{4.21}$$

$$\tau_\Psi = b \ (-{\omega_1}^2 + {\omega_2}^2 - {\omega_3}^2 + {\omega_4}^2 - {\omega_5}^2 + {\omega_6}^2) \tag{4.22}$$

where b is a constant.

As shown in (4.1) and (4.2), by mechanically controlling the speeds of the UAVs' rotors, the behavior or movement for the quadcopter and the hexacopter UAVs changes, which also affects the range-Doppler signatures for these UAVs.

4.3 Simulation Setups

The MD4-1000 quadcopter UAV, the DJI FPV quadcopter UAV, the Black Eagle 50 helicopter UAV, and the DJI S900 hexacopter UAV are the four different UAVs that are used in this investigation. Figure 4.4a–d displays the simulation setups for the four UAVs various motions. While Table 4.1 shows the radar parameters that are used in this work.

When a UAV throttles up, the rotors should have the same speed, which is calculated to be high enough to produce a thrust greater than the weight of the UAV. While when

a UAV throttles down, the rotors' speeds are calculated to be lower enough to produce a thrust less than the weight of the UAV, as illustrated in Figure 4.4a. On the other hand, the back rotors of a UAV must rotate at a faster rate than the front rotors in order to pitch it forward, and the opposite is true to pitch it backward, as shown in Figure 4.4b. As shown in Figure 4.4c, a UAV rolls left by having the right rotors rotate faster than the left rotors, and vice versa for a right roll. To keep the UAV stable, each rotor turns in a distinct direction from the one next to it. According to Figure 4.4d, a UAV yaws left by having the CCW rotors rotate faster than the CW rotors, and it yaws right by increasing the rotation rate for the CW rotors than that for the CCW rotors. For example, Figure 4.5 summarizes the different motions with the rotors speeds for a quadcopter [6]. For example, the impact of the mechanical control information of the MD4-1000 quadcopter UAV and the DJI S900 hexacopter UAV on their range-Doppler images are shown in Figure 4.6a–f, Figure 4.7a–f,

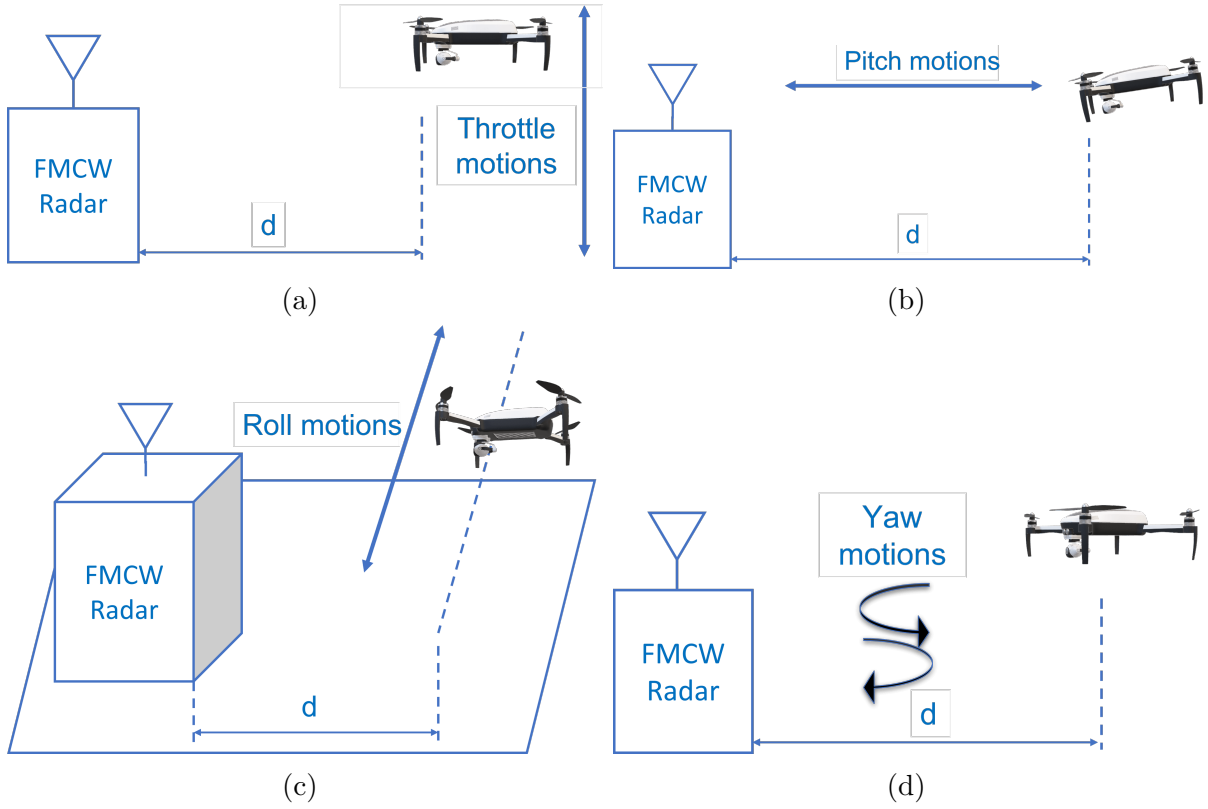


Figure 4.4: Simulation setups for the UAVs' different movements. (a) Throttle. (b) Pitch. (c) Roll. (d) Yaw.

Table 4.1: Specified radar parameters.

Quantity	Symbol	Value
Center Frequency	f_0	77 GHz
Bandwidth	BW	2 GHz
Range Resolution	ΔR	0.075 m
Velocity Resolution	ΔV	0.52 m/s
Maximum Range	R_{max}	60 m
Antenna Beam Width	$HPBW$	60°
Antenna Polarization	V	Vertical

and Figure 4.8a–d. The proposed method in Chapter 3 is used to generate the required datasets for this investigation. These datasets contain the range-Doppler information of the four UAVs according to the simulation setups shown in Figure 4.4a–d.

Four different datasets are used in this investigation, and all of them contain the range-Doppler information of the four UAVs. The first dataset contains 1200 range-Doppler images, with 300 images for each UAV, and represents pitch and throttle motions, as shown in Figure 4.4a,b. The second dataset contains 1600 range-Doppler images, with 400 images for each UAV, and represents roll and yaw motions, as shown in Figure 4.4c,d. The third dataset contains all types of motions for each UAV with different speeds and

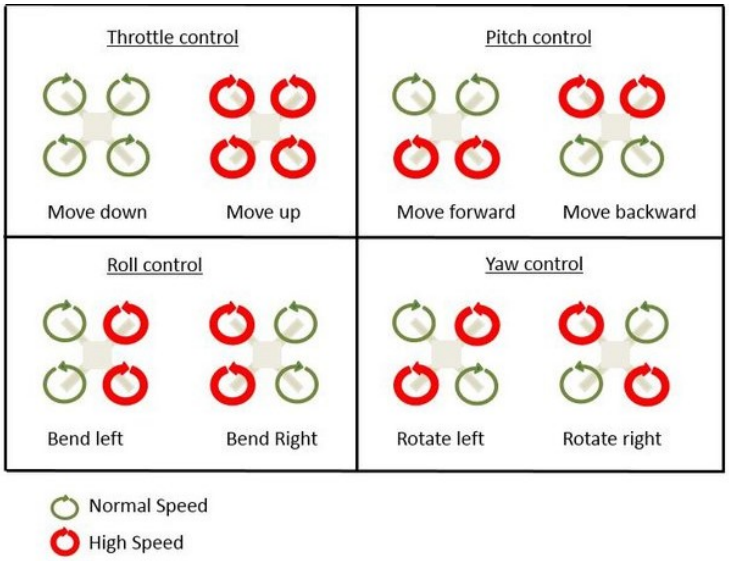


Figure 4.5: Quadcopter control [6].

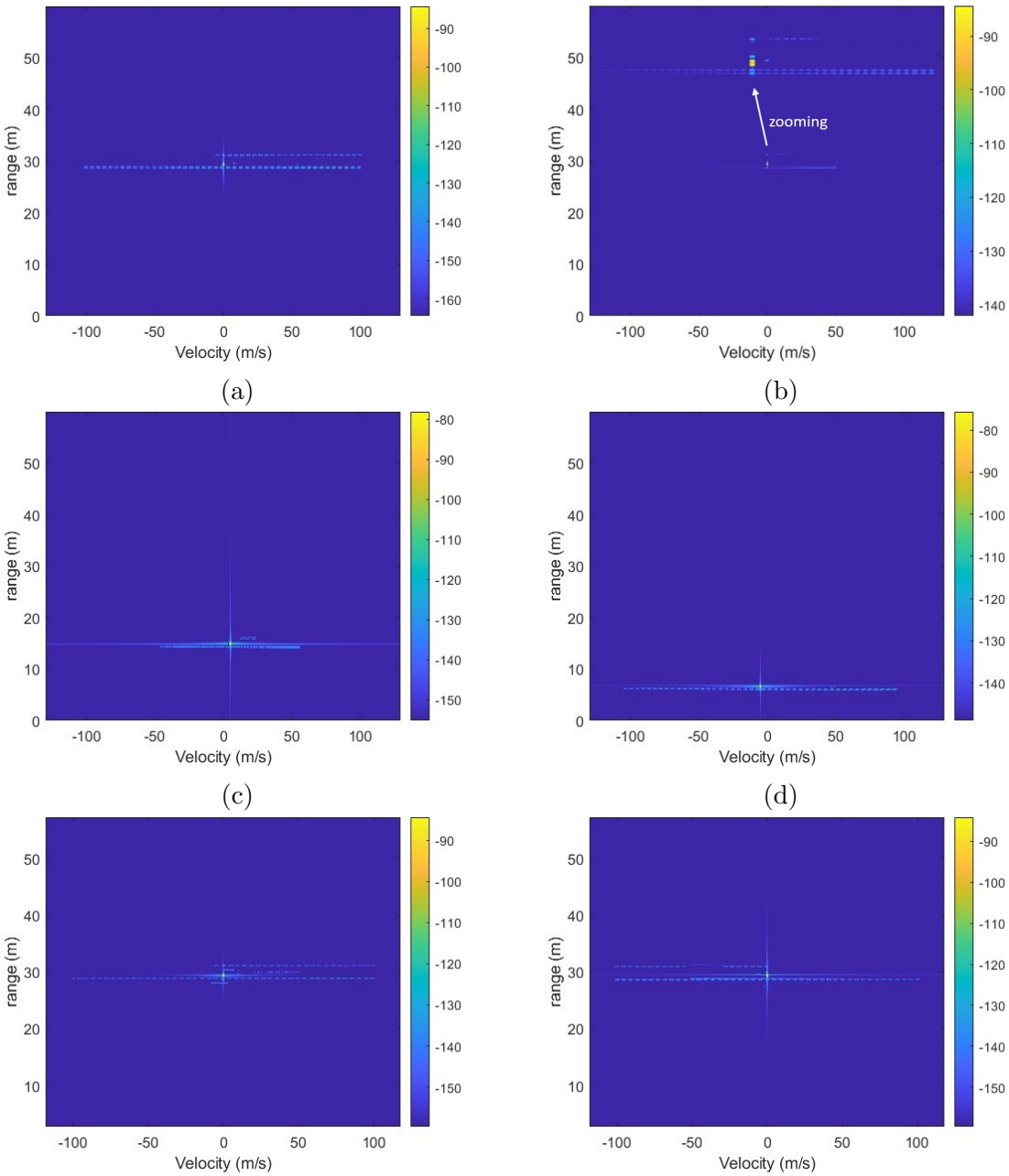


Figure 4.6: Range-Doppler maps for a quadcopter when: (a) Throttle up. (b) Throttle down. (c) Pitch forward. (d) Pitch backward. (e) Roll left. (f) Roll right.

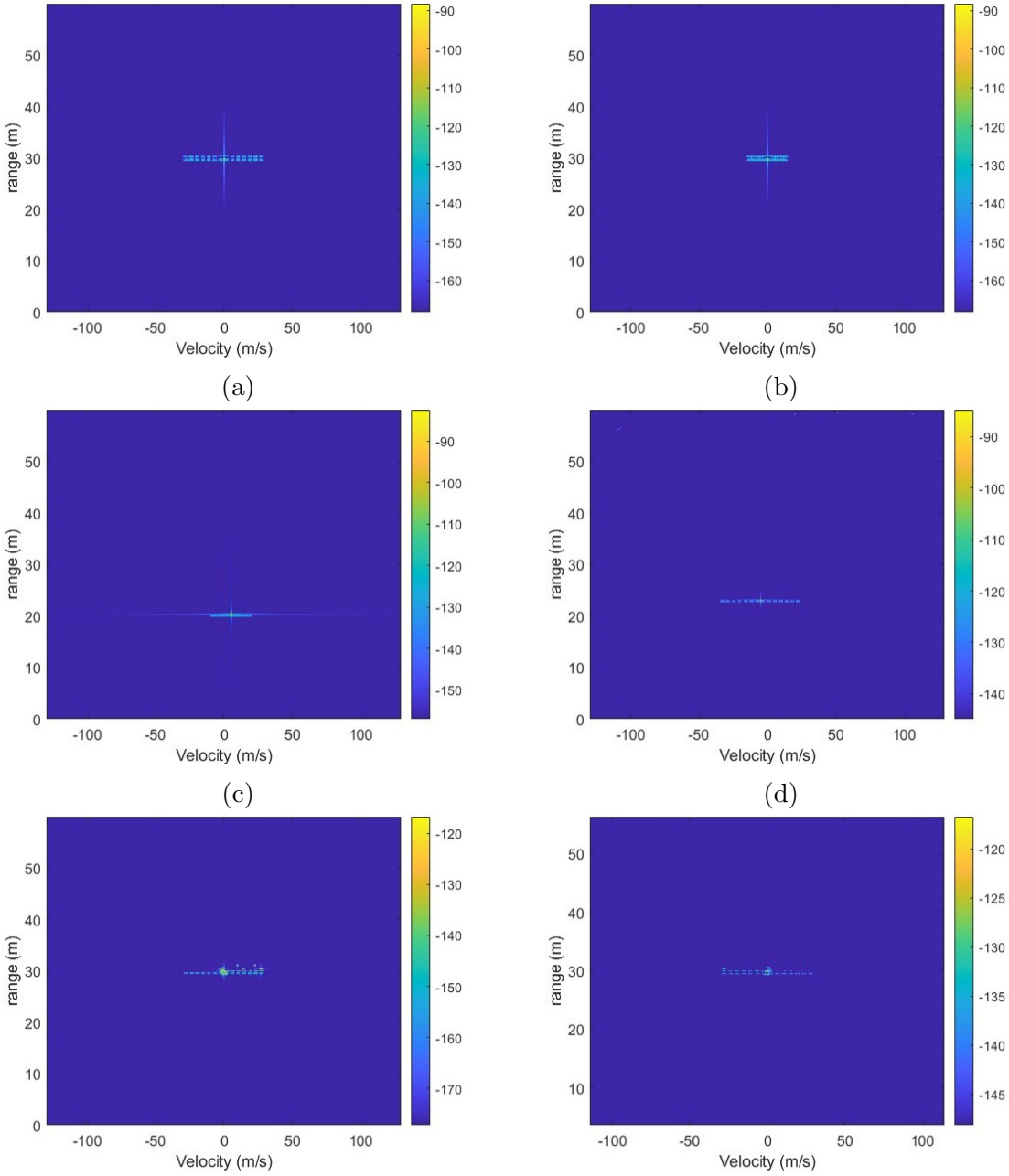


Figure 4.7: Range-Doppler maps for a hexacopter when: (a) Throttle up. (b) Throttle down. (c) Pitch forward. (d) Pitch backward. (e) Roll left. (f) Roll right.

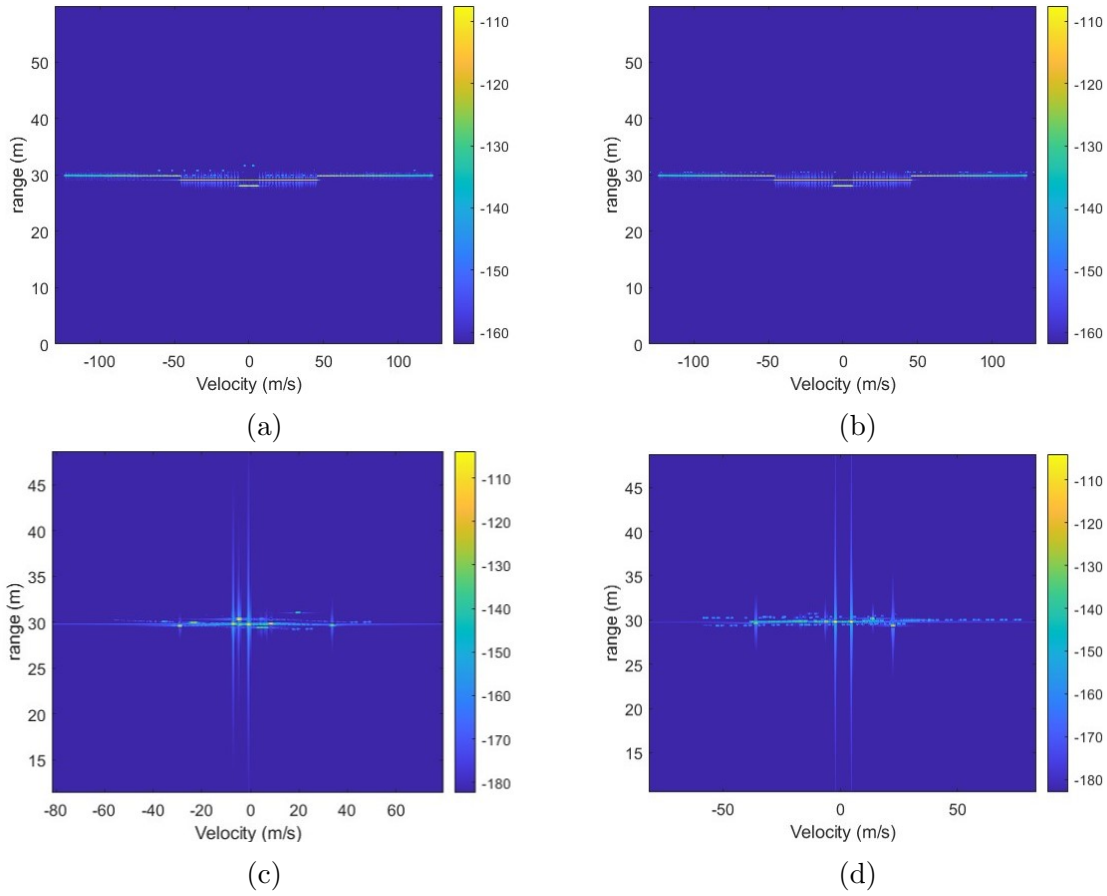


Figure 4.8: Range-Doppler maps for: (a) Yaw left quadcopter. (b) Yaw right quadcopter. (c) Yaw left hexacopter. (d) Yaw right hexacopter.

contains 2800 range-Doppler images, with 700 images for each UAV. The fourth dataset is used to validate the proposed MCML approach. It includes range-Doppler images of the four UAVs with randomized motions and different speeds. The number of range-Doppler images in each dataset depends on the number of modeled motions and the number of range-Doppler images for each motion. The datasets are divided into 80% training set and 20% test set. Table 4.2 presents a summary of the types of motions in the four datasets utilized in this investigation, along with the number of frames contained in each dataset.

Table 4.2: Generated datasets.

Dataset	Control Motions	range-Doppler images
Dataset 1	Throttle and Pitch	1200 (300/UAV)
Dataset 2	Roll and Yaw	1600 (400/UAV)
Dataset 3	Throttle, Pitch, Roll, and Yaw	2800 (700/UAV)
Dataset 4	Random *all* motions	3000 (750/UAV)

4.4 Classification Results

Eight different ML algorithms are applied to the dataset generated according to Figure 4.4a–d to investigate and compare their performance on classifying the four UAVs. The MD4-1000 quadcopter UAV, the DJI FPV quadcopter UAV, the DJI S900 hexacopter UAV, and the Black Eagle 50 helicopter UAV are denoted as Quad A, Quad B, Hexa, and Heli, respectively. The eight classifiers are 3 different Convolutional Neural Network (CNN) algorithms, Support Vector Machine (SVM), K-nearest Neighbors (KNN), Naive Bayes (NB), Random Forest (RF), and Decision Tree (DT) classifiers. When the mechanical control information of UAVs is not taken into consideration, the classification accuracy for the eight ML algorithms decreases; however, when this information is taken into consideration, the eight ML algorithms perform well, as shown in Figure 4.9, which illustrates

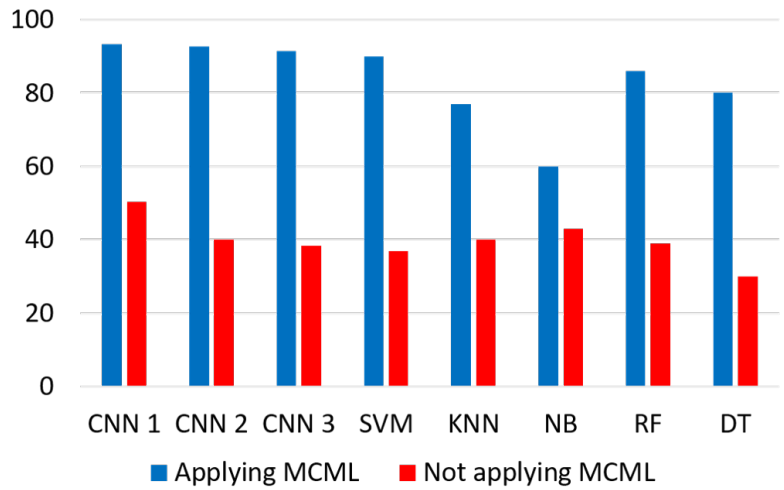


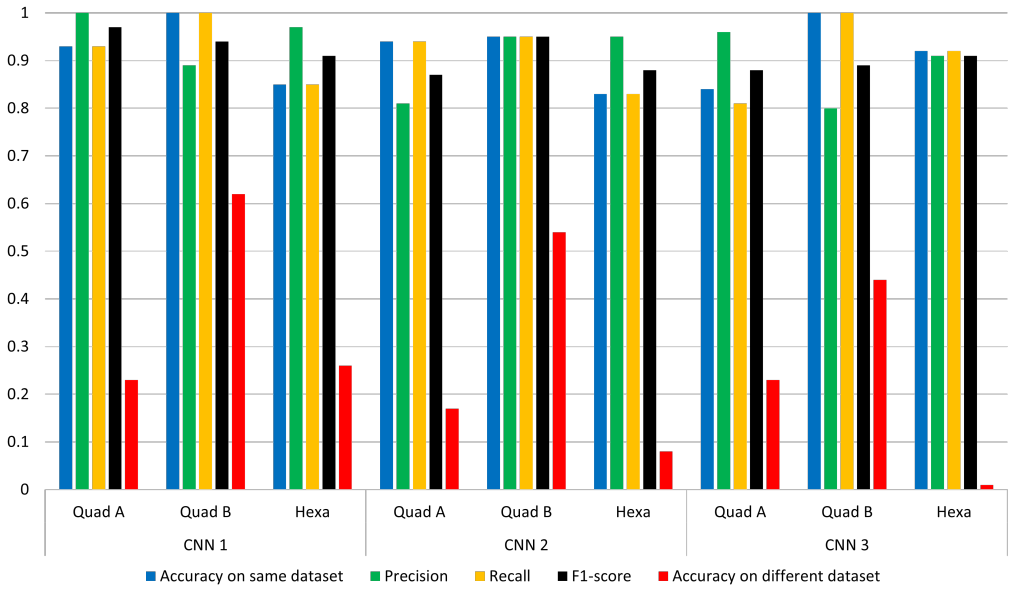
Figure 4.9: Different classifiers accuracy when considering/Not considering the mechanical control information of UAVs.

the accuracy of the eight ML algorithms. The DopplerNet algorithm [23], CNN1, the VGG16 algorithm [145], CNN2, and the light CNN algorithm [141], CNN3, are the three most accurate algorithms, respectively. Figure 4.10a,b show the classification reports for the three CNN classifiers when the mechanical control information of UAVs is not taken into consideration and when it is considered, respectively, for a more investigation.

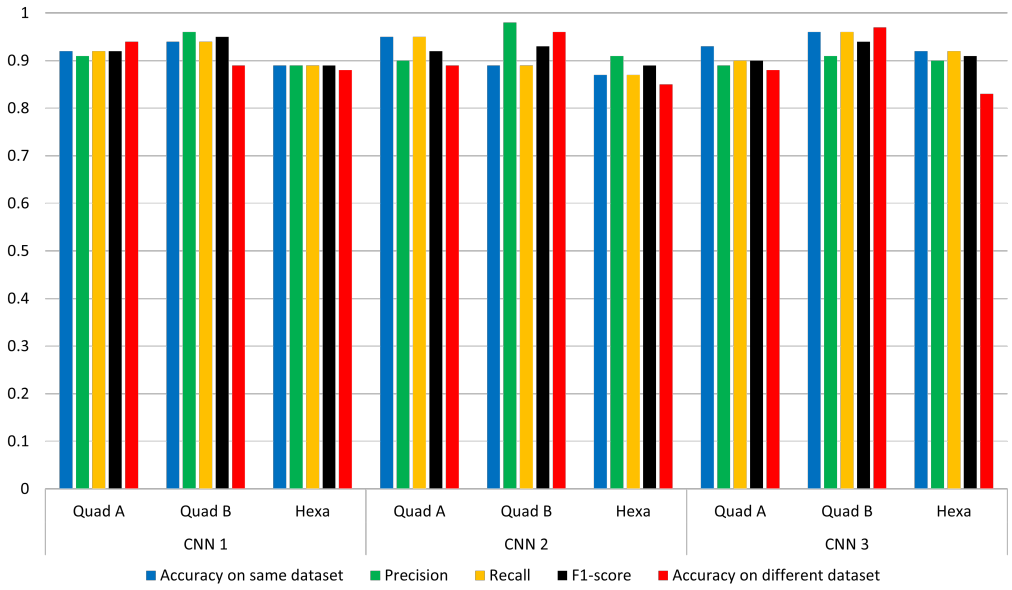
The helicopter UAV is easily distinguished since it has a higher RCS area than the other UAVs, hence the classification reports for the CNN classifiers only include the quadcopters and the hexacopter UAVs. The three most accurate CNN algorithms are adjusted to meet the range-Doppler images dimensions. It is discovered that the DopplerNet algorithm has a slightly higher accuracy than the other two CNN algorithms. It is therefore employed to classify the four UAVs. This model has become less complex with the addition of a Maxpooling layer in order to prevent over-fitting. Figure 4.11a depicts the algorithm's flow chart, which is made up of eight layers. The input layer's dimensions are $800 \times 500 \times 1$ based on the range and velocity resolutions that are selected, which are displayed in Table 4.1. A convolutional layer with 32 filters, a 3×3 kernel, and a Rectified Linear Unit (ReLU) activation function produces an output with a $798 \times 498 \times 32$. Following the convolutional layer comes a Maxpooling, 2×2, layer with an output size of $399 \times 249 \times 32$. The previous feature map is flattened into a vector with an output size of $3,179,232$. In addition to more four dense layers, three of which employ a ReLU activation function with an output size of 64 and the output layer, which employs a Softmax activation function to calculate the probability of each of the four classes. The hyperparameters of the algorithm are 10 epochs, 10 batches and Adam optimizer [130]. The DopplerNet algorithm is trained on dataset 1, from Table 4.2, and the results are displayed in Figure 4.11b with an accuracy of more than 90%.

According to Figure 4.12a, when the trained CNN algorithm is evaluated on dataset 2, from Table 4.2, its accuracy falls to 50.25%. This is the case of all earlier studies where ML models are trained and tested on a dataset that lacks relevant mechanical control data, for instance [141, 101, 97, 100, 98, 99, 63, 96, 25, 76, 75, 103]. However, if the classifier is trained on a dataset that included *all* basic possible mechanical control information, as shown in Figure 4.1b, its accuracy would remain higher than 90%, as shown in Figure 4.12b. In this instance, the classifier is trained on a combined dataset of datasets 1 and dataset 2, and it is tested on dataset 3, from Table 4.2.

For additional validation, a completely different dataset is generated. The new dataset, dataset 4 (from Table 4.2), contains random motions of the four UAVs at different rotors' speeds. The trained MCML algorithm that covers all the basic mechanical control information of UAVs is applied to this new scenario, yielding an accuracy of at least 90%, as shown in Figure 4.13. In the state-of-the-art literature, ML algorithms are trained on

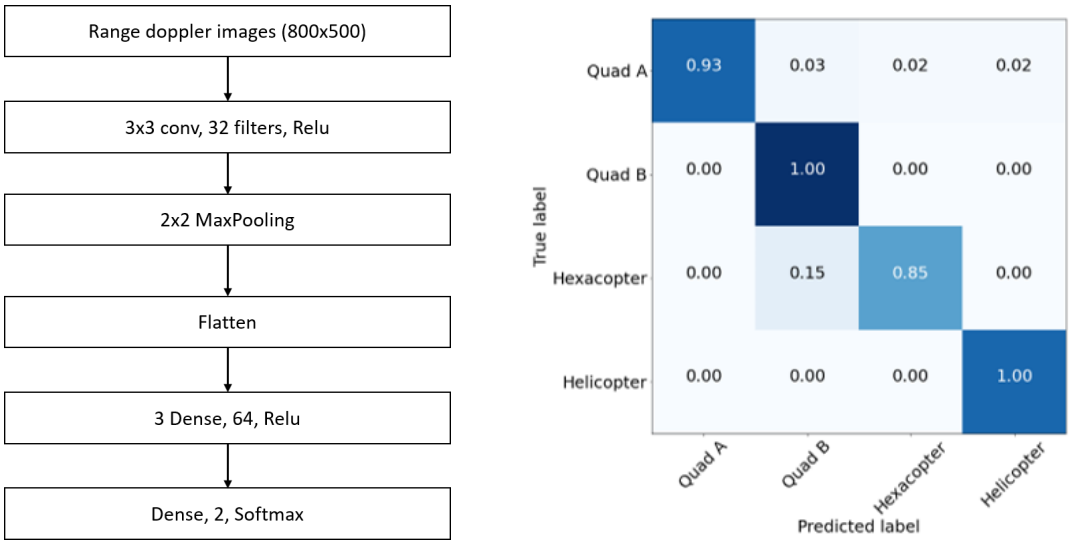


(a)



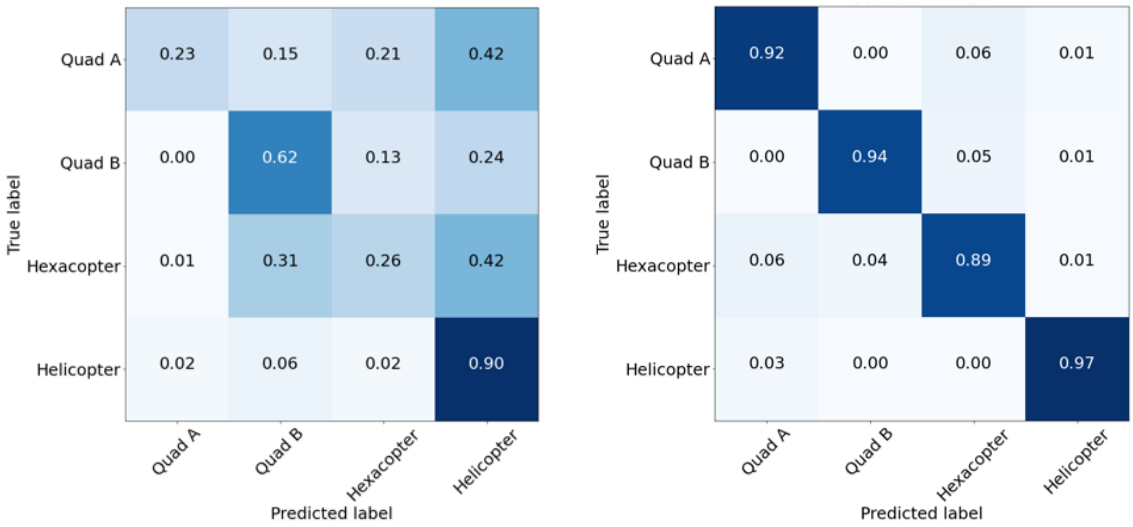
(b)

Figure 4.10: Comparison of the classification reports for the three different CNN algorithms used in this work when: (a) Not considering the mechanical control information of UAVs. (b) Considering the mechanical control information of UAVs.



(a) (b)

Figure 4.11: (a) A flowchart of the DopplerNet CNN algorithm. (b) Its confusion matrix when it is applied to the same dataset.



(a) (b)

Figure 4.12: Confusion matrix for the DopplerNet CNN algorithm when (a) Not considering the mechanical control information of UAVs. (b) Considering the mechanical control information of UAVs.

the hovering motion only of the UAVs, and few times they are trained on the hovering and pitching motions as reported in [141, 101, 97, 100, 98, 99, 63, 96, 25, 76, 75, 103]. A new scenario that contains random motions of the four UAVs is modeled to create a dataset that contains range-Doppler images of the random motions for the four UAVs as shown in Figure 4.14. The DopplerNet CNN classifier is trained solely on the hovering and pitching motions, following the approach employed in the current state-of-the-art literature [141, 101, 97, 100, 98, 99, 63, 96, 25, 76, 75, 103]. Then, the trained DopplerNet CNN classifier is applied to the generated dataset according to the scenario shown in Figure 4.14, yielding an accuracy around 60%, as shown in Figure 4.15a. Finally, the MCML algorithm, which considers *all* basic mechanical control information of UAVs, is applied to the same dataset giving an accuracy exceeding 97%, as shown in Figure 4.15b.

Using the AWR1443BOOST radar [2] from Texas Instruments (TI), the effect of the mechanical control information on the range-Doppler images of a quadcopter UAV is examined. As a proof of concept, the DJI Phantom 3 standard quadcopter UAV is utilized to generate range-Doppler images of throttling up and pitching forward motions using the AWR1443BOOST TI radar, shown in Figure 3.12. Table 4.3 presents the AWR1443BOOST radar configuration used for this experiment. As shown in Figure 4.16, the DJI Phantom 3 standard UAV is throttling up at a distance of 25 m in front of the AWR1443BOOST radar. After that, the UAV starts to pitch forward towards the radar at a speed of 1.5 m/s. The range-Doppler images of the throttling up and pitching

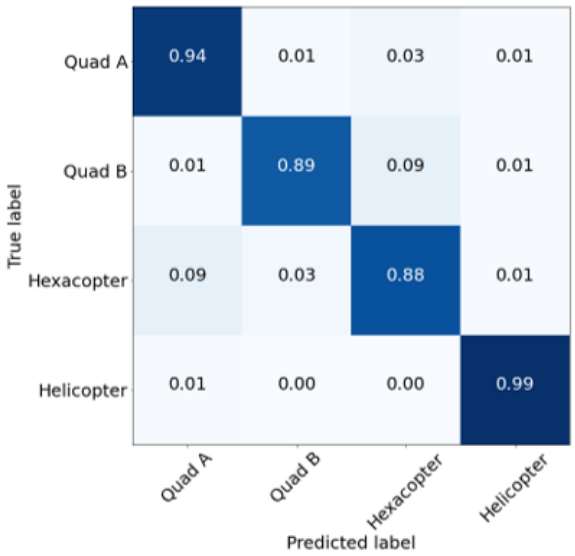


Figure 4.13: A Confusion matrix for applying the proposed MCML algorithm to dataset 4.

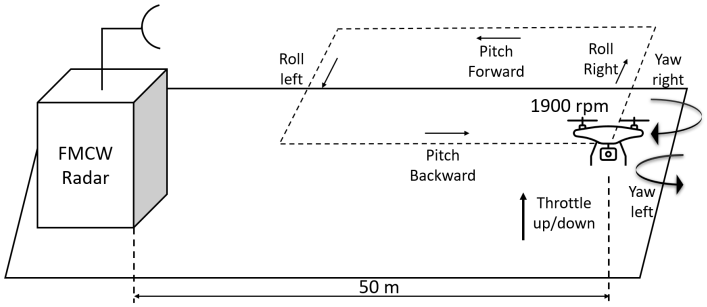
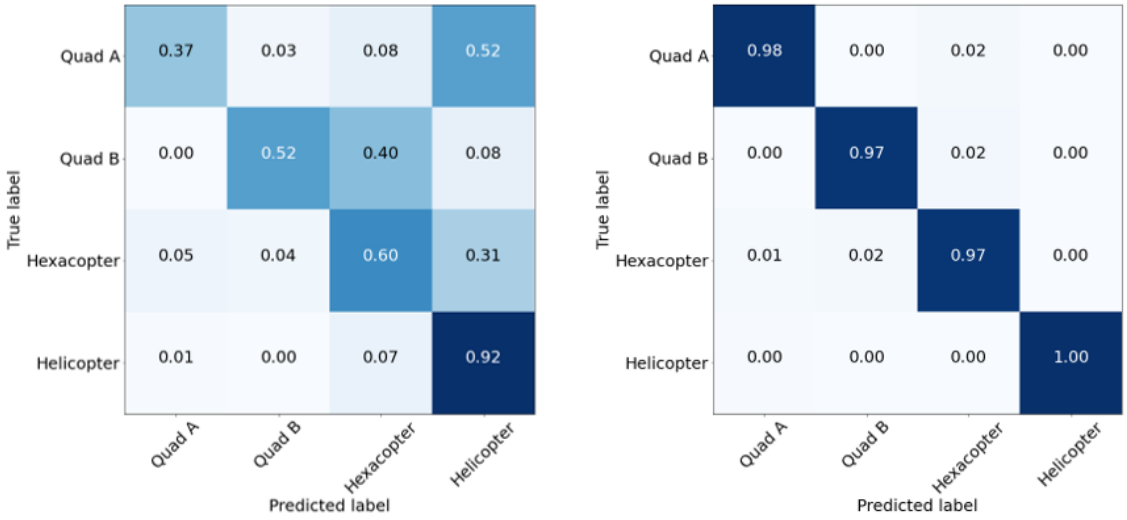


Figure 4.14: Simulation setup for all motions scenario.



(a) (b)

Figure 4.15: A confusion matrix of applying the DopplerNet classifier on the full motions scenario according to (a) The state-of-the-art literature. (b) The proposed MCML method.

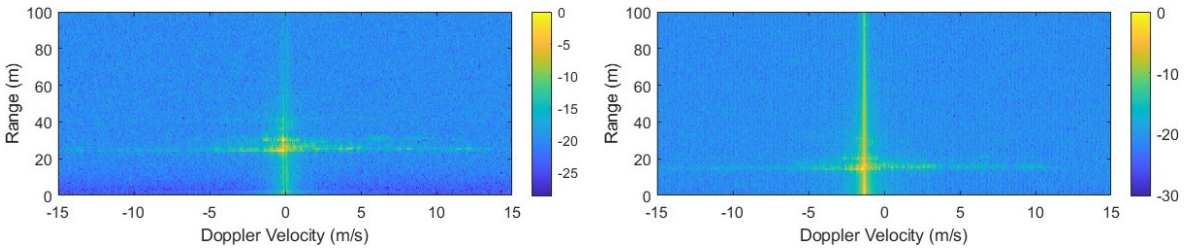
forward movements are shown in Figure 4.17a,b. The range-Doppler images depicted in Figure 4.17, which are consistent with the range-Doppler images generated for the MD4-1000 quadcopter using the proposed method in Chapter 3 as illustrated in Figure 4.6a,c, highlight the strong dependence of range-Doppler images of UAVs on their mechanical control information.

Table 4.3: The AWR1443BOOST TI radar configuration.

Quantity	Symbol	Value
Center Frequency	f_0	77 GHz
Bandwidth	BW	750 MHz
Range Resolution	ΔR	0.2 m
Velocity Resolution	ΔV	0.0694 m/s
Maximum Range	R_{max}	100 m



Figure 4.16: Measurements setup of the DJI Phantom 3 standard quadcopter.



(a) (b)

Figure 4.17: Range-Doppler images for DJI Phantom 3 standard when it: (a) Throttles up. (b) Pitches forward.

Chapter 5

Improvement of UAV Detection and Classification

5.1 Introduction

In this chapter, an investigation on the impact of antenna's Field of View (FOV) on the accuracy of Machine Learning (ML) algorithms to classify Unmanned Air Vehicles (UAVs) is presented. In the state-of-the-art literature, ML algorithms were trained and tested on the same datasets that were generated under a particular condition where the relative angle between the UAVs and the antenna was kept at 0°. Contrary to conventional practices, a ML algorithm is trained on a dataset that is generated under a particular condition where the relative angle between the UAVs and the antenna is kept at 0° and is then tested across a range of relative angles, from 20° to 90°. As the relative angle between the UAVs and the antenna increases, observational results show a decline in ML classification accuracy.

Multiple-Input Multiple-Output (MIMO) radar technology has become an essential tool for UAV detection and classification. Multiple antennas are used by MIMO radars at both the transmission and reception ends, improving range performance and spatial resolution. When compared to conventional Single-Input Single-Output (SISO) radar systems, the usage of MIMO radars improves UAV detection and classification accuracy, lowers clutter and interference, and improves overall Signal to Noise Ratio (SNR). MIMO radars are a viable choice for modern UAV surveillance and defense systems because they can distinguish between UAVs and other objects in the airspace more clearly [30, 31, 32, 33, 34, 35, 36, 37, 38, 39, 40, 41, 42, 43, 44, 45].

Although MIMO radars improve the detection and classification of UAVs, they struggle with detecting and classifying multiple UAVs at wide relative angles. For this, a Range-Doppler Integration while Steering (RDIwS) beamforming-based method is proposed. Radar beamforming increases the detection probability of UAVs by electronically guiding the antenna beam in a certain direction. Additionally, radar beamforming improves the spatial resolution of UAVs and increases the SNR for them, ensuring the detection and classification of small UAVs [46, 47, 48, 49, 50, 51, 52, 53, 54, 55]. The RDIwS beamforming-based method divides the antenna FOV into sectors and focuses the radar energy on the targets within each sector. The range-Doppler maps that are obtained for each sector are then integrated to create a range-Doppler map for the entire scene. This method significantly improves the SNR of UAVs and enhances the radar system's capability to detect and classify multiple UAVs at wide angles. In addition, compared to the conventional steering & tracking beamforming-based method, the RDIwS beamforming-based method is simple as it does not require reconfiguring the radar multiple times during one operation and it uses the max available power of the antenna with no need to split this power to multiple beams to track multiple targets, which offers a longer range detection.

5.2 Mathematical Background

Assume we have a MIMO radar system with M Transmitters (TXs) and N Receivers (RXs), and a single point target is positioned in front of the radar at a particular angle. The beat signal at the l^{th} antenna element is given by [42]:

$$x_l(t_f, t_s) = b_l e^{-j[2\pi f_{beat} t_f + \frac{2v_r t_s}{\lambda_{max}} + \tau_l + \alpha_l + \Delta\psi_l(t_f, t_s)]} + e_l(t_f, t_s) \tag{5.1}$$

in (5.1), t_f and t_s represent the fast and slow time indices, respectively. b_l and α_l denote the channel's mismatched magnitude and phase. v_r, τ_l, λ_{max}, $e_l(t_f,t_s)$, $\Delta\psi_l(t_f,t_s)$ represent the target's radial velocity, the phase shift at the l^{th} RX, the wavelength, the additive noise, and the residual phase noise, respectively. While f_{beat} denotes the beat frequency that is used to calculate the range information.

To obtain the Angle of Arrival (AoA) information and generate the range-angle maps, the Capon beamformer is used [48, 42]. The Capon beamformer, a spatial filtering technique, facilitates the estimation of AoA in the presence of both noise and interference, it involves the formulation of a weight set for the elements of the array, optimizing the SNR of the received signal [48, 42].

The fundamental principle of the Capon beamformer revolves around identifying the optimal weight set for the array elements, thereby minimizing the output power while

adhering to a constraint on the desired signal power [48, 42]. The determination of these optimal weights entails solving an optimization problem that necessitates the inversion of a covariance matrix derived from the received signals [48, 42]. By rearranging terms in (5.1) and consolidating the received signals from all RX channels into a column vector, the Capon approach enables the estimation of AoA. Mathematically, it can be expressed as [48, 42]:

$$\mathbf{x}(t_f, t_s) = \mathbf{\Gamma} \cdot \mathbf{a}(\theta) \cdot y(v, f_b, t_f, t_s) + \mathbf{e}(t_f, t_s) \tag{5.2}$$

$$\mathbf{\Gamma} = \begin{pmatrix} b_1 \cdot e^{-j\alpha_1} & 0 & 0 \\ 0 & \ddots & 0 \\ 0 & 0 & b_l \cdot e^{-j\alpha_l} \end{pmatrix} \tag{5.3}$$

$$\mathbf{a}(\theta) = \begin{pmatrix} e^{-j\tau_1} \\ \vdots \\ e^{-j\tau_l} \end{pmatrix} \tag{5.4}$$

$$y(v_r, f_{beat}, t_f, t_s) = e^{-j[2\pi f_{beat} t_f + \frac{2v_r t_s}{\lambda_{max}} + \Delta\psi_l(t_f, t_s)]} \tag{5.5}$$

where θ is the estimated AoA, $\mathbf{\Gamma}$ depends on the channel gain/phase mismatches, and $\boldsymbol{a}$ is the steering vector. If multiple targets are present at varying ranges, each with a different beat frequency, the received vector can be obtained as the sum of the individual received vectors from each target. Mathematically, this can be expressed as [48, 42]:

$$\mathbf{x}(t_f, t_s) = \mathbf{\Gamma} \cdot \mathbf{A}(\theta) \cdot \mathbf{Y}(v, f_b, t_f, t_s) + \mathbf{e}(t_f, t_s) \tag{5.6}$$

where $\boldsymbol{A}$ is a matrix with K columns representing each target's steering vector, and Y is a matrix with the elements of $y(v_r, f_{beat}, t_f, t_s)$ as its diagonal entries. $\boldsymbol{A}$, v_r, and f_{beat} are the unknown parameters. However, only the elements of $\boldsymbol{A}$ depend on the RX channel indices. Therefore, the matrix Y has no contribution to the covariance of $\boldsymbol{x}$. In fact, the covariance matrix of x can be computed as follows when the additive noise is uncorrelated to Y [48, 42]:

$$\mathbf{R} = E(\mathbf{x} \cdot \mathbf{x}^H) = P_s \cdot \mathbf{\Gamma} \cdot \mathbf{A}(\theta) \cdot \mathbf{A}^H(\theta) \cdot \mathbf{\Gamma}^H + \mathbf{R_n} \tag{5.7}$$

where P_s represents the power of the signals and $\boldsymbol{R_n}$ is the noise covariance. The computation of the Capon output filter spectrum relies on the positive definiteness and invertibility of the covariance matrix $\boldsymbol{R}$ [48, 42].

$$\mathbf{\Phi}(\hat{\theta}) = \frac{\mathbf{a}}{\mathbf{a}^H(\hat{\theta}) \cdot \mathbf{R}^{-1} \cdot \mathbf{a}(\hat{\theta})} \tag{5.8}$$

by utilizing the angle information obtained from the Capon beamformer and the range calculated through the first Fast Fourier Transform (FFT) of the received signal, a range-angle map is generated for the target.

MIMO radar systems improve the SNR of a target compared with SISO radar systems. The SNR of a SISO radar system can be expressed as [56, 57]:

$$SNR_{SISO} = \frac{P_r}{N_0} = \frac{P_t G^2 \lambda^2 \sigma}{(4\pi)^3 R^4 N_0} \tag{5.9}$$

where P_r is the received power, P_t is the transmitted power, $G = \frac{4\pi}{\lambda^2} A_e$ is the antenna gain, λ is the signal wavelength, A_e is the effective aperture of the received antenna, σ is the target's Radar Cross-Section (RCS), R is the target's range (distance between the antenna and the target), and N_0 is the RX noise, which is considered to be thermal noise.

The SNR of a MIMO radar system with M TXs and N RXs, SNR_{MIMO}, can be derived as follows [31]: Let P_i be the transmitted power of the i^{th} antenna, $i = 1, 2, ..., M$, and A_j^e be the effective aperture of the j^{th} received antenna, $j = 1, 2, ..., N$. Assuming all antennas have the same gain, G, the power of the j^{th} received signal from the i^{th} reflected transmitted signal is:

$$P_{ij}^{MIMO} = \frac{P_i G \sigma A_j^e}{(4\pi)^2 R^4} \tag{5.10}$$

where A_j^e is the effective aperture of the j^{th} received antenna. After mixing the power at the j^{th} received antenna from all the i^{th} reflected signals, we get:

$$P_j^{MIMO} = \sum_{i=1}^{M} P_{ij}^{MIMO} = \sum_{i=1}^{M} \frac{P_i G \sigma A_j^e}{(4\pi)^2 R^4} = \frac{G \sigma A_j^e}{(4\pi)^2 R^4} \sum_{i=1}^{M} P_i \tag{5.11}$$

The total power after processing for all antennas is:

$$P^{MIMO} = \sum_{j=1}^{N} \frac{G \sigma A_j^e}{(4\pi)^2 R^4} \sum_{i=1}^{M} P_i = \frac{G\sigma}{(4\pi)^2 R^4} \sum_{i=1}^{M} P_i \sum_{j=1}^{N} A_j^e \tag{5.12}$$

where $\sum_{j=1}^{N} A_j^e = \sum_{j=1}^{N} \frac{G_j \lambda^2}{4\pi}$. Assuming that antennas have the same gain, G, then $\sum_{j=1}^{N} \frac{G_j \lambda^2}{4\pi} = \frac{NG\lambda^2}{4\pi}$, and $\sum_{i=1}^{M} P_i = MP_t$, assuming $P_i = P_t, i = 1, 2, ..., M$. Then equation (5.12) becomes:

$$P^{MIMO} = \frac{MP_t N G^2 \lambda^2 \sigma}{(4\pi)^3 R^4} \tag{5.13}$$

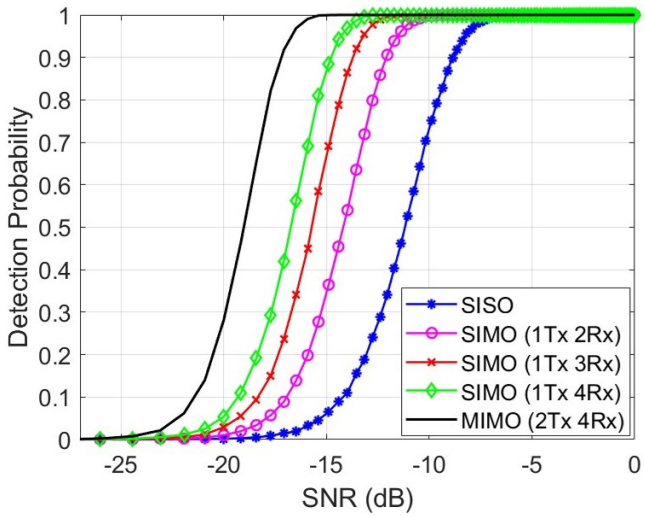


Figure 5.1: ROC curve depicting the detection probability of the TI radar.

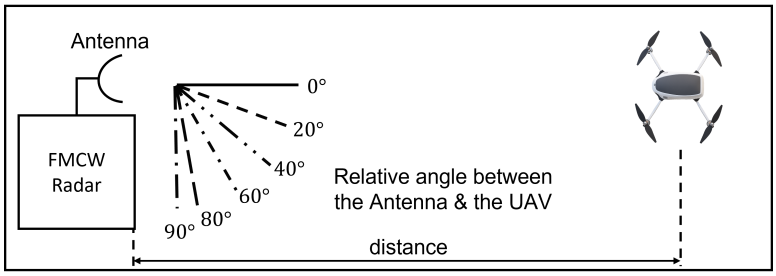
Then the SNR of a MIMO radar system can be expressed as:

$$SNR_{MIMO} = \frac{MNP_tG^2\lambda^2\sigma}{(4\pi)^3R^4N_0} \tag{5.14}$$

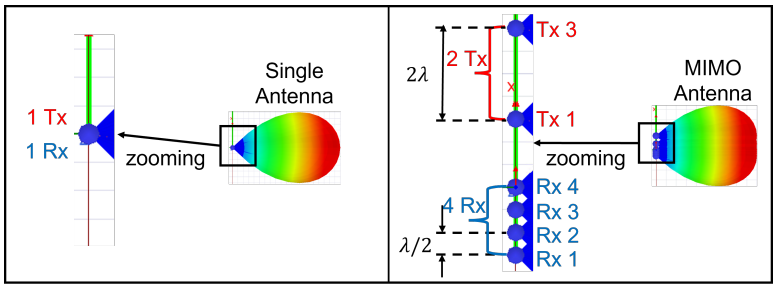
Comparing equation (5.9) and equation (5.14), the SNR of a MIMO radar system is improved by MN times the SNR of a SISO radar system, as shown below:

$$SNR_{MIMO} = MN \times SNR_{SISO} \tag{5.15}$$

The significance of equation (5.15) lies in the augmentation of SNR through the inclusion of more TX and RX antennas, effectively elevating the number of channels. In the context of the AWR1443BOOST Texas Instruments (TI) radar, equipped with 3 TXs and 4 RXs, diverse combinations of these elements impact the SNR and the radar detection probability. Substantiating this notion, the Receiver Operating Characteristics (ROC), shown in Figure 5.1 which is generated using MATLAB, demonstrates equation (5.15). Specifically, the implemented MIMO antenna case (2TX & 4RX) in this investigation displays a substantial increase in detection probability compared to the SISO antenna and the Single-Input Multiple-Output (SIMO) antenna cases. For instance, at an approximate SNR of $-17.5\ dB$ and a false alarm probability $P_{fa} = 10^{-5}$, the detection probability for the implemented MIMO antenna case reaches 0.9, while it stood at 0 for the SISO antenna case.



(a)



(b)

Figure 5.2: (a) Top-view of the simulation setups for the UAVs at different angles. (b) The used SISO antenna (left) and MIMO antenna (right).

Figure 5.2a shows the test setup in a top-view configuration, illustrating the UAVs at various relative angles. The UAVs are positioned at a distance of 1 m from the radar, aligning with the laboratory measurements conducted for the validation of this study. This work utilized two distinct setups for experimentation. The first setup featured a configuration comprising a SISO antenna, as depicted in Figure 5.2b (left side). In contrast, the second setup, illustrated in Figure 5.2b (right side), involved a MIMO antenna equipped with two TXs and four RXs, with an antenna spacing of $d = \lambda/2$ designed to align with the AWR1443BOOST TI radar specifications [2].

5.3 MIMO and SISO Radars Classification Results

Seven UAVs are considered in this work; a fixed-wing, a helicopter, four quadcopters, and a hexacopter UAVs. This section presents the ML results pertaining to the classification of the seven UAVs considered in this work. The dimensions of the seven UAVs are shown in Table 5.1. A Convolutional Neural Network (CNN) algorithm, based on the DopplerNet CNN algorithm [23], is employed in this study. A millimeter-Wave (mm-Wave) Frequency-

Table 5.1: Dimensions of the used UAVs.

UAV	**Dimensions** (m)
Fixed-wing	$0.74 \times 0.2 \times 0.15$
Helicopter	2.65×0.56, blade 3.75
Quadcopter A	$0.178 \times 0.232 \times 0.127$
Quadcopter B	$1.136 \times 1.730 \times 0.495$
Quadcopter C	Diagonal 0.35, blade 0.24
Quadcopter D	Diagonal 0.25, blade 0.14
Hexacopter	Diagonal 0.9, frame arm 0.358

Table 5.2: Radar configuration & antenna parameters.

Parameter	**Value**
Center Frequency	79 GHz
Bandwidth	3.460 GHz
Maximum Range	5.5 m
Range Resolution	0.0433 m
Velocity Resolution	0.0174 m/s
Antenna Beam Width	60°
Antenna Polarization	Vertical
Antenna Gain	10.5 dBi
Output Power	21 dBm
Number of Channels	8 (2 TX & 4 RX)
Spacing between Antennas	$\lambda/2$
Field of View	±90°

Modulated Continuous-Wave (FMCW) radar operating at a center frequency of 77 GHz is utilized. The radar has a bandwidth of 3.46 GHz, resulting in a range resolution of 4.33 cm. The radar system is based on the AWR1443BOOST TI radar platform [2]. This radar configuration contains 3 TXs and 4 RXs, with the first and third TXs utilized for obtaining the azimuth angle information, and the second TX designated for obtaining the elevation angle information. However, in the specific test setup of this investigation, elevation angle information is considered unnecessary, given the UAVs and the radar are positioned at the same elevation angle, as shown in Figure 5.2a. Consequently, only the first and third transmitters are utilized, resulting in the use of 2 TXs and 4 RXs in this study, as shown in Figure 5.2b. Detailed radar parameters are provided in Table 5.2. The same radar configuration is used in simulations to generate synthetic datasets.

5.3.1 Synthetic Datasets

In this subsection, the classification results for the CNN model using synthetic datasets are provided. Based on the simulation setup shown in Figure 5.2a, a dataset containing a total of 1600 range-Doppler maps, 1400 range-Doppler maps for the seven UAVs (200 frames/UAV) and 200 range-Doppler maps for an additional empty class, is generated at a relative angle of 0° to train the CNN model. Figure 5.3a–g shows the seven UAVs used in this study, accompanied by their respective range-Doppler images. The dataset is divided

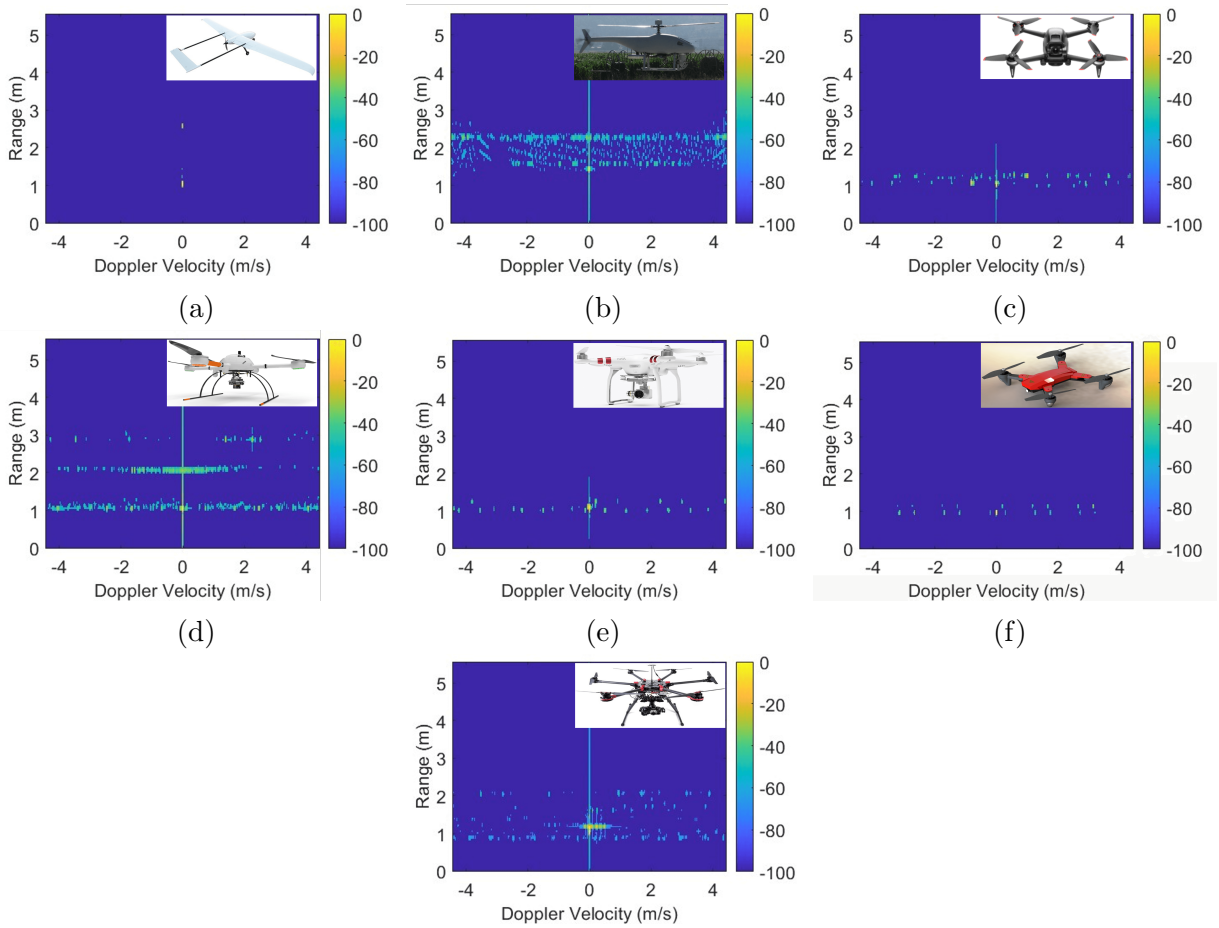
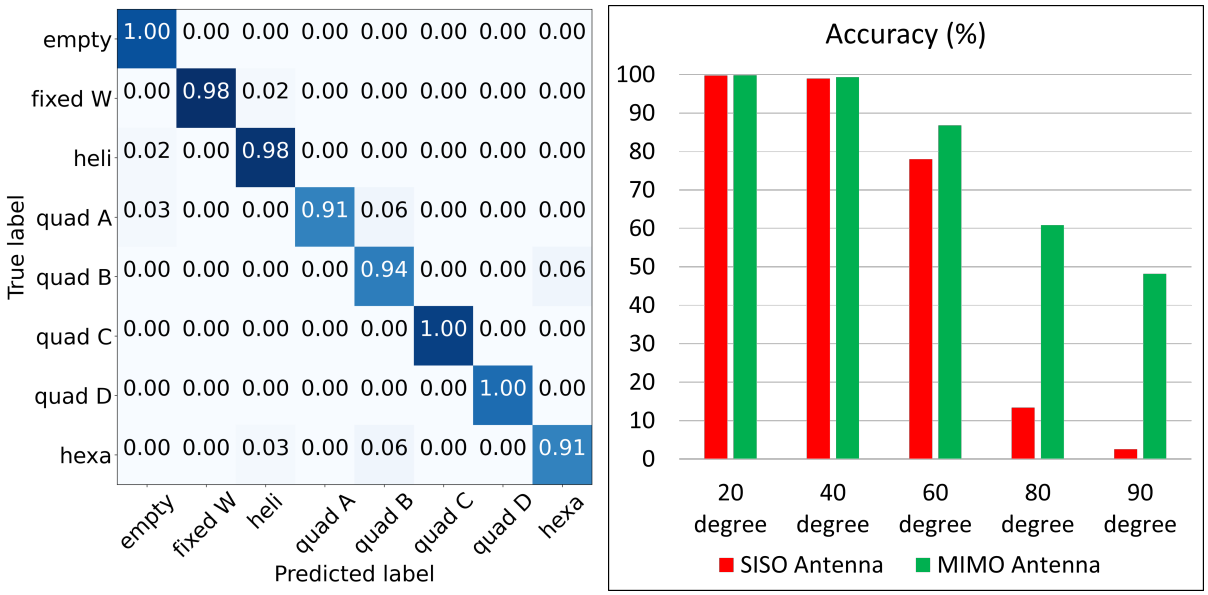


Figure 5.3: Range-Doppler images for the seven UAVs at a relative angle of 0°. (a) Fixed-wing. (b) Helicopter. (c) Quadcopter A. (d) Quadcopter B. (e) Quadcopter C. (f) Quadcopter D. (g) Hexacopter.



(a) (b)

Figure 5.4: (a) The confusion matrix of the CNN algorithm at a relative angle of 0°. (b) A Comparison between the CNN classification accuracy using the SISO and the MIMO antennas at various relative angles.

into a training set and a test set with a ratio of 80% and 20%, respectively. The CNN algorithm underwent training using the dataset generated at a relative angle of 0° between the antenna and the UAVs, resulting in an accuracy of 96.5%, as shown in Figure 5.4a.

In order to assess the accuracy of the trained CNN algorithm, it is evaluated on datasets generated at the other five angles, each dataset contains 1400 range-Doppler maps for the seven UAVs (200 frames/UAV). It's important to note that there is no overlap between these datasets. This assessment is conducted for two scenarios: utilizing a SISO antenna and employing a MIMO antenna. A comparison of the classification accuracy between the SISO and MIMO antenna scenarios at the five different relative angles is presented in Figure 5.4b. For both scenarios, the CNN algorithm exhibits similar accuracy levels at relative angles of 20° and 40°, surpassing 99%, as the UAVs are within the antenna FOV. At the 60° angle, the CNN algorithm achieves moderate accuracy in classifying the seven UAVs, as the UAVs are not entirely within the antenna's FOV. However, for the 80° and 90° angles, the CNN algorithm struggles to classify the UAVs due to their positions lying outside the antenna's FOV. Significantly, using a MIMO antenna in the same test setup leads to enhanced accuracy of the CNN algorithm, because of the improved SNR of the UAVs. The confusion matrices for testing the trained CNN model on synthetic datasets

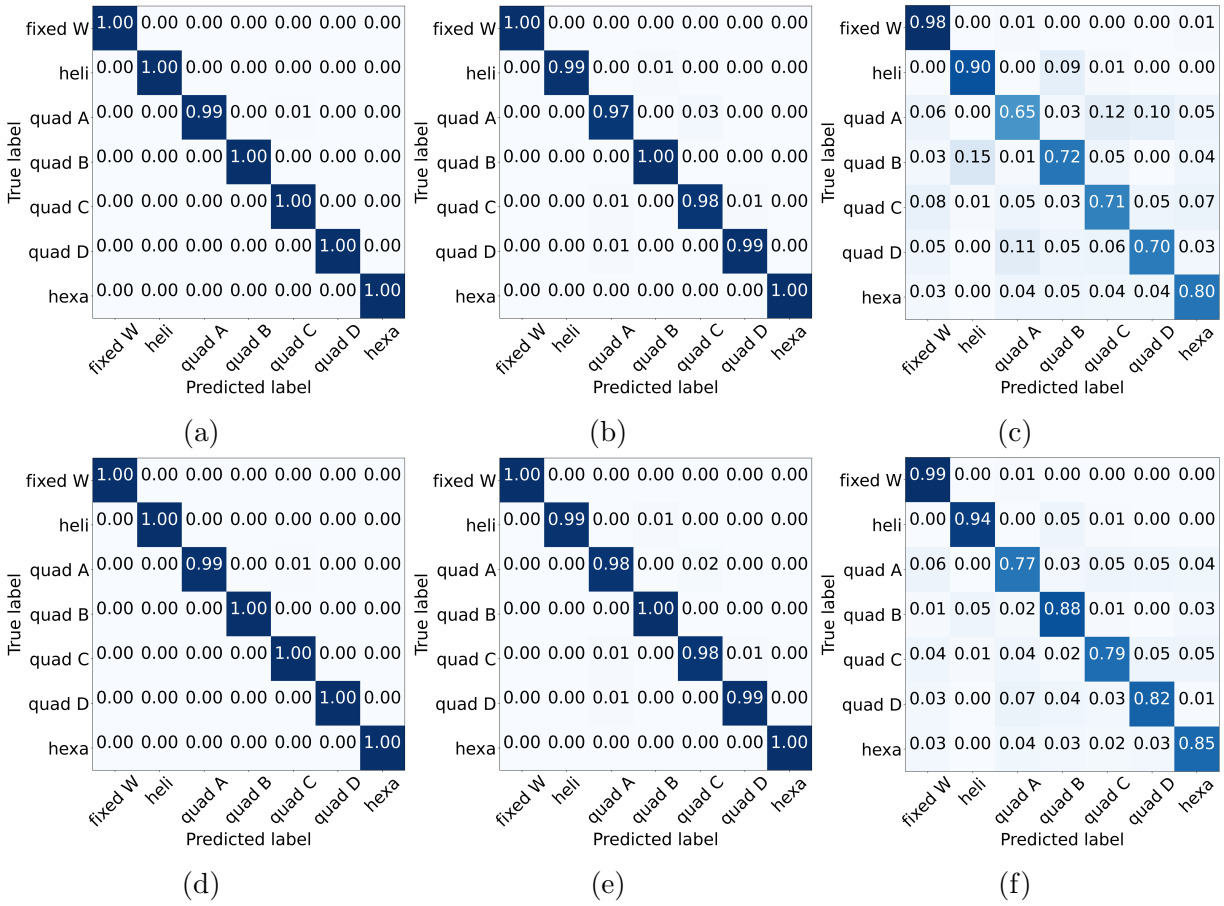


Figure 5.5: The confusion matrices for testing the trained CNN model on synthetic datasets at different angles for both the SISO and MIMO antenna cases. (a) 20° SISO antenna. (b) 40° SISO antenna. (c) 60° SISO antenna. (d) 20° MIMO antenna. (e) 40° MIMO antenna. (f) 60° MIMO antenna.

at 20°, 40°, and 60° relative angles for both the SISO and MIMO antenna cases are shown in Figure 5.5a–f.

5.3.2 Real-Measurements Datasets

To further validate the results, a series of datasets are generated using the TI radar, capturing the range-Doppler information of quadcopter C and quadcopter D. One dataset is generated at 0° relative angle between the two UAVs and the antenna, which contains

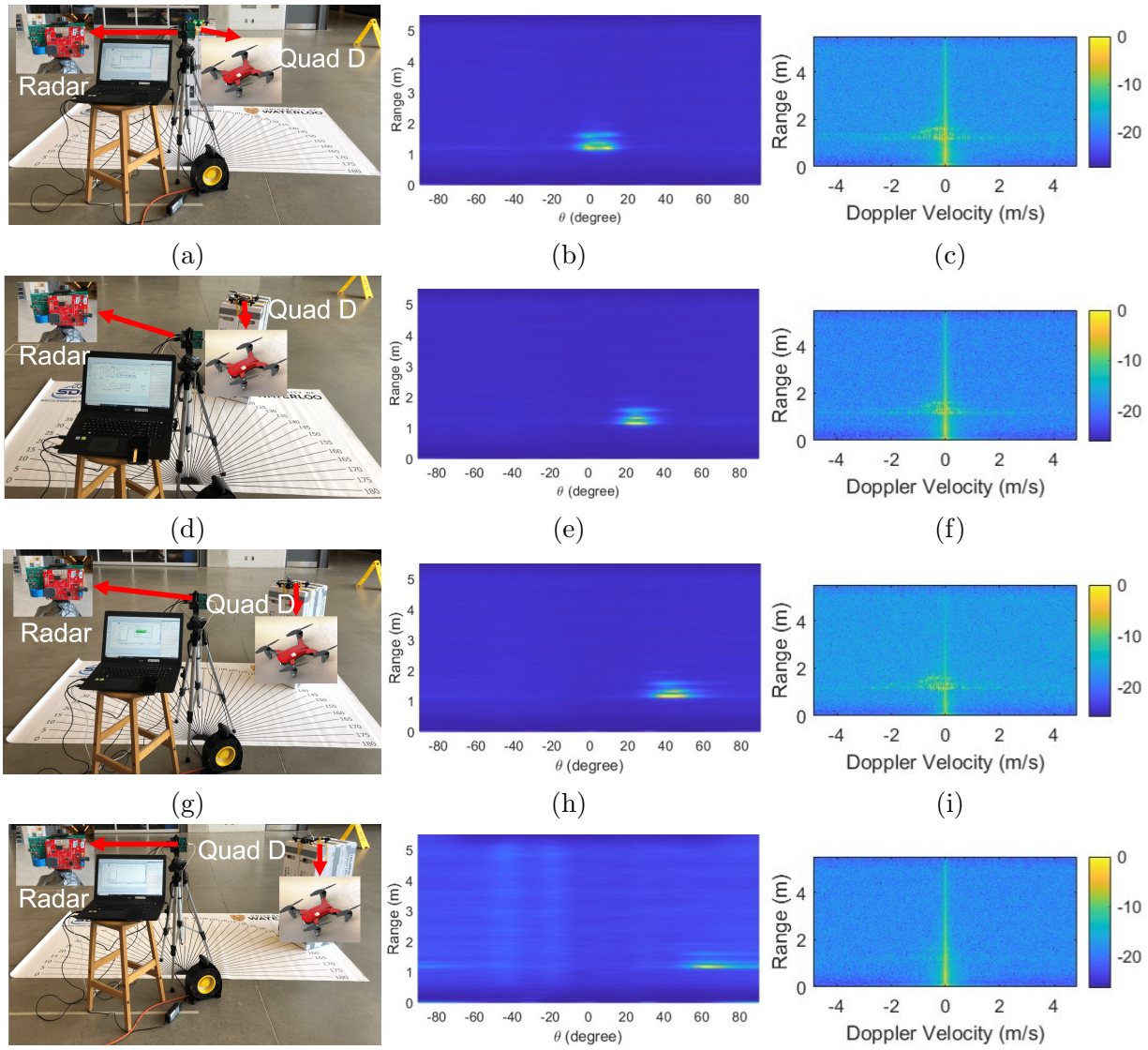


Figure 5.6: Experimental setups for quadcopter model D at different angles. (a) 0° setup. (b) 0° range-angle. (c) 0° range-Doppler. (d) 20° setup. (e) 20° range-angle. (f) 20° range-Doppler. (g) 40° setup. (h) 40° range-angle. (i) 40° range-Doppler. (j) 60° setup. (k) 60° range-angle. (l) 60° range-Doppler.

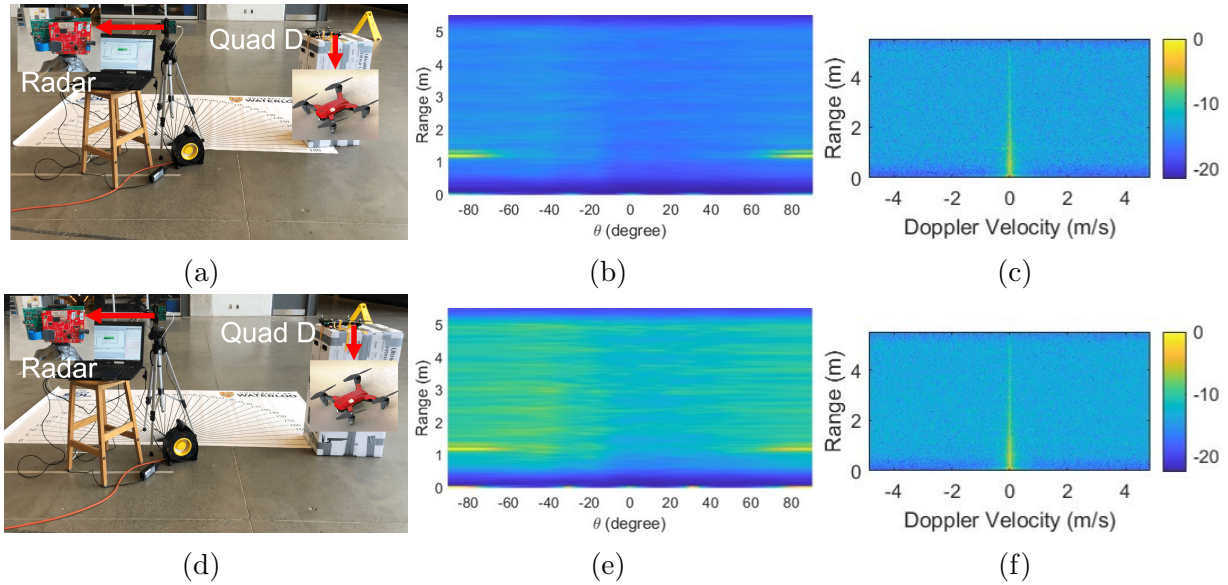
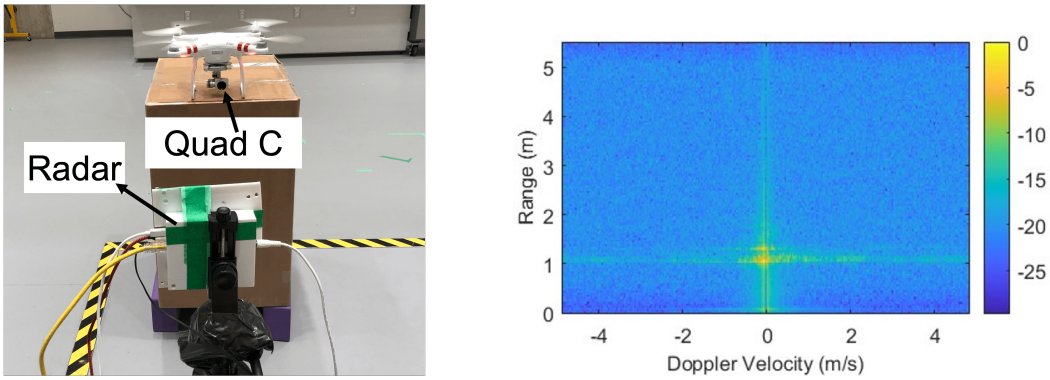


Figure 5.7: Experimental setups for quadcopter model D at different angles. (a) 80° setup. (b) 80° range-angle. (c) 80° range-Doppler. (d) 90° setup. (e) 90° range-angle. (f) 90° range-Doppler.

514 range-Doppler maps for each of the two quadcopters. While five other datasets are generated for quadcopter D only at different relative angles of 20° to 90° with respect to the radar, each of them contains 514 range-Doppler maps for quadcopter D. Figure 5.6a,d,g,j and Figure 5.7a,d illustrate the experimental setups where quadcopter model D is positioned 1 m away from the AWR1443BOOST TI radar at six different angles. The resulting range-angle maps for these particular configurations for quadcopter model D are presented in Figure 5.6b,e,h,k and Figure 5.7b,e, while the resulting range-Doppler maps are presented in Figure 5.6c,f,i,l and Figure 5.7c,f. For quadcopter model C, the experimental setup and the range-Doppler map for this UAV positioned 1 m from the AWR1443BOOST TI radar are shown in Figure 5.8a and Figure 5.8b, respectively.

In a manner consistent with the simulations, the CNN algorithm is trained using a dataset containing range-Doppler information obtained from real-measurements. These measurements are obtained using the AWR1443BOOST TI radar for quadcopter C and quadcopter D, with a fixed relative angle of 0° between the UAVs and the radar. In addition, an empty class consisting of 440 frames is included in this dataset, the numbers of 514 frames for the quadcopters and 440 frames for the empty class are determined by the duration during which the radar was operational to capture these frames. The dataset is divided into a training set and a test set with a ratio of 80% and 20%, respectively.



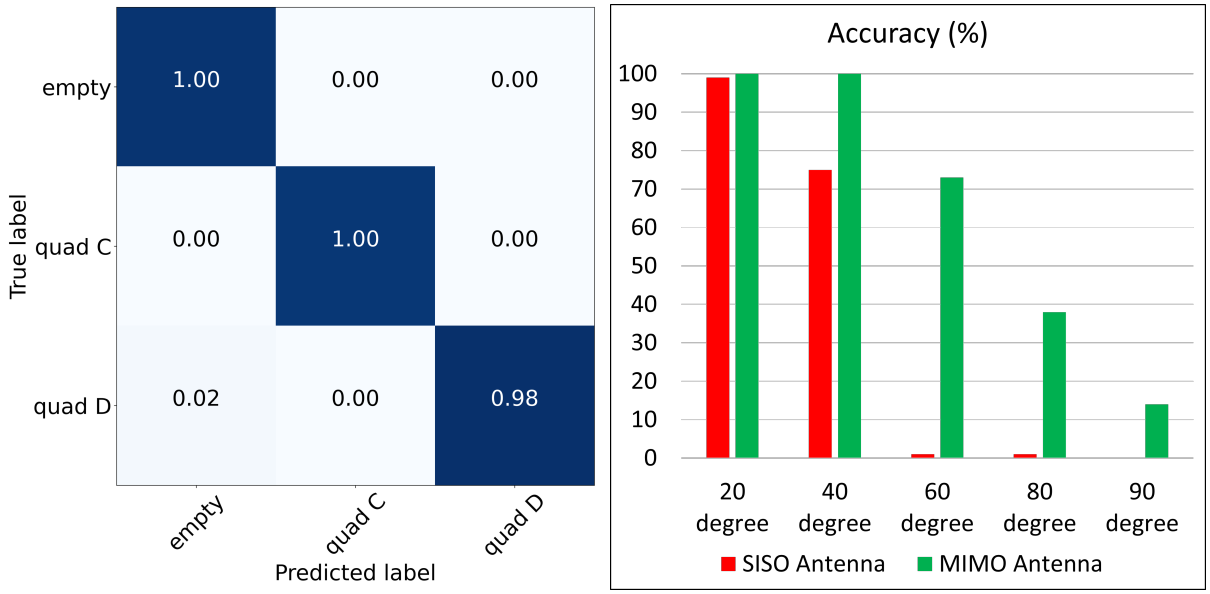
(a) (b)

Figure 5.8: (a) Experimental setup for quadcopter model C. (b) range-Doppler map of quadcopter model C at a relative angle of 0° with respect to the radar.

The CNN algorithm demonstrates excellent performance, achieving an accuracy exceeding 98% during its evaluation. The resulting confusion matrix, representing the classification performance of the CNN algorithm on the real-measurement dataset, is depicted in Figure 5.9a.

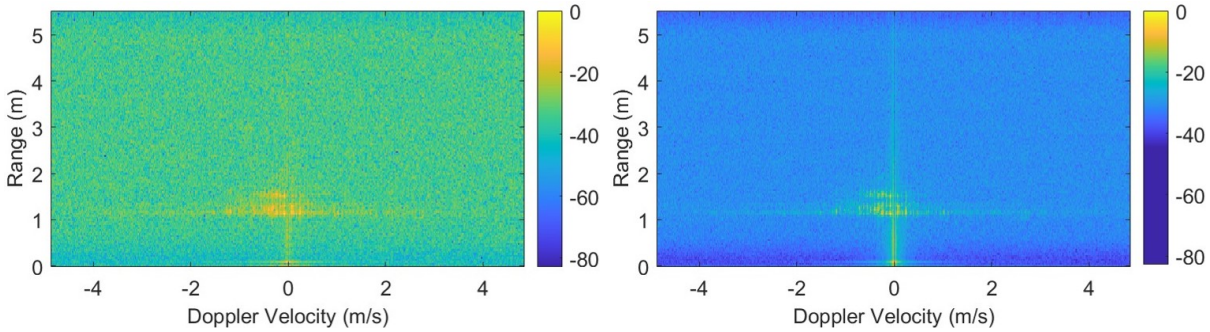
The CNN algorithm, which is trained on a real-measurement dataset at a relative angle of 0°, is tested for two scenarios: the first using a SISO antenna and the second using MIMO antennas. For each scenario, the CNN algorithm is applied to the datasets obtained through real-measurements of quadcopter D at relative angles ranging from 20° to 90° with respect to the radar. Figure 5.9b presents a comparison of the classification results of the CNN algorithm for quadcopter D at various angles using SISO and MIMO antenna scenarios, demonstrating agreement with the simulation results.

Analysis of the CNN classification outcomes using synthetic datasets revealed a decline in classification accuracy as the relative angle between UAVs and antennas increased. Notably, for both SISO and MIMO antenna scenarios, the classification accuracy is similar for relative angles of 20° and 40°, as evidenced in Figure 5.4b. Impressively, even when UAVs are partially within the antenna's FOV at a 60° relative angle, the CNN model still demonstrates accurate classifications. However, for relative angles of 80° and 90°, the employment of MIMO antennas yielded a marked enhancement in classification accuracy due to the augmented SNR of the UAVs, as elucidated in equation (5.15). For example, Figure 5.10a,b, show the range-Doppler maps for quadcopter D at a relative angle of 40° using SISO and MIMO antennas, respectively, which illustrates the enhancement in SNR achieved by utilizing MIMO antenna systems compared to SISO antenna systems. This improvement contributes to the enhanced detection and classification of UAVs.



(a) (b)

Figure 5.9: (a) Classification results of the CNN algorithm for the real-measurements dataset at a relative angle of 0° with respect to the radar. (b) Classification results of the CNN algorithm for quadcopter D at different angles.



(a) (b)

Figure 5.10: Range-Doppler maps for quadcopter D at relative angle of 40° using: (a) SISO antenna. (b) MIMO antenna.

The experimental results presented in Figure 5.6 indicate that the radar system exhibits accurate detection of the UAV at angles of 0°, 20°, 40°, and 60°. However, a notable decrease in detection performance is observed at angles of 80°, and 90°. Furthermore, the analysis reveals a weakening of the range-Doppler signature of the quadcopter as the angle

of incidence increases. These results suggest a dependency of a radar's detection capability on the incident angle, with a diminishing performance observed at higher angles, thus potentially impacting the range-Doppler characteristics of a UAV.

The findings of this study underscore the significance of employing MIMO radars for UAV detection and classification purposes. MIMO radars offer several advantages, including an enhanced SNR compared to conventional SISO radar systems. This higher SNR contributes to enhanced accuracy in UAV detection and classification. Consequently, the utilization of MIMO radars is pivotal in improving the effectiveness of UAV detection and classification systems. However, the findings also show that MIMO radars struggle with detecting and classifying UAVs at wide relative angles as shown in Figures 5.4b and 5.9b. In order to overcome this limitation, a RDIwS beamforming-based method is introduced in the next section.

5.4 RDIwS Beamforming-Based Method for UAV Detection and Classification

Radar beamforming is an advanced signal processing technique that has completely changed the field of radar technology. The ability to precisely adjust the directionality of radar's antenna beams is crucial to current radar systems. Beamforming offers unmatched levels of accuracy in radar systems across many civil and military applications. Radar beamforming is fundamentally based on the fundamentals of phased array antenna systems and signal processing. Electronic beamforming directs the radar beam by dynamically altering the phase and amplitude of signals from various antenna elements. Radar beamforming is an important technique for UAV detection and classification. By electronically steering the antenna beam to specific directions, radar beamforming increases the detection probability of UAVs. In addition, radar beamforming increases the SNR for UAVs, ensuring the detection of small sizes of UAVs, and improves spatial resolution of UAVs [46, 47, 48, 49, 50, 51, 52, 53, 54, 55].

Beamforming is achieved by using an array of TXs as shown in Figure 5.11. Assuming M is the number of TXs and the spacing between them, d, is equal, which means the distance between the first and second TXs is d, and the first and last TXs is $(M-1)d$. In order to steer the beam or direct it to a specific angle, θ, the phase for each TX is calculated according to [146]:

$$\boldsymbol{\phi} = \begin{bmatrix} \phi_1 & \phi_2 & \dots & \phi_M \end{bmatrix} = \begin{bmatrix} 0 & 2\pi\frac{d}{\lambda}\sin\theta & 2\pi\frac{2d}{\lambda}\sin\theta & \dots & 2\pi\frac{(M-1)d}{\lambda}\sin\theta \end{bmatrix} \tag{5.16}$$

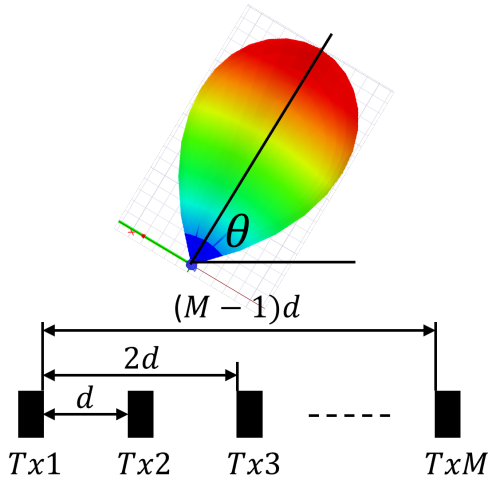


Figure 5.11: Beamforming using an array of transmitters.

Assuming the antenna spacing $d = \frac{\lambda}{2}$, equation (5.16) becomes:

$$\boldsymbol{\phi} = \begin{bmatrix} 0 & \pi \sin\theta & 2\pi \sin\theta & \dots & (M-1)\pi \sin\theta \end{bmatrix} \tag{5.17}$$

In this section, a RDIwS beamforming-based method is proposed to enhance the detection and classification of UAVs at different angles and in the presence of multiple UAVs. The method works by dividing the MIMO antenna FOV space into sectors and steering the antenna beam across these sectors to focus the radar energy on the targets within these sectors. Subsequently, the range-Doppler maps obtained within each sector are integrated to provide a range-Doppler map for the whole FOV space. This is obtained by averaging the range-Doppler maps calculated through equation (3.1) as follows:

$$\frac{1}{N} \sum_{\theta=1}^{N} RDM_{\theta}(t, f) \tag{5.18}$$

where N is he number of steered angles, $RDM_{\theta}(t, f)$ is the range-Doppler map at each steered angle.

5.4.1 Performance Analysis of the RDIwS method

In this subsection, a performance analysis of the RDIwS beamforming-based method is presented. A comparison between the detection probability of a radar system using MIMO

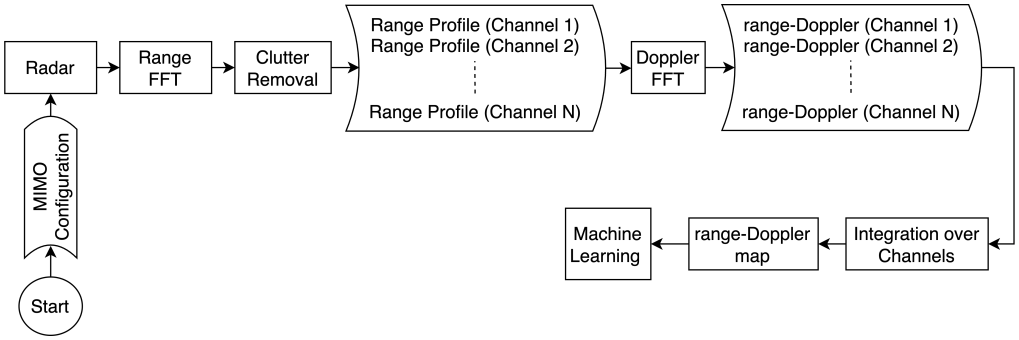


Figure 5.12: Signal processing algorithm for a MIMO radar system.

antenna configuration, a radar system using steering-only beamforming, a radar system using steering & tracking beamforming, and beamforming using the proposed RDIwS in different scenarios is illustrated using the ROC curves. For more clarification, Figures 5.12, 5.13, 5.14, and 5.15 show the signal processing chain for a MIMO radar system, a radar system using steering-only beamforming, a radar system using the proposed RDIwS beamforming-based method, and a radar system using steering & tracking beamforming, respectively. As shown in Figure 5.12, the radar is configured to work in a MIMO mode, then a FFT is applied to the radar's raw data to the fast axis to obtain the range information for each of the radar's channels. Subsequently, another FFT is applied to the slow axis to get the Doppler information for each channel. Then, integration of the radar's channels is applied to get the range-Doppler maps required for ML work. While, as shown in Figure 5.13, the radar is configured to work on a beamforming mode, then the same procedure for obtaining the range-Doppler maps is followed for each of the steered angles. Eventually, the range-Doppler maps for all the angles are inputted to ML for classification. On the other hand, as shown in Figure 5.14, the proposed RDIwS beamforming-based method algorithm differs from the steering-only beamforming algorithm by integrating the range-Doppler maps from all steered angles together before applying ML models to them. This significantly enhances the SNR in a simple and fast way. Finally, as shown in Figure 5.15, the radar is configured to scan the space by steering the antenna beam. Then, after obtaining the angle information and the number of UAVs in the scene, another configuration is applied to produce several beams focusing on the UAVs directions. Although this technique allows tracking the UAVs accurately, it has some limitations in the complexity of changing the radar's configurations many times, dividing the antenna power over the number of beams needed to track the UAVs, and its tracking depends on the idea that the UAVs are moving in straight lines in the same directions which is not true all the time.

For simplicity, the antenna beamwidth is assumed to be 90°, which means at an angle of

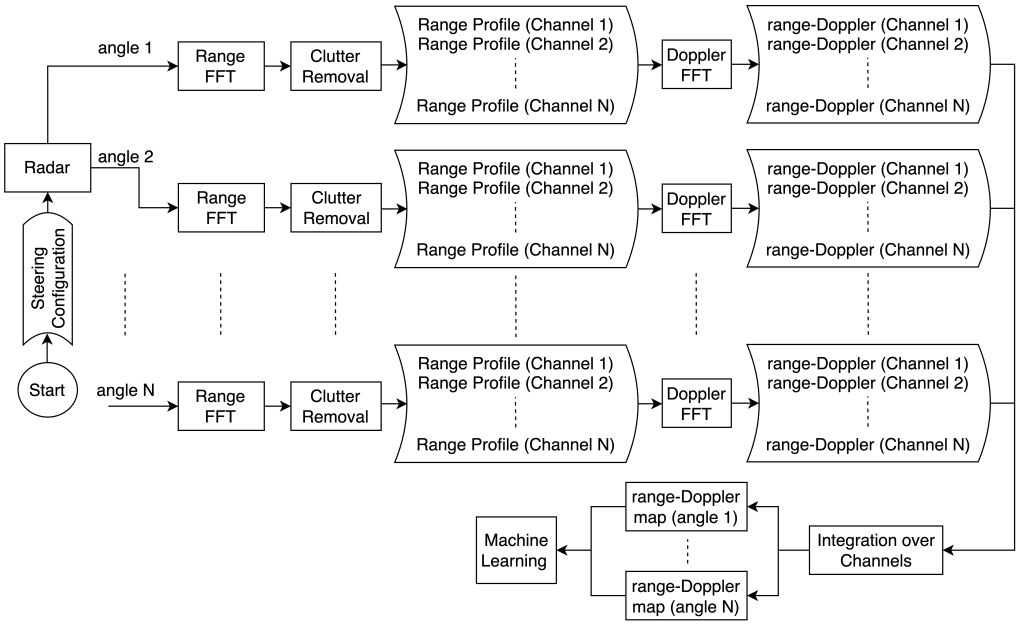


Figure 5.13: Signal processing algorithm for a beamforming (steering-only) radar system.

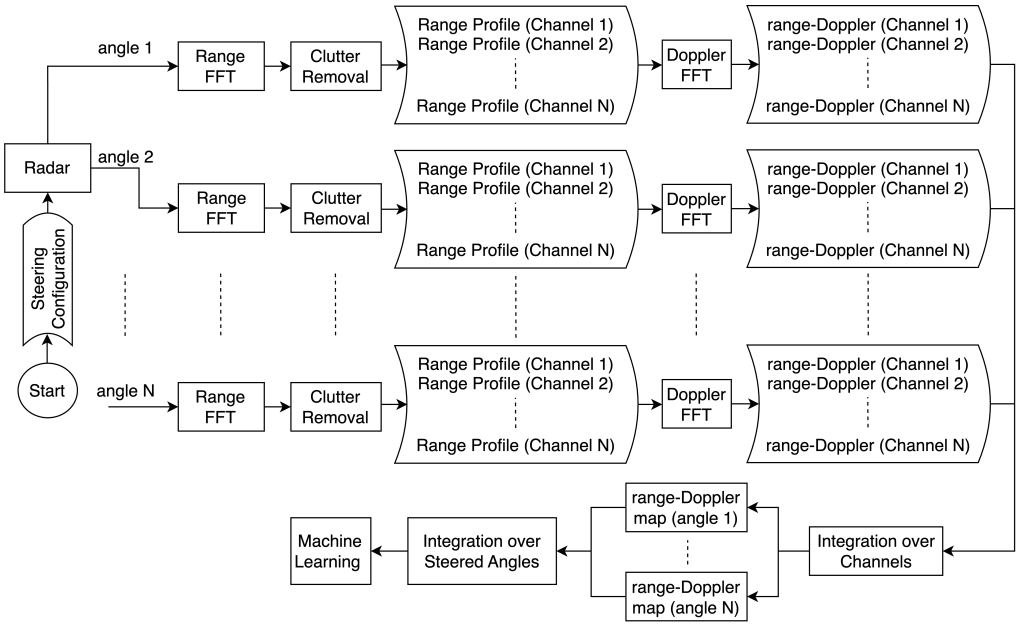


Figure 5.14: Signal processing algorithm for a beamforming-based RDIwS radar system.

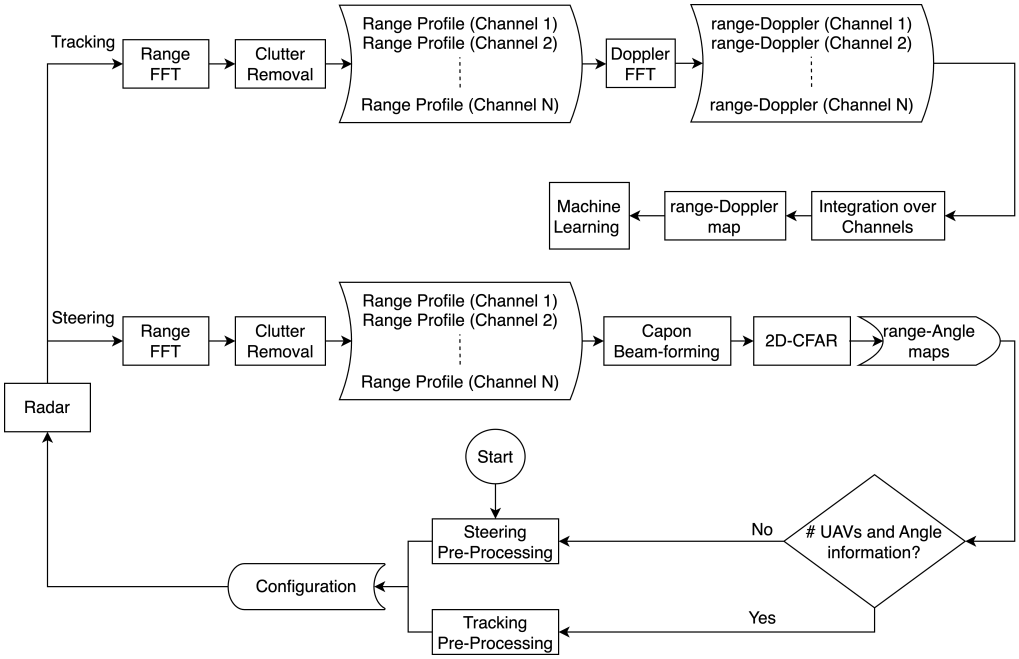


Figure 5.15: Signal processing algorithm for a beamforming (steering and tracking) radar system.

45°, the transmitted power is reduced by 3 dB. The performance of the proposed RDIwS beamforming-based method is compared to the other mentioned methods based on the following scenarios:

- A UAV is located at a relative angle of 0° with respect to the radar.
- A UAV is located at a relative angle of 45° with respect to the radar.
- Two UAVs are located closely within the maximum power of the radar.
- Two UAVs are located at relative angles of ±45° with respect to the radar.
- Four UAVs are located closely within the maximum power of the radar.
- Four UAVs are located at relative angles of ±45° with respect to the radar (two UAVs are located closely at each angle).
- Four UAVs are located at different locations and different relative angles of ±45° and ±60° with respect to the radar.

Figure 5.16a–g, generated using MATLAB, show the ROC curves of the detection probability of the UAVs according to the above different scenarios at 10^{-5} probability of false alarm. Beamforming focuses the antenna energy in a specific direction which leads to enhancement in a target's SNR. Additionally, by using the proposed RDIwS beamforming-based method, more enhancement to a target's SNR is achieved. This is because it successfully reduces the impact of variations in random noise and helps to create a more stable and reliable detecting environment. As shown in Figure 5.16a, as the UAV is located within the maximum transmitted power from the antenna, a noticeable enhancement in the detection probability using the proposed RDIwS beamforming-based method compared to a conventional MIMO radar system and a steering-only beamforming-based method, the detection probability reaches nearly 75% at -30 dB SNR compared to no detection in the MIMO case, and 5% for steering-only case. While the detection probability using the beamforming-based methods remains the same compared to a reduction for the MIMO case when the UAV is located at a relative angle of 45° with respect to the radar, as shown in Figure 5.16b. Despite its complexity, the detection probability of the steering & tracking beamforming-based method is identical to the detection probability of the proposed RDIwS method as in this case, there is no need to split the antenna power to multiple beams as there is only one UAV in the scene.

On the other hand, by increasing the number of UAVs in a scene, the detection probability decreases for all cases when the UAVs are located closely in range. The presence of multiple targets within the Constant False Alarm Rate (CFAR) window indeed affects CFAR processing, it leads to an increase in the CFAR threshold level that subsequently decreases the detection probability. This effect is shown in Figure 5.16c–f. For example, the detection probability for the RDIwS beamforming-based method at -30 dB SNR is 75%, 45%, and 17.5% for the 1, 2, and 4 UAV cases, respectively. While when the UAVs are located at different ranges that do not affect the CFAR processing, the detection probability remains the same for the beamforming-based methods, with significant enhancement in the proposed RDIwS beamforming-based method, compared to no detection for MIMO radar system as shown in Figure 5.16g. In this case, the MIMO radar detects 2 out of 4 UAVs, and the detected UAVs have relatively higher RCS than the missed UAVs. In addition, the missed UAVs are located at wider relative angles which significantly affects the reflected energy from them. These reasons lead to a domination of the radar energy from the detected UAVs. On the other hand, using beamforming in general overcomes this effect.

The advantages of the proposed RDIwS beamforming-based method can be summarized as follows:

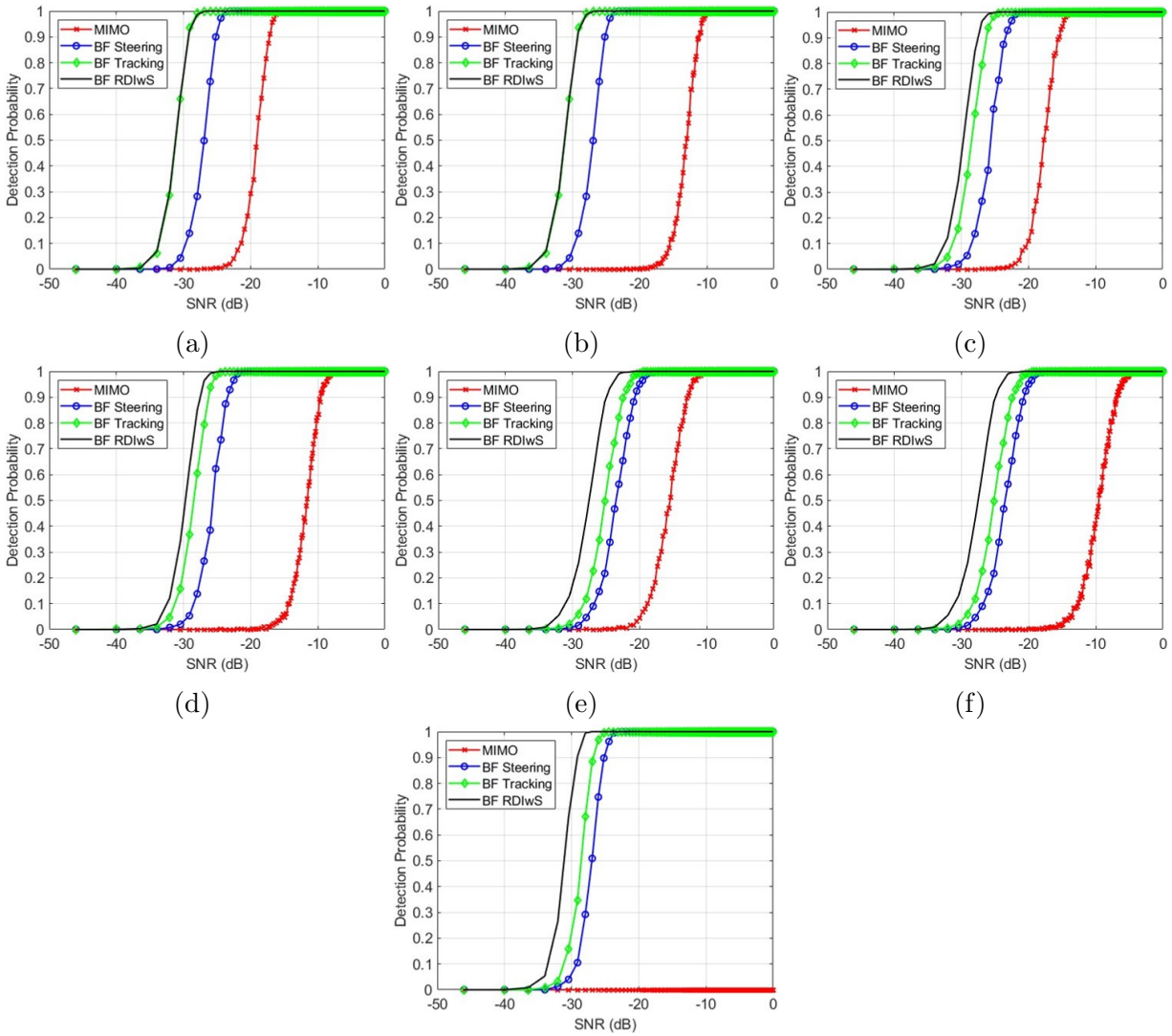


Figure 5.16: ROC curves for the performance of the beamforming methods compared to a traditional MIMO radar system at false alarm probability of 10^{-5} when: (a) A UAV at a relative angle of 0°. (b) A UAV at a relative angle of 45°. (c) Two UAVs within the maximum power. (d) Two UAVs at a relative angle of ±45°. (e) Four UAVs within the maximum power. (f) Four UAVs at a relative angle of ±45°. (g) Four UAVs at different locations and different relative angles of ±45° and ±60°.

- It enhances the SNR of radar targets which subsequently increases the radar's detection probability, especially in case of multiple UAVs at different angles.
- Its simplicity compared to the steering & tracking beamforming-based method as it does not require reconfiguring the radar multiple times during one operation.
- It uses the max available power of the antenna with no need to split this power to multiple beams as in the steering & tracking beamforming-based method which offers a longer range detection.
- It requires less hardware utilization compared to the steering & tracking beamforming-based method to have the same detection probability in case of multiple UAVs in a scene. For example, the steering & tracking beamforming-based method requires four times the hardware used for the RDIwS beamforming-based method to provide similar performance in the case of four UAVs present in a radar scene.
- No data augmentation is needed to overcome the low SNR of UAVs as presented in [79], in which data augmentation is used to improve ML accuracy at low SNR levels.

5.4.2 Evaluation of the RDIwS Method

To overcome the low classification accuracy at wide relative angles between the UAVs and the antenna, as shown in Figure 5.4b, beamforming is used to steer the antenna beam across the space and calculating the range-Doppler maps of the divided sectors. In the steering-only case, the range-Doppler maps for each sector are combined in one dataset to apply the trained ML algorithm on it, yielding an accuracy of around 77.5% across all angles. Steering the beam only improves the classification accuracy at wide angles, but it also decreases the classification accuracy by almost 20% for 20° and 40° relative angles and by almost 10% for 60° relative angle, as shown in Figure 5.17 (yellow). To increase the classification accuracy across all relative angles, the proposed RDIwS beamforming-based method is used. Instead of just combining the range-Doppler maps in one dataset representing all scanned sectors in the space, the range-Doppler maps for the UAVs in these sectors are integrated. This method increases the SNR of UAVs and enhances the radar detection probability, as shown in Figure 5.17 (blue).

In addition, an investigation is conducted to compare the performance of using the proposed RDIwS beamforming-based method in detecting and classifying multiple UAVs at different angles. Figure 5.18 shows the simulation setup used in this investigation. As

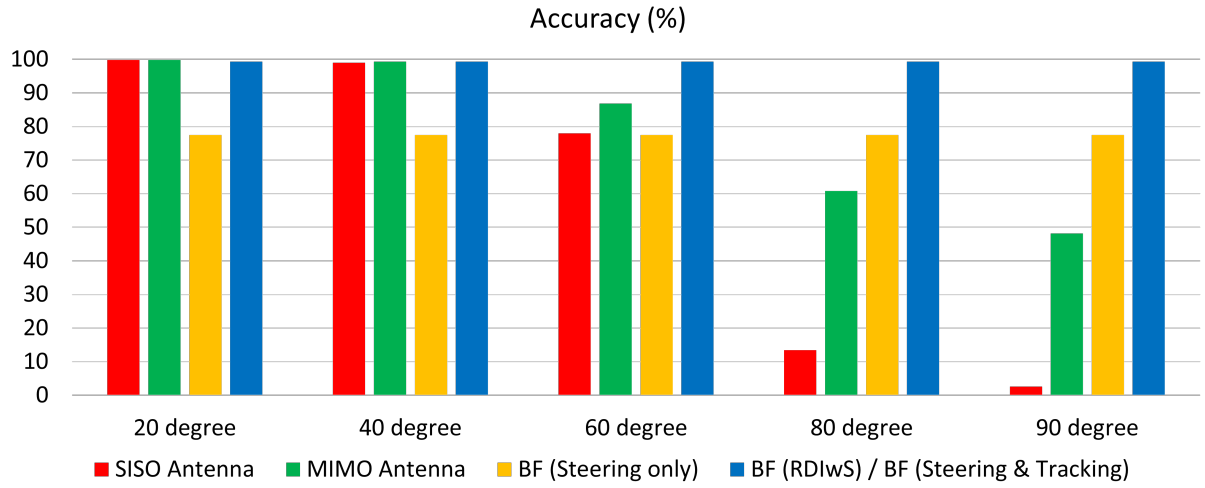


Figure 5.17: Comparison of the classification accuracy of different radar systems at different angles in case of only one UAV in the scene.

shown in Figure 5.18, four UAVs are used, a quadcopter at 60°, a fixed-wing at 30°, a helicopter at −30°, and a hexacopter at −60°. A MIMO radar is modeled with 4 TXs and 8 RXs with a spacing of 2.05 mm providing 32 virtual channels. The radar system has a FOV of ±71.85°, consistent with the radar parameters shown in Table 3.11 and employed in the investigation illustrated in Figure 3.11. The range-angle map of the MIMO radar is shown in Figure 5.19a. The MIMO radar detects only the fixed-wing and the helicopter UAVs as their echo signals overpowered the echo signals from the quadcopter and the hexacopter UAVs. This occurs for two main reasons, the first one is that the RCS for the helicopter and the fixed-wing UAVs are relatively higher than that of the quadcopter and the hexacopter UAVs. The second reason is that the fixed-wing and the helicopter locations are at closer relative angles with respect to the radar than the relative angles for the quadcopter and the hexacopter UAVs, which affects the echo signal power significantly. A ML algorithm, OneVsRest classifier [147], is trained on a dataset containing the range-Doppler information of each UAV individually, then the trained ML algorithm is evaluated using a dataset containing the range-Doppler maps for the UAVs as they are detected according to Figure 5.18. Although the ML algorithm is able to classify the helicopter and the fixed-wing UAVs together correctly, it fails to classify the four UAVs at the same time as the radar detects only two of them, yielding an accuracy of 0% to classify the four UAVs.

By using the proposed RDIwS beamforming-based method, the radar is able to detect

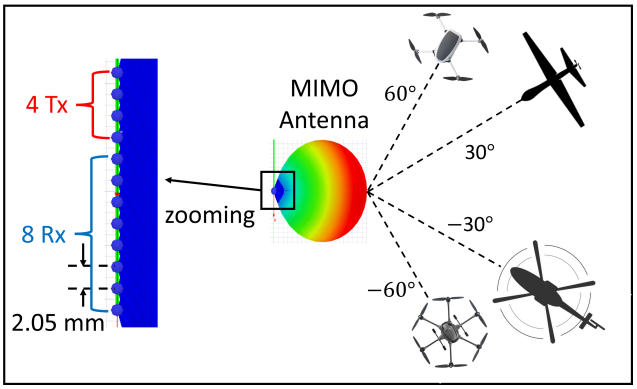
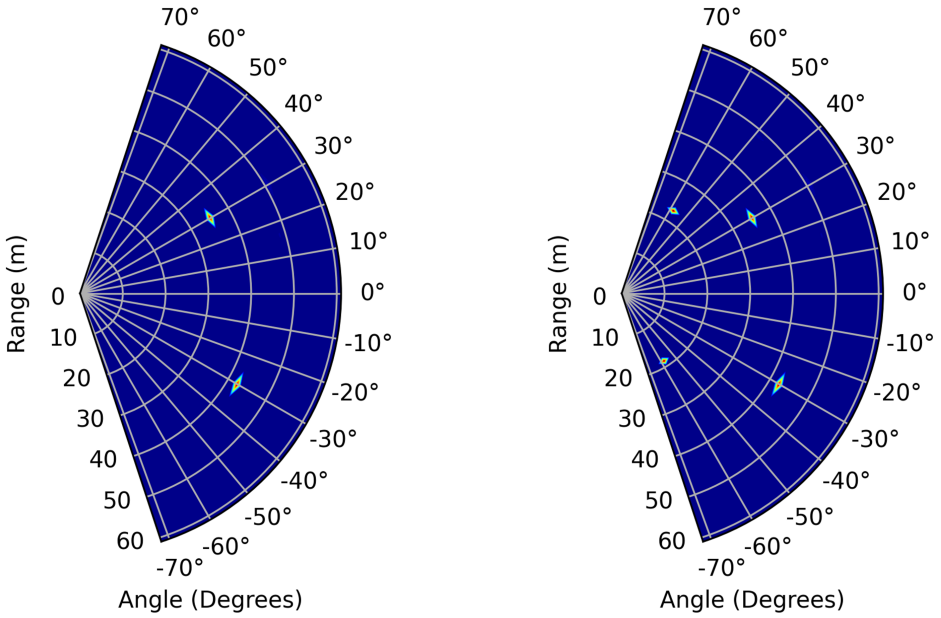


Figure 5.18: Simulation setup of multiple UAVs at different angles.



(a) (b)

Figure 5.19: Range-angle maps for four different UAVs when using: (a) MIMO radar. (b) RDIwS beamforming-based method.

the four UAVs at the same time as shown in the range-angle map in Figure 5.19b. The range-angle maps shown in Figure 5.19a,b represent the same frame obtained using the MIMO and the proposed RDIwS beamforming-based methods for fair comparison. The radar is able to detect the four UAVs using the proposed RDIwS beamforming-based

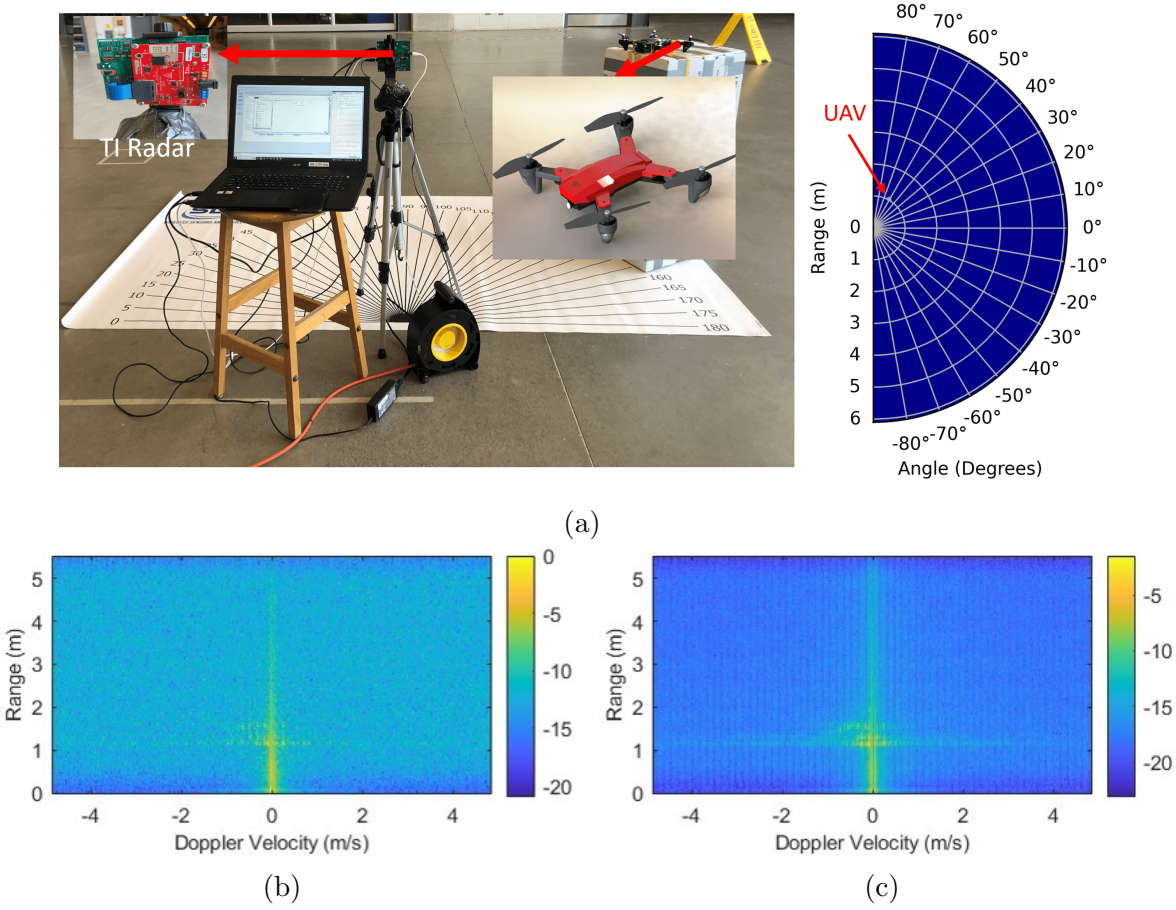


Figure 5.20: (a) A quadcopter UAV positioned 1 m in front of the radar at a relative angle of 60°. (b) Range-Doppler map of the quadcopter UAV using the traditional MIMO algorithm. (c) Range-Doppler map of the quadcopter UAV using the proposed RDIwS beamforming-based algorithm.

method as it allows the radar to focus the main power of its beam to each sector of the FOV space. Subsequently, the ML algorithm is able to classify the four UAVs with an accuracy of 95%. The detailed classification accuracy for each UAV is 100% for the helicopter UAV, 98% for the fixed-wing UAV, 90% for the quadcopter UAV, and 92% for the hexacopter UAV.

For further validation of the study's results, a series of datasets are generated employing the AWR1443BOOST TI radar system [2], its parameters are shown in Table 5.2. These datasets capture the range-Doppler information of a quadcopter UAV. Figure 5.20a displays

the test setup of these measurements, in which the quadcopter UAV is placed at a proximity of 1 m in front of the radar and the UAV maintains a defined relative angle of 60° concerning its orientation to the radar's location. These datasets encompass a range of relative angles, spanning from 0° to 90°, and a total of six datasets are meticulously generated to encapsulate this comprehensive range of scenarios. Figure 5.20b,c show the range-Doppler maps for the quadcopter UAV, as discerned through both the traditional MIMO algorithm and the proposed RDIwS beamforming-based method. These visual representations highlight the substantial impact of the RDIwS approach, which distinctly enhances the SNR attributed to the quadcopter UAV. The enhanced SNR directly translates to improved detection capabilities and higher accuracy in the classification of the quadcopter UAV, with the classification accuracy increasing from 85% for the MIMO method to over 97% for the RDIwS beamforming-based method. The comprehensive dataset and the resulting range-Doppler maps reaffirm the efficacy of the RDIwS beamforming-based method in enhancing radar performance. This method empowers radar technology to overcome detection and classification challenges, ultimately advancing its operational capabilities.

Although the RDIwS beamforming-based method presents notable advantages, it is accompanied by certain drawbacks outlined as follows: its reliance on a radar system equipped with beamforming capabilities, which is not universally available in many radar systems. Additionally, the temporal aspect of obtaining results poses a challenge, as the method necessitates the integration of range-Doppler maps from various steered angles. This, in turn, requires the system to await the completion of the radar beam steering process for each angle, introducing a temporal delay. Moreover, there is a potential susceptibility to clutter from diverse angles, particularly in scenarios where background clutter is nonhomogeneous, such as in varying weather or terrain conditions.

Chapter 6

Conclusions and Future Works

6.1 Conclusions

This thesis introduces a new method for generating radar datasets that contain UAV information using full-wave EM CAD tools. The method provides accurate modeling of the UAV's size, shape, and material characteristics in relation to its radar scattering behaviour. Six distinct types of UAVs are modeled to produce the initial dataset utilizing this new method, and the simulation is run using a modeled 77 GHz FMCW radar. The full-wave EM simulation results are used to extract the frames needed to build the dataset. The method provides accurate results for range-Doppler and micro-Doppler calculations. The six different UAVs in the generated dataset are classified with a CNN classifier, which has a classification accuracy of more than 97%. Additionally, the trained CNN algorithm is used in a new scenario with two identical UAVs moving in different directions, obtaining comparable levels of accuracy. The proposed method overcomes one of the most significant limitations in this field as it eliminates the constraints associated with real-world physical measurements. In addition, lab-measurements are performed using the DJI Phantom 3 standard quadcopter UAV to further validate the proposed methodology. When applied to the generated dataset using lab-measurements, the ML algorithm trained on the generated dataset using full-wave EM simulations produced results with high accuracy. By using EM simulation software, the proposed method enables the generation of datasets that are both realistic and scalable, allowing for the development and testing of ML algorithms under a wide range of scenarios.

Moreover, the proposed methodology makes it simple to look into attempts to deceive radar systems as it has the potential to improve the accuracy and effectiveness of UAV

detection and classification utilizing radar systems. Furthermore, this study extended its focus to the evaluation of ML algorithms in discerning and classifying UAVs amidst avian entities. The results unveiled a notable trend: the radar system's capacity to accurately detect and classify UAVs decreases proportionally as the number of avian subjects in a scene increases. When a single bird shares a scene with a UAV, the CNN model demonstrates an excellent classification accuracy of 99%. However, in circumstances where a UAV is navigating among a swarm of ten birds, this accuracy marginally decreases to 90%. The provided methodology allows defense scientists to carefully examine growing radar avoidance strategies. This simplifies the identification of present radar vulnerabilities and guides the creation of enhanced radar designs that are resistant to emerging stealth threats. The proposed approach presents a paradigm shift in how ML experts can approach the problem of UAV classifications.

Furthermore, the thesis introduces the impact of mechanical control information on range-Doppler images for UAVs. Two quadcopters, a hexacopter, and a helicopter UAVs are used in this investigation. The range-Doppler signatures are found to be highly dependent on the mechanical control information for each UAV. Utilizing eight distinct classifiers, the mechanical control information for the four UAVs is investigated for its impact on UAV classification. The proposed MCML method effectively addresses reduced classification accuracy in scenarios where UAV mechanical control information is not taken into consideration, achieving classifier accuracy exceeding 90%. Moreover, the trained MCML algorithm demonstrates high accuracy when applied to an unobserved dataset featuring random UAV motions with varying rotor's speeds. The MCML method proves superior in accuracy compared to state-of-the-art radar-based approaches for UAV classification.

Additionally in this thesis, the impact of an antenna's FOV on ML accuracy is investigated. Seven UAVs are measured with respect to an antenna at various relative angles ranging from 0° to 90°. A CNN classifier performs noticeably better when the relative angle shrinks. Interestingly, the ML method occasionally succeeds in accurately classifying particular UAV types even when only partial rotor's blade detection is feasible. A major factor in improving the classification accuracy of UAVs is the use of MIMO radars. Compared to conventional SISO radar systems, MIMO radars reduce clutter and interference while enhancing SNR, allowing for a more thorough detection and classification of UAVs. It is possible to accurately determine the relative angle between the UAVs and the antenna by utilizing the MIMO radar's ability to identify the AoA or direction of UAVs, improving predictions of a classifier's performance.

Although MIMO radars enhance the detection and classification of UAVs compared to SISO or Single-Input Multiple-Output (SIMO) radar systems, MIMO radars still struggle to accurately detect and classify UAVs in the presence of multiple UAVs at wider angles.

In order to overcome this issue, the thesis proposes a RDIwS beamforming-based method to further enhance the detection and classification of UAVs, especially in the presence of multiple UAVs at wider relative angles. The method works by dividing a MIMO antenna's FOV space into sectors and steering the antenna's beam across these sectors to focus the radar's energy on the targets within these sectors. Subsequently, the range-Doppler maps obtained within each sector are integrated to provide a range-Doppler map for the whole FOV space. The RDIwS beamforming-based method enhances the SNR of radar targets which subsequently increases the radar's detection probability for multiple targets at different angles. For four targets located at different angles and distances scenario, and at -30 dB SNR and false alarm probability of 10^{-5}, the RDIwS beamforming-based method has a detection probability of 75% compared to 5% for steering-only beamforming, and no detection for MIMO radar case.

6.1.1 Supplementary Resources

To better understand how the results in this thesis were obtained, a GitHub repository link is provided. This link contains resources such as ML algorithms, MATLAB codes, and synthetic datasets. These resources were employed to produce some results outlined in the thesis, contributing to improved reproducibility and clarity of the presented findings. The provided resources are summarized as follows:

- In the "`Ch3_Methodology`" folder, the initial dataset generated using the proposed method in chapter 3, named as (`Dataset`), and a Python code to apply and train the used CNN model, named as (`Ch3_methodology.py`), are included. Additionally, another Python code, named as (`Ch3_deceiveRadar_BladeLength.py`), and a dataset for the Phantom 3 standard UAV, named as (`Dataset_reducedBladeLength`), contains the range-Doppler information of the Phantom 3 standard UAV with a shorter blade length are available to investigate the impact of changing the blade length of the Phantom 3 standard UAV. The results produced by these codes, when applied to the provided datasets, correspond to Figure 3.9 and section 3.4 within chapter 3.

- In the "`Ch4_MCML`" folder, 3 datasets are provided, (`MCML_dataset1, MCML_dataset2, and MCML_dataset3`), which are explained in Table 4.2 within chapter 4. Additionally, 2 Python codes are provided, one named as (`Ch3_MCML.py`) to train the different ML algorithms used in this investigation, and another one named (`Ch4_MCML_test.py`) to test the trained ML algorithms. The trained ML algorithms using the proposed MCML method and not using the proposed MCML method are saved in folders

(`Trained MCML models`) and (`Trained not MCML models`), respectively. An explanation of how to train and test the ML algorithms and on which dataset is shown in detail in section 4.4 within chapter 4. The results obtained from the provided codes and datasets align with results shown in Figures 4.9, 4.10, 4.11b, and 4.12 within chapter 4.

- In the "`Ch5_FOV`" folder, 3 datasets are provided, (`0degree, 20degree, and 40degree`), these datasets contain the range-Doppler information of 7 UAVs and an empty class. Also, 2 Puthon codes are provided, one named as (`Ch5_FOV_train.py`) to train the CNN algorithms used in this work on (`0degree`), and another one named (`Ch5_FOV_test.py`) to test the trained ML algorithm on the (`20degree and 40degree`) datasets, it is saved as (`Trained_CNN_FOV.model`). An explanation of this process is shown in subsection 5.3.1, and the results obtained from the provided codes and datasets match Figures 5.4a and Figures 5.5d,e within chapter 5.

- In the "`Ch5_Performance_Analysis`" folder, 2 MATLAB codes are provided. One is named (`pfa.m`) and is used to calculate the value of the threshold factor which determines the false alarm probability needed. The other one is named (`pd.m`) and is used to calculate the detection probability of a radar system. Both codes are used in the performance analysis part of this thesis. For example, Figure 5.1 within chapter 5 is generated using these MATLAB codes. While Figure 5.16 within chapter 5 is generated following the same algorithm used in these codes.

The codes and datasets provided in the accompanying GitHub repository serve as illustrative examples showcasing the methodology and implementation for specific results discussed in this thesis. It is important to note that these resources do not comprehensively cover all the results presented in the thesis but rather aim to provide clarity and facilitate reproducibility for select outcomes.

6.2 Limitations and Future Works

Although the thesis has addressed some key limitations in the field of radar detection and classification of UAVs, some limitations need to be addressed in the future. These limitations are summarized as follows:

- Only two UAVs were used in real-measurements, and birds results were mainly obtained using radar-based digital twins. This is due to the availability of UAVs

and the practical constraints and complexity of acquiring these measurements. For the birds, it was not possible to take real-measurements for birds in a controlled-experiment setup. In future work, more UAVs should be taken into consideration for real-measurements and figuring out a way to fly birds in controllable directions to take real-measurements for them.

- For real-measurements, the distance for the tested UAV was within 100 m. This is because of the hardware constraints in using high-power radars that work in the W-band. According to Federal Communications Commission (FCC) [148], the total radiated power shall not exceed 50 dBm peak for $76-81$ GHz band radar which the same limit the TI radar used in this work follows, it has a maximum output power of 21 dBm [149, 150], which has a maximum detection range of 125 m for 500 MHz bandwidth. In future work, other radars that do not have this limitation should be used with adding power amplifiers.

- The signal processing done in this work was not in real-time operation. This work was done as a proof of concept with no need during this phase for working in real-time. In future work and real applications, the signal processing will be implemented to work in real-time.

- The datasets generated using the full-wave EM CAD tool do not consider any noise or clutter as this could not be modeled in the used EM CAD tool. Noise and clutter were taken into consideration in the theoretical analysis of the signal processing parts in this thesis, and in signal processing the real-measurements taken in this work. Although the proposed method's proficient performance in a real-world context, notwithstanding the absence of noise or errors during training, implies potential robustness and efficacy under ideal circumstances, however, in future work and based on the continuing discussion with the application engineers who develop the EM CAD tool used in this work, noise source will be employed to the simulations to obtain more realistic results.

- The thesis primarily utilized deterministic methods allowing for a detailed examination of deterministic aspects. However, the introduction of noise and clutter into the datasets in future work offers an avenue for a more comprehensive assessment, prompting the need for statistical approaches such as Regression Tree [151] and Natural Gradient Boosting [152] to consider probability and confidence in the results. These methods provide a nuanced understanding of uncertainties, contributing to more realistic modeling of scenarios and enhancing the overall validity and applicability of the research outcomes.

- Tracking models were not considered in this thesis. Tracking models provide information on the behavior of a UAV which may imply if this UAV is harmful or not. In future work, tracking models will be taken into consideration.
- ML methods used in this work were compared only in terms of their accuracy, precision, recall, and F1-score to classify UAVs. In reality, other factors such as memory usage, computational cost, and processing time should be taken into consideration for real-time operation. In future work, these parameters will be considered.
- This thesis focuses only on enhancing radar-based systems capabilities to detect and classify UAVs. Although the thesis succeeded in addressing some key limitations in the field and increased radar-based systems capabilities to detect and classify UAVs, fusion with other sensor types, such as cameras, may lead to more enhancement of the detection and classification of UAVs. In future work, sensor fusion will be considered for this purpose.

Despite the hardware limitations, the availability of UAVs, and the CAD tools constraints, the primary goal of the research was to establish and validate the proof-of-concept approaches and ideas presented in this thesis. Instead of offering a thorough and detailed analysis of all potential characteristics and aspects, the goal of this work was to demonstrate the viability and potential of the proposed concepts, leaving a detailed examination of its constraints for later, more in-depth studies.

6.3 Publications

6.3.1 Book Chapters

- A. N. Sayed, O. M. Ramahi, and G. Shaker, "Detection and Classification of Drones using Radars, AI, and Full-wave Electromagnetic CAD Tool," in *Drones – Various Applications*, D. D. M. Cvetković, Ed. Rijeka, Croatia: IntechOpen, 2023.

6.3.2 Journal Articles

- A. N. Sayed, O. M. Ramahi, and G. Shaker, "Machine Learning for UAV Classification Employing Mechanical Control Information," *IEEE Transactions on Aerospace and Electronic Systems*, pp. 1–14, May 2023.

- A. N. Sayed, M. M. Y. R. Riad, A. Ansariyan, L. Salman, O. M. Ramahi and G. Shaker, "UAV Classification using Neural Networks and Radar Digital Twins,". Under review.
- A. N. Sayed, H. Abedi, O. M. Ramahi and G. Shaker, "Enhanced UAV Detection and Classification using Machine Learning and MIMO Radars,". Under review.
- A. N. Sayed, O. M. Ramahi and G. Shaker, "RDIwS: An Efficient Beamforming-Based Method for UAV Detection and Classification,". Under review.
- A. N. Sayed, N. Rojhani, O. M. Ramahi and G. Shaker, "Improving UAV Classification: A Model-Based Augmentation Approach with Radar Digital Twin Datasets,". Under preparation.
- A. N. Sayed, O. M. Ramahi and G. Shaker, "On the Impact of Radar Clutter on the Detection and Classification of UAVs in Dense Urban Environments: A Study utilizing Radar Digital Twins,". Under preparation.
- A. N. Sayed, O. M. Ramahi and G. Shaker, "Comprehensive Radar-Based Digital Twin Datasets for UAVs and Avian Targets: A Resource for Advanced Surveillance and Classification Studies,". Under preparation.

6.3.3 Conference Papers

- A. N. Sayed, M. M. Y. R. Riad, O. M. Ramahi, and G. Shaker, "A Methodology for UAV Classification using Machine Learning and Full-Wave Electromagnetic Simulations," in *2022 International Telecommunications Conference (ITC-Egypt)*, Alexandria, Egypt, 2022, pp. 1–2.
- A. N. Sayed, O. M. Ramahi, and G. Shaker, "UAV Classification using Mechanical Control Information and Machine Learning," in *2023 International Microwave and Antenna Symposium (IMAS)*, Cairo, Egypt, 2023, pp. 1–2.
- A. N. Sayed, H. Abedi, O. M. Ramahi, and G. Shaker, "On the Impact of an Antenna Field of View on the Classification of UAVs," in *2023 International Workshop on Antenna Technology (iWAT)*, Aalborg, Denmark, 2023, pp. 1–2.
- A. N. Sayed, O. M. Ramahi, and G. Shaker, "UAV Detection & Classification Aided by Full-Wave Electromagnetic CAD Tools," in *2023 URSI International Symposium on Electromagnetic Theory (EMTS)*, Vancouver, BC, Canada, 2023, pp. 1–2.

- A. N. Sayed, O. M. Ramahi, and G. Shaker, "UAV Classification utilizing Radar Digital Twins," in *2023 IEEE International Symposium on Antennas and Propagation and USNC-URSI Radio Science Meeting (USNC-URSI)*, Portland, OR, USA, 2023, pp. 741–742.
- A. N. Sayed, H. H. Tran, O. M. Ramahi, and G. Shaker, "Radar-Based Digital Twins for Classification of UAVs and Avian Targets," in *2023 IEEE Microwaves, Antennas, and Propagation Conference (MAPCON)*, Ahmedabad, India, 2023, pp. 1–4.
- A. N. Sayed, O. M. Ramahi and G. Shaker, "UAV Detection and Classification Enhanced by RDIwS Beamforming-Based Method,". Under review.
- A. N. Sayed, O. M. Ramahi and G. Shaker, "In the Realm of Aerial Deception: UAV Classification via ISAR Images and Radar Digital Twins for Enhanced Security,". Under review.

References

[1] "Spreading wings s900 - dji," 2022. [Online]. Available: https://www.dji.com/ca/spreading-wings-s900

[2] "Awr1443boost evaluation board," 2023. [Online]. Available: https://www.ti.com/tool/AWR1443BOOST

[3] "Dca1000evm evaluation board," 2023. [Online]. Available: https://www.ti.com/tool/DCA1000EVM

[4] P. Wang, Z. Man, Z. Cao, J. Zheng, and Y. Zhao, "Dynamics modelling and linear control of quadcopter," in *2016 International Conference on Advanced Mechatronic Systems (ICAMechS)*, Melbourne, VIC, Australia, 2016, pp. 498–503.

[5] A. Alaimo, V. Artale, C. Milazzo, A. Ricciardello, and L. Trefiletti, "Mathematical modeling and control of a hexacopter," in *2013 International Conference on Unmanned Aircraft Systems (ICUAS)*, Atlanta, GA, USA, 2013, pp. 1043–1050.

[6] K. S. Khuwaja, B. S. Chowdhry, K. F. Khuwaja, V. O. Mihalca, and R. C. Ţarcă, "Virtual reality based visualization and training of a quadcopter by using rc remote control transmitter," *IOP Conference Series: Materials Science and Engineering*, vol. 444, no. 5, p. 052008, Nov. 2018.

[7] "Heathrow airport: Drone sighting halts departures - bbc news," 2022. [Online]. Available: https://www.bbc.com/news/uk-46803713

[8] "Drone sightings keep closing london's airports - bloomberg," 2022. [Online]. Available: https://www.bloomberg.com/news/articles/2019-01-09/drone-sightings-keep-closing-london-s-airports

[9] "Shrapnel injures 12 at saudi abha airport as drone intercepted - reuters," 2022. [Online]. Available: https://www.reuters.com/world/middle-east/saudi-led-coalition-says-destroyed-drone-launched-towards-abha-airport-4-injured-2022-02-10/

[10] "Iraq assassination attempt signals new era of non-state drone attacks - middle east eye," 2022. [Online]. Available: https://www.middleeasteye.net/opinion/iraq-assassination-new-era-drone-non-state-actors

[11] "Turkey closes diyarbakir airport for month after drone attack 'by pkk' - world - the times," 2022. [Online]. Available: https://www.thetimes.co.uk/article/turkey-closes-diyarbakir-airport-for-month-after-drone-attack-by-pkk-gmcj8skfz

[12] "Drone attack in abu dhabi kills 3 wounds 6 - cbc news," 2022. [Online]. Available: https://www.cbc.ca/news/world/abu-dhabi-drone-attack-1.6317555

[13] "Flights diverted at east midlands airport after drone sightings - air transport - the guardian," 2022. [Online]. Available: https://www.theguardian.com/world/2022/jun/11/flights-diverted-at-east-midlands-airport-after-drone-sightings

[14] "Rcmp charge two from b.c. after drone used to smuggle drugs into prison - ctv news," 2022. [Online]. Available: https://winnipeg.ctvnews.ca/drone-used-to-smuggle-drugs-into-manitoba-prison-rcmp-charge-two-men-from-b-c-1.5980061

[15] "Small drones are giving ukraine an unprecedented edge - wired," 2022. [Online]. Available: https://www.wired.com/story/drones-russia-ukraine-war/

[16] "Ukraine: How drones are changing the way of war - science - in-depth reporting on science and technology - dw," 2022. [Online]. Available: https://www.dw.com/en/ukraine-how-drones-are-changing-the-way-of-war/a-61681013

[17] M. A. Khan, H. Menouar, A. Eldeeb, A. Abu-Dayya, and F. D. Salim, "On the detection of unauthorized drones - techniques and future perspectives: A review," *IEEE Sensors J.*, vol. 22, no. 12, pp. 11 439–11 455, Apr. 2022.

[18] G. Lykou, D. Moustakas, and D. Gritzalis, "Defending airports from uas: A survey on cyber-attacks and counter-drone sensing technologies," *Sensors*, vol. 20, no. 12, pp. 1–35, Jun. 2020.

[19] S. Park, H. T. Kim, S. Lee, H. Joo, and H. Kim, "Survey on anti-drone systems: Components, designs, and challenges," *IEEE Access*, vol. 9, pp. 42 635–42 659, Mar. 2021.

[20] S. Samaras, E. Diamantidou, D. Ataloglou, N. Sakellariou, A. Vafeiadis, V. Magoulianitis, A. Lalas, A. Dimou, D. Zarpalas, K. Votis, P. Daras, and D. Tzovaras, "Deep learning on multi sensor data for counter uav applications—a systematic review," *Sensors*, vol. 19, no. 22, p. 4837, Nov. 2019.

[21] J. Flórez, J. Ortega, A. Betancourt, A. García, M. Bedoya, and J. S. Botero, "A review of algorithms, methods, and techniques for detecting uavs and uas using audio, radiofrequency, and video applications," *TecnoLógicas*, vol. 23, no. 48, pp. 269–285, May 2020.

[22] V. Semkin, J. Haarla, T. Pairon, C. Slezak, S. Rangan, V. Viikari, and C. Oestges, "Analyzing radar cross section signatures of diverse drone models at mmwave frequencies," *IEEE Access*, vol. 8, pp. 48 958–48 969, Mar. 2020.

[23] I. Roldan, C. R. Del-Blanco, Álvaro Duque De Quevedo, F. I. Urzaiz, J. G. Menoyo, A. A. López, D. Berjón, F. Jaureguizar, and N. García, "Dopplernet: A convolutional neural network for recognising targets in real scenarios using a persistent range-doppler radar," *IET Radar, Sonar and Navigation*, vol. 14, no. 4, pp. 593–600, Apr. 2020.

[24] A. Karlsson, M. Jansson, and M. Hämäläinen, "Model-aided drone classification using convolutional neural networks," in *2022 IEEE Radar Conference (RadarConf22)*, New York City, NY, USA, 2022, pp. 1–6.

[25] H. C. Kumawat, M. Chakraborty, A. A. B. Raj, and S. V. Dhavale, "Diat-μsat: Small aerial targets' micro-doppler signatures and their classification using cnn," *IEEE Geoscience and Remote Sensing Letters*, vol. 19, pp. 1–5, Aug. 2021.

[26] H. C. Kumawat, M. Chakraborty, and A. A. B. Raj, "Diat-radsatnet-a novel lightweight dcnn architecture for micro-doppler-based small unmanned aerial vehicle (suav) targets' detection and classification," *IEEE Transactions on Instrumentation and Measurement*, vol. 71, pp. 1–11, Jul. 2022.

[27] K. B. Kang, J. H. Choi, B. L. Cho, J. S. Lee, and K. T. Kim, "Analysis of micro-doppler signatures of small uavs based on doppler spectrum," *IEEE Trans. Aerosp. Electron. Syst.*, vol. 57, no. 5, pp. 3252–3267, Oct. 2021.

[28] H. Sun, B. S. Oh, X. Guo, and Z. Lin, "Improving the doppler resolution of ground-based surveillance radar for drone detection," *IEEE Trans. Aerosp. Electron. Syst.*, vol. 55, no. 6, pp. 3667–3673, Dec. 2019.

[29] B. S. Oh and Z. Lin, "Extraction of global and local micro-doppler signature features from fmcw radar returns for uav detection," *IEEE Trans. Aerosp. Electron. Syst.*, vol. 57, no. 2, pp. 1351–1360, Apr. 2021.

[30] C. Su, C. Zou, L. Jiao, and Q. Zhang, "A mimo radar signal processing algorithm for identifying chipless rfid tags," *Sensors*, vol. 21, no. 24, p. 8314, Dec. 2021.

[31] X.-R. Li, Z. Zhang, W.-X. Mao, X.-M. Wang, and J. Lu, "A derivation of colocated mimo radar equation," in *2011 International Conference on Computational Problem-Solving (ICCP)*, Chengdu, China, 2011, pp. 674–677.

[32] E. Fishler, A. Haimovich, R. Blum, R. Cimini, D. Chizhik, and R. Valenzuela, "Performance of mimo radar systems: advantages of angular diversity," in *Conference Record of the Thirty-Eighth Asilomar Conference on Signals, Systems and Computers, 2004.*, vol. 1, Pacific Grove, CA, USA, 2004, pp. 305–309.

[33] M. T. Frankford, K. B. Stewart, N. Majurec, and J. T. Johnson, "Numerical and experimental studies of target detection with mimo radar," *IEEE Trans. Aerosp. Electron. Syst.*, vol. 50, no. 2, pp. 1569–1577, Apr. 2014.

[34] P. Wellig, P. Speirs, C. Schuepbach, R. Oechslin, M. Renker, U. Boeniger, and H. Pratisto, "Radar systems and challenges for c-uav," in *2018 19th International Radar Symposium (IRS)*, Bonn, Germany, 2018, pp. 1–8.

[35] O. Biallawons, J. Klare, and L. Fuhrmann, "Improved uav detection with the mimo radar mira-cle ka using range-velocity processing and tdma correction algorithms," in *2018 19th International Radar Symposium (IRS)*, Bonn, Germany, 2018, pp. 1–10.

[36] A. Cidronali, M. Passafiume, P. Colantonio, G. Collodi, C. Florian, G. Leuzzi, M. Pirola, C. Ramella, A. Santarelli, and P. Traverso, "System level analysis of millimetre-wave gan-based mimo radar for detection of micro unmanned aerial vehicles," in *2019 PhotonIcs & Electromagnetics Research Symposium - Spring (PIERS-Spring)*, Rome, Italy, 2019, pp. 438–450.

[37] T. Al-Nuaim, M. Alam, and A. Aldowesh, "Low-cost implementation of a multiple-input multiple-output radar prototype for drone detection," in *2019 International Symposium ELMAR*, Zadar, Croatia, 2019, pp. 183–186.

[38] F. Yang, F. Xu, F. Fioranelli, J. L. Kernec, S. Chang, and T. Long, "Practical investigation of a mimo radar system capabilities for small drones detection," *IET Radar, Sonar & Navigation*, vol. 15, no. 7, pp. 760–774, Jul. 2021.

[39] B. Li, S. Wang, J. Zhang, X. Cao, and C. Zhao, "Ultra-fast accurate aoa estimation via automotive massive-mimo radar," *IEEE Trans. Veh. Technol.*, vol. 71, no. 2, pp. 1172–1186, Feb. 2022.

[40] T. Ghoshal and K. V. S. Hari, "Object classification using micro-doppler signature and clutter suppression in mimo radar," in *2022 IEEE International Conference on Electronics, Computing and Communication Technologies (CONECCT)*, Bangalore, India, 2022, pp. 1–5.

[41] X. Fang, J. Zhu, D. Huang, Z. Zhang, and G. Xiao, "E2dtf: An end-to-end detection and tracking framework for multiple micro-uavs with fmcw-mimo radar," *IEEE Trans. Microw. Theory Techn.*, vol. 61, pp. 1–16, Mar. 2023.

[42] H. Abedi, S. Luo, V. Mazumdar, M. M. Riad, and G. Shaker, "Ai-powered in-vehicle passenger monitoring using low-cost mm-wave radar," *IEEE Access*, vol. 10, pp. 18 998–19 012, Dec. 2022.

[43] H. Abedi, J. Boger, P. P. Morita, A. Wong, and G. Shaker, "Hallway gait monitoring using novel radar signal processing and unsupervised learning," *IEEE Sensors J.*, vol. 22, no. 15, pp. 15 133–15 145, Aug. 2022.

[44] H. Abedi, A. Ansariyan, P. P. Morita, A. Wong, J. Boger, and G. Shaker, "Ai-powered non-contact in-home gait monitoring and activity recognition system based on mm-wave fmcw radar and cloud computing," *IEEE Internet Things J.*, vol. 10, no. 11, pp. 9465–9481, Jan. 2023.

[45] H. Abedi, M. Ma, J. He, J. Yu, A. Ansariyan, and G. Shaker, "Deep learning-based in-cabin monitoring and vehicle safety system using a 4d imaging radar sensor," *IEEE Sensors J.*, vol. 23, no. 11, pp. 11 296–11 307, Jun. 2023.

[46] W. Gruener, J. Toernig, and P. Fielding, "Active-electronically-scanned-array based radar system features," in *Radar 97 (Conf. Publ. No. 449)*, Edinburgh, UK, 1997, pp. 339–343.

[47] H. Hommel and H. Feldle, "Current status of airborne active phased array (aesa) radar systems and future trends," in *First European Radar Conference, 2004. EURAD.*, Amsterdam, Netherlands, 2004, pp. 121–124.

[48] R. G. Lorenz and S. P. Boyd, "Robust minimum variance beamforming," *IEEE Trans. Signal Process.*, vol. 53, no. 5, pp. 1684–1696, May 2005.

[49] A. D. de Quevedo, F. I. Urzaiz, J. G. Menoyo, and A. A. Lopez, "Drone detection with x-band ubiquitous radar," in *2018 19th International Radar Symposium (IRS)*, Bonn, Germany, 2018, pp. 1–10.

[50] F. I. Urzaiz, A. D. de Quevedo, A. M. Ayuso, A. G. Machado, J. G. Menoyo, and A. A. Lopez, "Design, implementation and first experimental results of an x-band ubiquitous radar system," in *2018 IEEE Radar Conference (RadarConf18)*, Oklahoma City, OK, USA, 2018, pp. 1150–1155.

[51] R. Takahashi, T. Inaba, T. Takahashi, and H. Tasaki, "Digital monopulse beamforming for achieving the crlb for angle accuracy," *IEEE Trans. Aerosp. Electron. Syst.*, vol. 54, no. 1, pp. 315–323, Sep. 2018.

[52] A. D. de Quevedo, F. I. Urzaiz, J. G. Menoyo, and A. A. Lopez, "Drone detection and radar-cross-section measurements by rad-dar," *IET Radar, Sonar & Navigation*, vol. 13, no. 9, pp. 1437–1447, Aug. 2019.

[53] K. Z. Rajab, B. Wu, P. Alizadeh, and A. Alomainy, "Multi-target tracking and activity classification with millimeter-wave radar," *Applied Physics Letters*, vol. 119, no. 3, p. 34101, Jul. 2021.

[54] F. Ibanez Urzaiz, J. Gismero-Menoyo, A. Asensio-Lopez, and A. D. de Quevedo, "Digital beamforming on receive array calibration: Application to a persistent x-band surface surveillance radar," *IEEE Sensors J.*, vol. 21, no. 5, pp. 6752–6760, Nov. 2021.

[55] H. Haifawi, F. Fioranelli, A. Yarovoy, and R. van der Meer, "Drone detection & classification with surveillance 'radar on-the-move' and yolo," in *2023 IEEE Radar Conference (RadarConf23)*, San Antonio, TX, USA, 2023, pp. 1–6.

[56] Skolnik and M. Ivan, *Radar Handbook*. New York: McGraw Hill Book Co., 1970.

[57] ——, *Introduction to Radar Systems*. New York: McGraw-Hill Education, 1980.

[58] X. Guo, C. S. Ng, E. de Jong, and A. B. Smits, "Micro-doppler based mini-uav detection with low-cost distributed radar in dense urban environment," in *2019 16th European Radar Conference (EuRAD)*, Paris, France, 2019, pp. 189–192.

[59] S. Yoon, S. Kim, J. Jung, S. Cha, Y. Baek, B. Koo, I. Choi, and S. Park, "Efficient protocol to use fmcw radar and cnn to distinguish micro-doppler signatures of multiple drones and birds," *IEEE Access*, vol. 10, pp. 26 033–26 044, Mar. 2022.

[60] B. Tsang, R. Narayanan, R. B. B. Tsang, R. M. Narayanan, R. Bharadwaj, and B. T. Tsang, "Experimental analysis of micro-doppler characteristics of drones and birds for classification purposes," *Radar Sensor Technology XXVI*, vol. 12108, pp. 198–210, May 2022.

[61] R. I. A. Harmanny, J. J. M. de Wit, and G. P. Cabic, "Radar micro-doppler feature extraction using the spectrogram and the cepstrogram," in *2014 11th European Radar Conference*, Rome, Italy, 2014, pp. 165–168.

[62] T. Hong, C. Fang, H. Hao, and W. Sun, "Identification technology of uav based on micro-doppler effect," in *2021 International Wireless Communications and Mobile Computing (IWCMC)*, Harbin City, China, 2021, pp. 308–311.

[63] S. Rahman and D. Robertson, "Time-frequency analysis of millimeter-wave radar micro-doppler data from small uavs," in *2017 Sensor Signal Processing for Defence Conference (SSPD)*. London, UK: Institute of Electrical and Electronics Engineers Inc., Dec. 2017, pp. 1–5.

[64] S. Rahman and D. A. Robertson, "Radar micro-doppler signatures of drones and birds at k-band and w-band," *Scientific Reports*, vol. 8, no. 1, p. 17396, Nov. 2018.

[65] B. S. Oh, X. Guo, F. Wan, K. A. Toh, and Z. Lin, "Micro-doppler mini-uav classification using empirical-mode decomposition features," *IEEE Geoscience and Remote Sensing Letters*, vol. 15, no. 2, pp. 227–231, Feb. 2018.

[66] B. S. Oh, X. Guo, and Z. Lin, "A uav classification system based on fmcw radar micro-doppler signature analysis," *Expert Systems with Applications*, vol. 132, pp. 239–255, Oct. 2019.

[67] Y. Zhao and Y. Su, "The extraction of micro-doppler signal with emd algorithm for radar-based small uavs' detection," *IEEE Transactions on Instrumentation and Measurement*, vol. 69, no. 3, pp. 929–940, Mar. 2020.

[68] X. Ma, B.-S. Oh, L. Sun, K.-A. Toh, and Z. Lin, "Emd-based entropy features for micro-doppler mini-uav classification," in *2018 24th International Conference on Pattern Recognition (ICPR)*, Beijing, China, 2018, pp. 1295–1300.

[69] M. Ritchie, F. Fioranelli, H. Griffiths, and B. Torvik, "Micro-drone rcs analysis," in *2015 IEEE Radar Conference*. Johannesburg, South Africa: Institute of Electrical and Electronics Engineers Inc., Oct. 2015, pp. 452–456.

[70] M. Ezuma, C. K. Anjinappa, M. Funderburk, and I. Guvenc, "Radar cross section based statistical recognition of uavs at microwave frequencies," *IEEE Trans. Aerosp. Electron. Syst.*, vol. 58, no. 1, pp. 27–46, Feb. 2022.

[71] R. Fu, M. A. Al-Absi, K. H. Kim, Y. S. Lee, A. A. Al-Absi, and H. J. Lee, "Deep learning-based drone classification using radar cross section signatures at mmwave frequencies," *IEEE Access*, vol. 9, pp. 161 431–161 444, Sep. 2021.

[72] M. Passafiume, N. Rojhani, G. Collodi, and A. Cidronali, "Modeling small uav micro-doppler signature using millimeter-wave fmcw radar," *Electronics*, vol. 10, no. 6, pp. 1–16, Mar. 2021.

[73] J. Ren and X. Jiang, "Regularized 2-d complex-log spectral analysis and subspace reliability analysis of micro-doppler signature for uav detection," *Pattern Recognition*, vol. 69, pp. 225–237, Apr. 2017.

[74] P. Molchanov, K. Egiazarian, J. Astola, R. I. A. Harmanny, and J. J. M. de Wit, "Classification of small uavs and birds by micro-doppler signatures," in *2013 European Radar Conference*, Nuremberg, Germany, 2013, pp. 172–175.

[75] M. Ritchie, F. Fioranelli, H. Borrion, and H. Griffiths, "Multistatic micro-doppler radar feature extraction for classification of unloaded/loaded micro-drones," *IET Radar, Sonar and Navigation*, vol. 11, no. 1, pp. 116–124, Jan. 2017.

[76] J. S. Patel, C. Al-Ameri, F. Fioranelli, and D. Anderson, "Multi-time frequency analysis and classification of a micro-drone carrying payloads using multistatic radar," *The Journal of Engineering*, vol. 2019, no. 20, pp. 7047–7051, Oct. 2019.

[77] F. Hoffmann, M. Ritchie, F. Fioranelli, A. Charlish, and H. Griffiths, "Micro-doppler based detection and tracking of uavs with multistatic radar," in *2016 IEEE Radar Conference (RadarConf)*, Philadelphia, PA, USA, 2016, pp. 1–6.

[78] R. Palamà, F. Fioranelli, M. Ritchie, M. Inggs, S. Lewis, and H. Griffiths, "Measurements and discrimination of drones and birds with a multi-frequency multistatic radar system," *IET Radar, Sonar & Navigation*, vol. 15, no. 8, pp. 841–852, Aug. 2021.

[79] H. Dale, C. Baker, M. Antoniou, M. Jahangir, G. Atkinson, and S. Harman, "Snr-dependent drone classification using convolutional neural networks," *IET Radar, Sonar and Navigation*, vol. 16, no. 1, pp. 22–33, Jan. 2022.

[80] H. Dale, M. Jahangir, C. J. Baker, M. Antoniou, S. Harman, and B. I. Ahmad, "Convolutional neural networks for robust classification of drones," in *2022 IEEE Radar Conference (RadarConf22)*, New York City, NY, USA, 2022, pp. 1–6.

[81] D. H. Shin, D. H. Jung, D. C. Kim, J. W. Ham, and S. O. Park, "A distributed fmcw radar system based on fiber-optic links for small drone detection," *IEEE Transactions on Instrumentation and Measurement*, vol. 66, no. 2, pp. 340–347, Feb. 2017.

[82] M. Ezuma, O. Ozdemir, C. K. Anjinappa, W. A. Gulzar, and I. Guvenc, "Micro-uav detection with a low-grazing angle millimeter wave radar," in *2019 IEEE Radio and Wireless Symposium (RWS)*, Orlando, FL, USA, 2019, pp. 1–4.

[83] J. A. Paredes, F. J. Álvarez, M. Hansard, and K. Z. Rajab, "A gaussian process model for uav localization using millimetre wave radar," *Expert Systems with Applications*, vol. 185, p. 115563, Jul. 2021.

[84] J. Bernard-Cooper, S. Rahman, D. Robertson, and D. A. Robertson, "Multiple drone type classification using machine learning techniques based on fmcw radar micro-doppler data," *Radar Sensor Technology XXVI*, vol. 12108, pp. 99–112, May 2022.

[85] E. Hunter, D. Raval, B. Balaji, A. D. E. Hunter, A. Damini, and P. Carniglia, "Convolutional neural networks and wavelets for drone classification," *https://doi.org/10.1117/12.2618832*, vol. 12108, pp. 211–223, May 2022.

[86] T. Dai, S. Xu, B. Tian, J. Hu, Y. Zhang, and Z. Chen, "Extraction of micro-doppler feature using lmd algorithm combined supplement feature for uavs and birds classification," *Remote Sensing*, vol. 14, no. 9, p. 2196, May 2022.

[87] S. Björklund, "Target detection and classification of small drones by boosting on radar micro-doppler," in *2018 15th European Radar Conference (EuRAD)*, Madrid, Spain, 2018, pp. 182–185.

[88] Y. Wang, C. Zhao, and G. Luo, "A lightweight uav recognition algorithm based on micro-doppler features," in *2021 IEEE/CIC International Conference on Communications in China (ICCC)*, Xiamen, China, 2021, pp. 6–10.

[89] G. Ji, C. Song, and H. Huo, "Detection and identification of low-slow-small rotor unmanned aerial vehicle using micro-doppler information," *IEEE Access*, vol. 9, pp. 99 995–100 008, Jul. 2021.

[90] V. V. Reddy and S. Peter, "Uav micro-doppler signature analysis using fmcw radar," in *2021 IEEE Radar Conference (RadarConf21)*, Atlanta, GA, USA, 2021, pp. 1–6.

[91] A. Huang, P. Sévigny, B. Balaji, and S. Rajan, "Radar micro-doppler-based rotary drone detection using parametric spectral estimation methods," in *2020 IEEE SENSORS*, Rotterdam, Netherlands, 2020, pp. 1–4.

[92] X. Chen, H. Zhang, J. Song, J. Guan, J. Li, and Z. He, "Micro-motion classification of flying bird and rotor drones via data augmentation and modified multi-scale cnn," *Remote Sensing*, vol. 14, no. 5, p. 1107, Feb. 2022.

[93] D. Raval, E. Hunter, S. Hudson, A. Damini, and B. Balaji, "Convolutional neural networks for classification of drones using radars," *Drones*, vol. 5, no. 4, p. 149, Dec. 2021.

[94] W. S. Chen, J. Liu, and J. Li, "Classification of uav and bird target in low-altitude airspace with surveillance radar data," *The Aeronautical Journal*, vol. 123, no. 1260, pp. 191–211, Feb. 2019.

[95] N. Rojhani, M. Passafiume, M. Sadeghibakhi, G. Collodi, and A. Cidronali, "Model-based data augmentation applied to deep learning networks for classification of micro-doppler signatures using fmcw radar," *IEEE Trans. Microw. Theory Techn.*, vol. 71, no. 5, pp. 2222–2236, May 2022.

[96] C. J. Li and H. Ling, "An investigation on the radar signatures of small consumer drones," *IEEE Antennas and Wireless Propagation Letters*, vol. 16, pp. 649–652, Jul. 2017.

[97] P. Zhang, L. Yang, G. Chen, and G. Li, "Classification of drones based on micro-doppler signatures with dual-band radar sensors," in *2017 Progress in Electromagnetics Research Symposium - Fall (PIERS - FALL)*. Singapore: Electromagnetics Academy, Nov. 2017, pp. 638–643.

[98] P. Zhang, G. Li, C. Huo, and H. Yin, "Exploitation of multipath micro-doppler signatures for drone classification," *IET Radar, Sonar & Navigation*, vol. 14, no. 4, pp. 586–592, Apr. 2020.

[99] W. Zhang, G. Li, and C. Baker, "Radar recognition of multiple micro-drones based on their micro-doppler signatures via dictionary learning," *IET Radar, Sonar & Navigation*, vol. 14, no. 9, pp. 1310–1318, Sep. 2020.

[100] P. K. Rai, H. Idsoe, R. R. Yakkati, A. Kumar, M. Z. A. Khan, P. K. Yalavarthy, and L. R. Cenkeramaddi, "Localization and activity classification of unmanned aerial vehicle using mmwave fmcw radars," *IEEE Sensors J.*, vol. 21, no. 14, pp. 16 043–16 053, Jul. 2021.

[101] B. K. Kim, H. S. Kang, and S. O. Park, "Drone classification using convolutional neural networks with merged doppler images," *IEEE Geoscience and Remote Sensing Letters*, vol. 14, no. 1, pp. 38–42, Jan. 2017.

[102] M. Caris, W. Johannes, S. Sieger, V. Port, and S. Stanko, "Detection of small uas with w-band radar," in *2017 18th International Radar Symposium (IRS)*, Prague, Czech Republic, 2017, pp. 1–6.

[103] G. J. Mendis, T. Randeny, J. Wei, and A. Madanayake, "Deep learning based doppler radar for micro uas detection and classification," in *MILCOM 2016 - 2016 IEEE Military Communications Conference*. Baltimore, MD, USA: Institute of Electrical and Electronics Engineers Inc., Dec. 2016, pp. 924–929.

[104] J. Park, S. Park, D. H. Kim, and S. O. Park, "Leakage mitigation in heterodyne fmcw radar for small drone detection with stationary point concentration technique," *IEEE Trans. Microw. Theory Techn.*, vol. 67, no. 3, pp. 1221–1232, Mar. 2019.

[105] J. Park, D. H. Jung, K. B. Bae, and S. O. Park, "Range-doppler map improvement in fmcw radar for small moving drone detection using the stationary point concentration technique," *IEEE Trans. Microw. Theory Techn.*, vol. 68, no. 5, pp. 1858–1871, May 2020.

[106] J. Park, J. S. Park, K. B. Bae, and S. O. Park, "Advanced stationary point concentration technique for leakage mitigation and small drone detection with fmcw radar," *IEEE Trans. Microw. Theory Techn.*, vol. 69, no. 3, pp. 1791–1804, Mar. 2021.

[107] C. Bennett, M. Jahangir, F. Fioranelli, B. I. Ahmad, and J. L. Kernec, "Use of symmetrical peak extraction in drone micro-doppler classification for staring radar," in *2020 IEEE Radar Conference (RadarConf20)*. Florence, Italy: Institute of Electrical and Electronics Engineers Inc., Sep. 2020.

[108] M. Moore, D. Robertson, S. Rahman, D. A. Robertson, and G. Doppler, "94 ghz doppler radar for experimental validation of small uav micro-doppler," *Radar Sensor Technology XXVI*, vol. 12108, pp. 281–291, May 2022.

[109] M. Moore, D. A. Robertson, and S. Rahman, "Simulating uav micro-doppler using dynamic point clouds," in *2022 IEEE Radar Conference (RadarConf22)*, New York City, NY, USA, 2022, pp. 1–6.

[110] D. White, M. Jahangir, M. Antoniou, C. Baker, J. Thiyagalingam, S. Harman, and C. Bennett, "Multi-rotor drone micro-doppler simulation incorporating genuine motor speeds and validation with l-band staring radar," in *2022 IEEE Radar Conference (RadarConf22)*, New York City, NY, USA, 2022, pp. 1–6.

[111] A. Hanif, M. Muaz, A. Hasan, and M. Adeel, "Micro-doppler based target recognition with radars: A review," *IEEE Sensors J.*, vol. 22, no. 4, pp. 2948–2961, Feb. 2022.

[112] X. Wang, P. Wang, X. Cao, and V. C. Chen, "Interferometric angular velocity measurement of rotating blades: Theoretical analysis, modeling and simulation study," *IET Radar, Sonar and Navigation*, vol. 13, no. 3, pp. 438–444, Mar. 2019.

[113] P. Speirs, A. Murk, M. Renker, P. Wellig, and U. Aulenbacher, "High-detail simulations of consumer-grade uav rcs signatures, and comparisons against measurements," in *STO-MP-MSG-SET-183*, Virtual Mode via WebEX, Apr. 2021, pp. 1–26.

[114] A. Schroder, M. Renker, U. Aulenbacher, A. Murk, U. Boniger, R. Oechslin, and P. Wellig, "Numerical and experimental radar cross section analysis of the quadrocopter dji phantom 2," in *2015 IEEE Radar Conference*, Johannesburg, South Africa, 2015, pp. 463–468.

[115] L. Lehmann and J. Dall, "Simulation-based approach to classification of airborne drones," in *2020 IEEE Radar Conference (RadarConf20)*, Florence, Italy, 2020, pp. 1–6.

[116] "Ansys inc." 2022. [Online]. Available: https://www.ansys.com/products/electronics/ansys-hfss

[117] "Phantom 4 pro v2.0 - dji," 2023. [Online]. Available: https://www.dji.com/ca/phantom-4-pro-v2

[118] P. Sedivy and O. Nemec, "Drone rcs statistical behaviour," in *Proceedings of the MSG-SET-183 Specialists' Meeting on "Drone Detectability: Modelling the Relevant Signature", North Atlantic Treaty Organization (NATO)*, Held Virtually (via WebEx), 2021, pp. 4–1.

[119] E. F. Knott, J. F. Schaeffer, and M. T. Tulley, *Radar Cross Section*. Raleigh, NC: SciTech Publishing, Inc., 2004.

[120] "Albatross uav : Long range drone," 2022. [Online]. Available: https://www.appliedaeronautics.com/albatross-uav/

[121] "Fixed-wing drone, commercial long range uav, applied aeronautics," 2022. [Online]. Available: https://www.unmannedsystemstechnology.com/company/applied-aeronautics/

[122] "Unmanned helicopter, small rotary, tactical uav, isr drones, ruav," 2022. [Online]. Available: https://www.unmannedsystemstechnology.com/company/steadicopter/

[123] "Dji fpv - specs - dji," 2022. [Online]. Available: https://www.dji.com/ca/dji-fpv/specs

[124] J. Torres-Sánchez, F. L. Pez-Granados, D. Castro, and A. I. P. A-Barragán, "Configuration and specifications of an unmanned aerial vehicle (uav) for early site specific weed management," *PLoS ONE*, vol. 8, no. 3, p. 58210, Mar. 2013.

[125] "Microdrones md4-1000 full specifications & reviews," 2022. [Online]. Available: https://productz.com/en/microdrones-md4-1000/p/y5RW

[126] "Phantom 3 standard - dji," 2023. [Online]. Available: https://www.dji.com/ca/phantom-3-standard

[127] "Dji s900 hex-rotor drone — 3d cad model library — grabcad," 2023. [Online]. Available: https://grabcad.com/library/dji-s900-hex-rotor-drone-1

[128] P. Lang, X. Fu, M. Martorella, J. Dong, R. Qin, X. Meng, and M. Xie, "A comprehensive survey of machine learning applied to radar signal processing," *arxiv*, Sep. 2020.

[129] "Keras," 2022. [Online]. Available: https://keras.io/

[130] D. P. Kingma and J. Ba, "Adam: A method for stochastic optimization," *arxiv*, Dec. 2014.

[131] C. W. Hsu and C. J. Lin, "A comparison of methods for multiclass support vector machines," *IEEE Transactions on Neural Networks*, vol. 13, no. 2, pp. 415–425, Mar. 2002.

[132] "Dji phantom 3 - 3d cad model collection — grabcad community library," 2022. [Online]. Available: https://grabcad.com/library?page=1&time=alltime&sort=recent&query=dji%20phantom%203

[133] "Simplified straw rocket — 3d cad model library — grabcad," 2023. [Online]. Available: https://grabcad.com/library/simplified-straw-rocket-1

[134] "Dynamite — 3d cad model library — grabcad," 2023. [Online]. Available: https://grabcad.com/library/dynamite

[135] X. peng Zhu, Q. Zhang, and H. wei Li, "Isar imaging analysis of bistatic fmcw radar," in *Proceedings of the 9th International Symposium on Antennas, Propagation and EM Theory*, Guangzhou, China, 2010, pp. 540–543.

[136] F. Turin, D. Pastina, P. Lombardo, and L. Corucci, "Isar imaging of ground targets with an x-band fmcw radar system for airport surveillance," in *2014 15th International Radar Symposium (IRS)*, Gdansk, Poland, 2014, pp. 1–5.

[137] Z. Peng, J.-M. Muñoz-Ferreras, R. Gómez-García, and C. Li, "Fmcw radar fall detection based on isar processing utilizing the properties of rcs, range, and doppler," in *2016 IEEE MTT-S International Microwave Symposium (IMS)*, San Francisco, CA, USA, 2016, pp. 1–3.

[138] Z. Peng, J. M. Munoz-Ferreras, Y. Tang, C. Liu, R. Gomez-Garcia, L. Ran, and C. Li, "A portable fmcw interferometry radar with programmable low-if architecture for localization, isar imaging, and vital sign tracking," *IEEE Trans. Microw. Theory Techn.*, vol. 65, no. 4, pp. 1334–1344, Apr. 2017.

[139] S. Latthe, S. Mohite, L. Tagde, P. Chilveri, N. Akhter, and A. A. B. Raj, "A review on isar imaging techniques for low rcs targets," *International Journal of Engineering Research and Reviews*, vol. 10, no. 4, pp. 15–27, Dec. 2022.

[140] A. J. Smola and B. Schölkopf, "A tutorial on support vector regression," *Statistics and Computing*, vol. 14, no. 3, pp. 199–222, Aug. 2004.

[141] J. Park, J.-S. Park, and S.-O. Park, "Small drone classification with light cnn and new micro-doppler signature extraction method based on a-spc technique," *Arxiv*, Sep. 2020.

[142] S. K. Kim and D. M. Tilbury, "Mathematical modeling and experimental identification of an unmanned helicopter robot with flybar dynamics," *Journal of Robotic Systems*, vol. 21, no. 3, pp. 95–116, Mar. 2004.

[143] E. Bekir, *Introduction to modern navigation systems.* Singapore: World scientific, 2007.

[144] K. Singh, "Modelling and controls of a hexacopter," Master's thesis, Texas A&M University-Kingsville, 2018.

[145] K. Simonyan and A. Zisserman, "Very deep convolutional networks for large-scale image recognition," in *3rd International Conference on Learning Representations, ICLR 2015, Computational and Biological Learning Society.* San Diego, CA, USA: International Conference on Learning Representations, ICLR, Sep. 2014, pp. 1–14.

[146] "Imaging radar using cascaded mmwave sensor," 2023. [Online]. Available: https://www.ti.com/lit/ug/tiduen5a/tiduen5a.pdf

[147] J. Xu, "An extended one-versus-rest support vector machine for multi-label classification," *Neurocomputing*, vol. 74, no. 17, pp. 3114–3124, Oct. 2011.

[148] "76–81 ghz band radar service radiated power limits," 2023. [Online]. Available: https://www.ecfr.gov/current/title-47/chapter-I/subchapter-D/part-95/subpart-M/subject-group-ECFR938fd48a3f538f7/section-95.3367

[149] "Ti mmwave radar device regulatory compliance guide," 2023. [Online]. Available: https://www.ti.com/lit/an/spracp3c/spracp3c.pdf?ts=1696969321933&ref_url=https%253A%252F%252Fwww.google.com%252F

[150] "Awr1443boost ti user guide," 2023. [Online]. Available: https://www.ti.com/lit/ug/swru507c/swru507c.pdf?ts=1696938219393

[151] W.-Y. Loh, "Classification and regression trees," *Wiley interdisciplinary reviews: data mining and knowledge discovery*, vol. 1, no. 1, pp. 14–23, Jan. 2011.

[152] T. Duan, A. Anand, D. Y. Ding, K. K. Thai, S. Basu, A. Ng, and A. Schuler, "NGBoost: Natural gradient boosting for probabilistic prediction," in *Proceedings of the 37th International Conference on Machine Learning*, vol. 119. Vienna, Austria: PMLR, Jul. 2020, pp. 2690–2700.